ORIGINAL ARTICLE

A diachronous record of metamorphism in metapelites of the Western Gneiss Region, Norway

Samantha March[1] | **Martin Hand[1]** | **Renée Tamblyn[1,2]** | **Bruna B. Carvalho[3]** | **Chris Clark[4]**

[1]Department of Earth Sciences, University of Adelaide, Adelaide, South Australia, Australia

[2]The Institute for Geology, Bern University, Bern, Switzerland

[3]Dipartimento di Geoscienze, Università degli Studi di Padova, Padua, Italy

[4]School of Earth and Planetary Sciences, Curtin University, Perth, Western Australia, Australia

Correspondence
Samantha March, Department of Earth Sciences, University of Adelaide, Adelaide, South Australia, Australia.
Email: samantha.march@adelaide.edu.au

Handling Editor: Prof. Richard White

Abstract

In this study, data from garnet-kyanite metapelites in ultrahigh-pressure (UHP) domains of the Western Gneiss Region (WGR), Norway, are presented. U–Pb geochronology and trace element compositions in zircon, monazite, apatite, rutile and garnet were acquired, and pressure–temperature (P–T) conditions were calculated using mineral equilibria forward modelling and Zr-in-rutile thermometry. Garnet-kyanite gneiss from Ulsteinvik record a prograde evolution passing through ∼690–710°C and ∼9–11 kbar. Zircon and rutile age and thermometry data indicate these prograde conditions significantly predate Silurian UHP subduction in the WGR and are interpreted to record early Caledonian subduction of continental-derived allochthons. Minimum peak conditions in the Ulsteinvik metapelite occur at ∼28 kbar, constrained by an inferred garnet+kyanite+omphacite+muscovite+rutile+coesite+H_2O assemblage. The retrograde evolution passed through ∼740°C and ∼7 kbar, first recorded by the destruction of omphacite and followed by the partial replacement of kyanite and garnet by cordierite and spinel. Garnet-kyanite metapelite from the diamond-bearing Fjørtoft outcrop documents a polymetamorphic history, with garnet forming during the late Mesoproterozoic and limited preservation of high-pressure Caledonian assemblages. Similar to the Ulsteinvik metapelite, zircon and rutile age data from the Fjørtoft metapelite also record pre-Scandian Caledonian ages. Two potential tectonic scenarios are possible: (1) The samples were exhumed at different times during pre-Scandian subduction of the Blåhø nappe, or (2) the samples do not share a history in the same nappe complex, instead the Ulsteinvik metapelite is a constituent of the Seve-Blåhø Nappe, whilst the Fjørtoft metapelite shares its history within a separate nappe complex.

KEYWORDS
metapelite, P–T pseudosection, subduction, U–Pb geochronology, Western Gneiss Region

1 | INTRODUCTION

Continental collision is one of the most dramatic and visible manifestations of plate tectonics, playing a fundamental role in the evolution of the continents (e.g. Batt & Braun, 1999; Butler et al., 2012; Nance & Murphy, 2013). Since the discoveries of diagnostic ultrahigh-pressure (UHP) minerals such as diamond in the Kokchetav Massif, Kazakhstan (Sobolev & Shatsky, 1990), and coesite in the Alps and Scandinavian Caledonides (Chopin., 1984; Smith, 1984), it has been widely recognized that continental lithosphere may experience deep subduction and be subject to UHP conditions (>28 kbar) during collision. The buoyancy of continental crust relative to oceanic crust means subducted continental UHP terranes are more likely to be exhumed than subducted oceanic slabs (e.g. Ernst et al., 1997; Hacker et al., 2011; Sizova et al., 2019), thereby providing valuable insight into UHP geodynamic processes.

The Western Gneiss Region (WGR), in western Norway, is one of the best-preserved examples of continental subduction known. The WGR experienced the burial of continental lithosphere to mantle depths in excess of 120 km. Subsequently, over 30,000 km^2 of this subducted continental lithosphere was exhumed and is now preserved in outcrops along the west coast of Norway (Figure 1; e.g. Hacker, 2007; Hacker et al., 2010; Walsh et al., 2013; Walsh & Hacker, 2004). Consequently, the WGR is among the largest, best-exposed, and most-

studied UHP terranes in the world (e.g. DesOrmeau et al., 2015; Kylander-Clark et al., 2007; Root et al., 2005; Terry et al., 2000a). It provides the unique opportunity to investigate the timescales of deep continental burial and exhumation, as well as the structural processes associated with UHP metamorphism (Butler et al., 2018; Cutts et al., 2019; Roberts, 2002).

The identification of coesite and coesite replacement textures, as well as microdiamond (Carswell et al., 2003; Cuthbert et al., 2000; Dobrzhinetskaya et al., 1995; Smith & Godard, 2013; Terry et al., 2000b; van Roermund et al., 2002; Vrijmoed et al., 2006, 2008; Wain, 1997; Walczak et al., 2019), has aided in defining three distinct UHP domains within the WGR: Nordøyane, Sørøyane, and Nordfjord (Figure 1). P–T conditions increase north-westwards within these domains (Cuthbert et al., 2000), suggesting past coherence of Nordøyane, Sørøyane and Nordfjord and their oblique subduction (Carswell et al., 2006; Carswell & Cuthbert, 2003; Cuthbert et al., 2000; Griffin & Brueckner, 1985; Hacker et al., 2010; E.J. Krogh, 1977). UHP domains are dominated by quartzofeldspathic gneiss with minor amounts of eclogite, quartzite, marble, calc-silicate, anorthosite, gabbro, peridotite, and metapelitic gneiss (Bryhni, 1966; Dransfield, 1994; Gjelsvik, 1951; Robinson, 1995).

Numerous studies with the broad aim of characterizing the timescales, P–T conditions, and processes associated with the deep subduction of continental lithosphere in the WGR have been undertaken. This research has primarily focused on the metamorphic
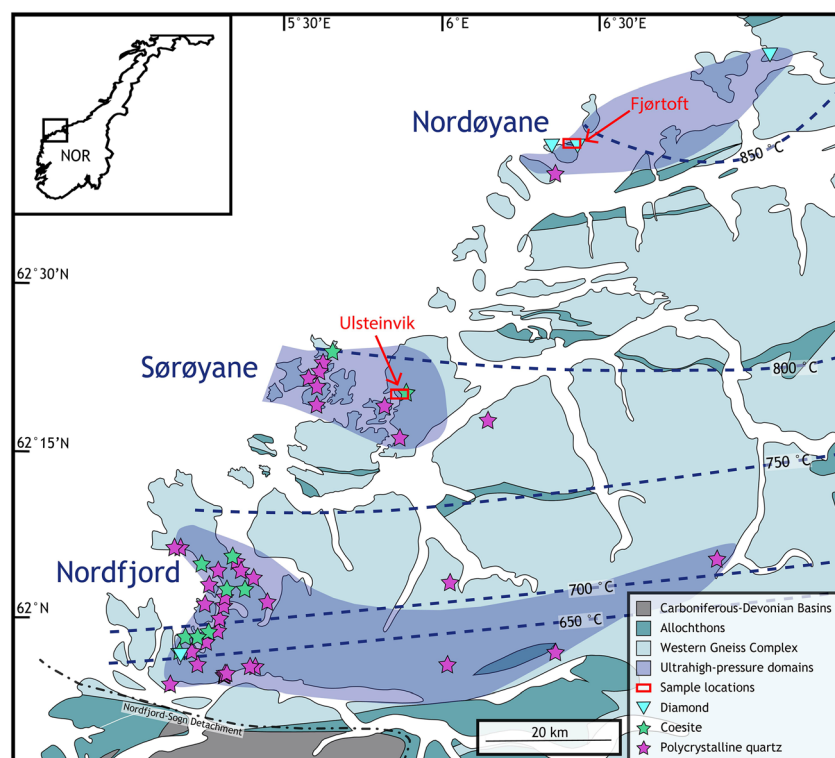

FIGURE 1 Geologic map of the Western Gneiss Region, Norway, highlighting UHP terranes (modified from Walsh et al., 2013) and sample locations. Coesite and polycrystalline quartz locations from Wain et al. (1997), Cuthbert et al. (2000), Carswell et al. (2003), Root et al. (2005), and Spengler et al. (2006), where polycrystalline quartz aggregates are interpreted to indicate the former presence of coesite. Diamond locations from Dobrzhinetskaya et al. (1995), van Roermund et al. (2002), Vrijmoed et al. (2008), and Smith and Godard (2013). Isotherms from Kylander-Clark et al. (2008) [Colour figure can be viewed at wileyonlinelibrary.com]

evolution of mafic eclogites and quartzofeldspathic rocks during the main Scandian phase of subduction (430–380 Ma; e.g. Beckman et al., 2014; Carswell et al., 2003; Corfu et al., 2013; Cuthbert et al., 2000; Griffin & Brueckner, 1985; Kylander-Clark et al., 2007; Peterman et al., 2009; T.E. Krogh et al., 2011;). Evidence of UHP conditions in these rocks has been supported by various forms of inverse thermobarometry as well as the identification of diagnostic UHP minerals (e.g. Carswell et al., 2006; Cuthbert et al., 2000; Engvik et al., 2007; Glodny et al., 2008; Peterman et al., 2009; Renedo et al., 2015; Terry et al., 2000a; Vrijmoed et al., 2006; Wain, 1997).

Significant work has also been focused on the volumetrically minor metapelites of the region (Cuthbert & van Roermund, 2011; Dobrzhinetskaya et al., 1995; Hacker et al., 2015; Holder et al., 2015; Terry et al., 2000b; Walczak et al., 2019). Metapelitic rocks typically contain higher concentrations of U and Th relative to mafic rocks and potentially offer a greater range of accessory minerals that can be used to constrain the ages of evolving mineral assemblages, making them a valuable tool in decoding the metamorphic history of the WGR. In the northern Caledonides, metapelites have been found to retain a more complete history of the evolution of the collision involving Baltica and its ultimate amalgamation with Laurentia, with the record of older c. 500–480 Ma and c. 460–445 Ma UHP metamorphic events that precede the main Scandian phase of subduction preserved within the Seve-Blåhø nappe in Fjørtoft (e.g. Barnes et al., 2019, 2021; Brueckner & van Roermund, 2004; Fassmer et al., 2017, 2021; Majka et al., 2014; Root & Corfu, 2012; Walczak et al., 2020). The record of multiple subduction events within the WGR was first used by Brueckner and van Roermund (2004) and Brueckner (2006) to propose a 'dunk tectonics' geodynamic model, in which continental crust is repeatedly, briefly immersed in the mantle during successive subduction/eduction events. These subduction events are tied to collision with continental fragments and arcs. Majka et al. (2014) suggested the orogen-scale Seve-Blåhø nappe may have comprised a microcontinent belonging to the outer Baltic margin that collided and subducted beneath a forearc block prior to the main Baltican phase of subduction. The later imbrication of nappes atop the main Baltican continent results in the modern manifestation of discrete, allochthonous terranes dispersed across the WGR that have been variably overprinted by the main Scandian subduction event.

In this study, a focused approach was used to investigate the tectonometamorphic history of two metapelitic samples. New P–T forward modelling coupled with U–Pb multi-mineral geochronology, petrochronology, and Zr-in-rutile thermometry is presented for metapelitic rocks in the WGR. Samples were collected from two localities (Figure 1): (a) a metapelitic outcrop in close proximity to the Hareidland eclogite in Ulsteinvik (Carswell et al., 2003; Mysen & Heier, 1972) and (b) a diamond-bearing outcrop on the island of Fjørtoft (Figure 1; Dobrzhinetskaya et al., 1995; van Roermund et al., 2002; Cuthbert & van Roermund, 2011).

2 | GEOLOGICAL BACKGROUND

2.1 | Overview of the Western Gneiss Region

The Western Gneiss Region is a parautochthonous polymetamorphic terrane, referred to as the Western Gneiss Complex (WGC), which is overlain by a series of oceanic and continental-derived allochthons. The WGC is dominated by granodioritic-tonalitic intrusive rocks that formed during the Gothian Orogeny, from c. 1700–1500 Ma (Åhäll & Connelly, 2008). The Mesoproterozoic Orogeny (c. 1100–900 Ma) imparted an amphibolite to granulite facies overprint and was accompanied by migmatization, plutonism, and mafic dyke emplacement (Brueckner, 1972; Corfu et al., 2013; Kylander-Clark et al., 2008; Tucker et al., 2004).

The Caledonian Orogeny spanned from c. 505 to 350 Ma, with early pre-Scandian (c. 505–430 Ma) deformation, metamorphism, and juxtaposition of continental and oceanic allochthons occurring as the Iapetus basin contracted towards closure (e.g. Brown & Johnson, 2018; Fassmer et al., 2017; Gilotti et al., 2004; Mcclelland et al., 2006). This caused multiple collision-subduction events to occur between outboard terranes (allochthonous microcontinents and island arcs) and Baltica's hyperextended margin, embodying the 'dunk tectonics' evolutionary model (Brueckner, 2006; Brueckner & van Roermund, 2004). One of these allochthonous terranes is the Blåhø nappe, which is the Norway correlative of the Seve Nappe Complex (Brueckner & van Roermund, 2004; Majka et al., 2014; Terry et al., 2000b; Walczak et al., 2019). The Seve Nappe Complex outcrops in both Sweden, as well as in the Indre Troms region and WGR in Norway (e.g. Brueckner & van Roermund, 2004; Gee et al., 2020; Mørk et al., 1988; Stølen, 1994). The exact timing of pre-Scandian events in the WGR remains uncertain; they may represent a continuous process of contraction and partial subduction during closure of the Iapetus Ocean, or alternatively may have comprised independent episodes split by periods of tectonic quiescence (Brueckner

& van Roermund, 2004). Ordovician subduction events are broadly contemporaneous with early Palaeozoic ophiolite obduction events in the Norwegian Caledonides (e.g. Furnes et al., 1985, 2012) and the formation of volcanic arcs near Baltica (Claesson et al., 1983; Dallmeyer & Gee, 1986). Ophiolite obduction occurs in two distinct episodes: an older Cambrian–Early Ordovician phase at *c.* 500–470 Ma and a younger Ordovician–Silurian phase at *c.* 440 Ma (Dunning & Pedersen, 1988; Pedersen & Dunning, 1997; Pedersen & Furnes, 1991).

The final phase of the Caledonian Orogeny in Scandinavia is termed the Scandian Orogeny (430–380 Ma). During the terminal Scandian collision, (1) the Iapetus Ocean closed and allochthonous terranes were thrust over the autochthonous Baltican basement from *c.* 430–415 Ma (Gee, 1975; Gee et al., 2013; Hacker & Gans, 2005; Roberts, 2003); (2) the Baltican basement and portions of overlying allochthons located beneath the edge of Laurentia experienced westward subduction to UHP depths (Andersen et al., 1998; Gee et al., 2013; Griffin & Brueckner, 1980; T.E. Krogh et al., 2011; Kylander-Clark et al., 2009; Root et al., 2005; Terry et al., 2000b); and finally, (3) the WGR underwent near-isothermal high-temperature exhumation to shallow mid-lower crustal levels (8–10 kbar) from *c.* 400 to 385 Ma (Andersen et al., 1998; Engvik et al., 2018; Hacker, 2007; Holmberg et al., 2019; Terry et al., 2000b; Tucker et al., 2004; Walsh & Hacker, 2004; Walsh et al., 2007). A two-stage exhumation is suggested for the UHP rocks of the WGR, including (1) rapid buoyancy-driven exhumation from the mantle to crustal depths (e.g. Andersen et al., 1991) and (2) a slower period of crustal exhumation related to extension (e.g. Walsh et al., 2013).

The Scandian Laurentia-Baltica collision and exhumation resulted in the exposure of high-pressure (HP) and UHP terranes across the Baltican margin. The spatial distribution of coesite-bearing eclogites and $^{40}Ar/^{39}Ar$ ages have been used to conclude that these UHP terranes outcrop in three east-southeast plunging antiforms along the west coast: Nordøyane, Sørøyane, and Nordfjord (Figure 1; Root et al., 2005). The WGR is structurally imbricated by discontinuous remnants of Caledonian thrust nappes that were later infolded along major foreland-verging shear zones, one of which is the Seve-Blåhø nappe on the island of Fjørtoft (e.g. Majka et al., 2014; Roberts & Gee, 1985).

2.2 | Metamorphism of the Western Gneiss Region

Incomplete overprinting reactions have allowed the sequence of metamorphic events in the WGR to be

relatively well constrained (Bryhni & Andréasson, 1985). Mesoproterozoic-aged metamorphism was associated with peak conditions of ~800–900°C and 10 kbar (Corfu & Andersen, 2002; Root et al., 2005; Tucker et al., 1990). Relics of this event within the WGC are rare but tend to be more prevalent within allochthons that were thrust over the Baltican basement during the early stages of the Caledonian Orogeny (Jolivet et al., 2005). Garnet Sm–Nd and Lu–Hf dating has shown that garnet in some high and ultrahigh-pressure locations formed during the late Mesoproterozoic and early Neoproterozoic, ascribing a polymetamorphic character to some high-P assemblages (Root et al., 2005; Simpson et al., 2021; Tamblyn et al., 2021). Low H_2O activity, coarse grain size, and limited deformation have been attributed to the sporadic preservation of these granulite facies assemblages during the subsequent Caledonian Orogeny (Austrheim, 1987; Krabbendam et al., 2000).

Pre-Scandian Caledonian tectonic events potentially involved multiple episodes of amphibolite facies metamorphism, with peak conditions of ~725°C and 12 kbar recorded in allochthons (Gee, 1975; Hacker & Gans, 2005). Allochthonous terranes were outboard from the main Baltican continent during these pre-Scandian events, and as a result, this phase of the Caledonian Orogeny is not recorded within the WGC basement.

Scandian subduction of the Baltican margin beneath Laurentia resulted in widespread HP–UHP metamorphism, evidenced by the presence of mantle peridotites, eclogites, and eclogite facies metagabbros (Cuthbert et al., 2000; van Roermund & Drury, 1998; Wain, 1997). Eclogites from these regions record *P–T* conditions of 15–39 kbar and 600–820°C with ages ranging between *c.* 420 and 400 Ma and an overall northwestward increasing *P–T* gradient (Butler, 2013; Carswell et al., 2003; Carswell et al., 2006; Cuthbert et al., 2000; Hacker et al., 2010; T.E. Krogh et al., 2011; Kylander-Clark et al., 2007, 2009; Labrousse et al., 2004; Mearns, 1986; Mørk & Mearns, 1986; Root et al., 2004, 2005; Wain, 1997; Young et al., 2007). Nordfjord records the transition between HP quartz eclogites (~600°C and 24 kbar) and UHP coesite- and microdiamond-bearing eclogites (750°C and >35 kbar; Cuthbert et al., 2000; Young et al., 2007; Smith & Godard, 2013). North of Nordfjord, Sørøyane experienced peak conditions of ~795°C and 32 kbar (Carswell et al., 2003; Root et al., 2004). Nordøyane records the maximum *P–T* conditions across the WGR, with eclogites and microdiamond- and/or coesite-bearing assemblages giving peak conditions of 820–850°C and 38–39 kbar (Carswell et al., 2006; Terry et al., 2000b).

The late Scandian exhumation of the WGR imparted a pervasive amphibolite facies overprint with local partial melting (e.g. Engvik et al., 2018; Holmberg et al., 2019; Kylander-Clark et al., 2008; Tucker et al., 2004). Recorded conditions during exhumation spanned 650–800°C and 5–15 kbar, largely destroying the record of UHP metamorphism (e.g. Dransfield, 1994; Engvik et al., 2018; Holmberg et al., 2019; Labrousse et al., 2004; Root et al., 2005; Walsh & Hacker, 2004). It has been suggested in some studies that the paucity of UHP mineral assemblages in the WGR could be the result of the metastability of pre-Caledonian lower-P mineral assemblages, rather than retrograde recrystallization after HP–UHP conditions (Garber et al., 2017; Krabbendam et al., 2000; Peterman et al., 2009; Spencer et al., 2013; Wain et al., 2001; Young & Kylander-Clark, 2015).

Previous temperature and age constraints for the retrograde history of the WGR have relied on three approaches, (1) U–Pb dating of eclogite facies zircon (Carswell et al., 2003; T.E. Krogh et al., 2011; Root et al., 2004; Young et al., 2007), (2) the dating of minerals with well-defined closure temperatures, that is, $^{40}Ar/^{39}Ar$ white muscovite dates (Walsh et al., 2013) in combination with U–Pb titanite and rutile (Butler et al., 2018; Root et al., 2005; Schärer & Labrousse, 2003; Spencer et al., 2013), and (3) dating of minerals associated with late igneous intrusions and melting (T.E. Krogh et al., 2011; Kylander-Clark & Hacker, 2014; Vrijmoed et al., 2013). Based on the combination of these results, the terminal stages of exhumation and cooling in the WGR appear to have been comparatively slow, with eclogite facies metamorphism concluding at c. 400 Ma, followed by systematic exhumation and cooling. Parts of the WGR are thought to have remained above the closure temperature of rutile (∼600°C) until as late as c. 374 Ma (Butler et al., 2018; T.E. Krogh et al., 2011; Kylander-Clark et al., 2008).

2.3 | Past geochronological work in Nordøyane and Sørøyane

Past Caledonian geochronological work for the Nordøyane and Sørøyane UHP terranes is summarized in Tables S1 and S2.

Oceanic and continental allochthons were metamorphosed and juxtaposed onto the WGC during the Caledonian Orogeny from c. 430 to 410 Ma as the Iapetus ocean closed (e.g. Hacker & Gans, 2005). The collision and westward, oblique subduction of Baltica beneath Laurentia (Bottrill et al., 2014) resulted in UHP metamorphism of the Baltican basement and overlying

allochthons from c. 425 to 400 Ma (e.g. Andersen et al., 1991; Kylander-Clark et al., 2007; Root et al., 2005). This was followed by exhumation of the WGR to shallow crustal depths between c. 400 and 374 Ma (e.g. Butler et al., 2018; Carswell et al., 2003; T.E Krogh et al., 2011; Kylander-Clark et al., 2008; Kylander-Clark & Hacker, 2014; Root et al., 2004, 2005; Schärer & Labrousse, 2003; Spencer et al., 2013; Tucker et al., 2004; Vrijmoed et al., 2013; Walsh et al., 2013; Young et al., 2007).

Though the WGR is largely dominated by Scandian-aged metamorphism (425–400 Ma), a notable record of pre-Scandian ages (505–430 Ma) has been recorded at both the Fjørtoft and Ulsteinvik localities. DesOrmeau et al. (2015) showed a nearly continuous spread of concordant Caledonian zircon ages from eclogites at Ulsteinvik, spanning from 475 to 430 Ma. This record pre-dates the dominant phase of Scandian UHP metamorphism and corroborates the hypothesis that Ulsteinvik may record an allochthonous history (Root et al., 2005). In Fjørtoft, Liu and Massone (2019) determined a similar, continuous record of monazite dates from c. 460–380 Ma, Walczak et al. (2019) of c. 450–400 Ma zircon growth, and Tual et al. (2020) of c. 450–350 Ma monazite growth. This protracted period of mineral (re)crystallization is suggested to be the result of multiple events or a prolonged residence time in the mantle at high temperatures.

The record of Scandian UHP metamorphism has been documented in many studies. U–Pb geochronology indicates protracted zircon growth at UHP conditions, with ages ranging from 420 to 400 Ma in Nordøyane (e.g. T.E. Krogh et al., 2011; Kylander-Clark et al., 2013), and similar, but slightly younger ages of c. 412–401 Ma in Sørøyane (e.g. Carswell et al., 2003; DesOrmeau et al., 2015; Root et al., 2004; Tucker et al., 2004). Recent studies have combined Lu–Hf and Sm–Nd isotopic systems in mafic eclogites across the WGR to document a ∼20 Myr period from c. 419–397 Ma over which garnet growth is interpreted to have occurred during eclogite facies metamorphism (Cutts & Smit, 2018; Kylander-Clark et al., 2007, 2009). Laser ablation split stream (LASS) analysis of monazite from quartzofeldspathic mylonite neighbouring the Hareidlandet-Dimnøya eclogite gave three variably discordant Caledonian intercept ages at 426.9 ± 5.6 Ma, 394.8 ± 1.2 Ma, and 390.0 ± 2.1 Ma (Holder et al., 2015). In addition, a LASS study of monazite in garnet-muscovite-kyanite gneiss from Leinøya, Sørøyane, yielded four weighted-mean $^{206}Pb/^{238}U$ ages between c. 405 and 390 Ma (Kylander-Clark et al., 2013). Rare-earth element (REE) compositions of these monazites were interpreted to record monazite (re)crystallization in the presence of garnet at c. 427–395 Ma and plagioclase breakdown and

recrystallization between *c.* 427 and 390 Ma. Monazite U–Th–Pb geochronology of the 'diamondiferous' Fjørtoft gneiss has given predominantly Scandian ages of *c.* 431–395 Ma (Hacker et al., 2015; Terry et al., 2000b), although some ages are as early as *c.* 460 Ma (Liu & Massone, 2019). A similar LASS U–Pb monazite study of the same diamondiferous gneiss gave Caledonian dates spanning from *c.* 430 to 390 Ma (Holder et al., 2015).

Zircon, muscovite, titanite, and rutile data have been used to constrain the retrograde history of the WGR. By analysing the spatial distribution of *P–T* estimates (calculated via equilibrium reactions), Walsh and Hacker (2004) were able to infer that the WGR had stalled at a depth of ~40 km. Zircon, monazite, and titanite record widespread resetting of Pb across the WGR at *c.* 395 Ma, suggesting that this stalling was regionally synchronous (Tucker et al., 1987, 1990). Upper amphibolite facies retrogression is constrained by zircon U–Pb ages from late pegmatites that cross cut older fabrics to between 395 and 390 Ma (T.E. Krogh et al., 2011). ^{40}Ar/^{39}Ar white mica dating in the WGR found that muscovite closed to Ar loss over a ~20 Myr period, spanning from *c.* 400 Ma at the eastern edge to *c.* 380 Ma in the west (Hacker, 2007; Walsh et al., 2013; Warren et al., 2012), documenting the timing of cooling through ~400–450°C (Harrison et al., 2009). Titanite ages record east-to-west younging across the WGR from *c.* 415 to 375 Ma (Garber et al., 2017; Kylander-Clark et al., 2008; Tucker et al., 2004). Rutile age data suggest that parts of the WGR remained above 600°C until as late as *c.* 374 Ma (Butler et al., 2018; T.E. Krogh et al., 2011; Kylander-Clark et al., 2008).

2.4 | Samples

Metapelitic samples with inferred UHP histories were collected for this study. Sample WGC2019J-25B was collected from an outcrop in Ulsteinvik (32V 335031 6916093, WGS 84 UTM) and is proximal to the UHP Hareidland eclogite (Mysen & Heier, 1972). Sample WGC2019J-31A was collected from what is assumed to be the Seve-Blåhø nappe on the island of Fjørtoft (32V 368303 6956199, WGS 84 UTM). Both samples are garnet-kyanite metapelitic gneisses (Figure 2).

3 | METHODS

3.1 | Whole-rock geochemistry

Whole-rock chemical compositional data required for mineral equilibria modelling was acquired at Bureau
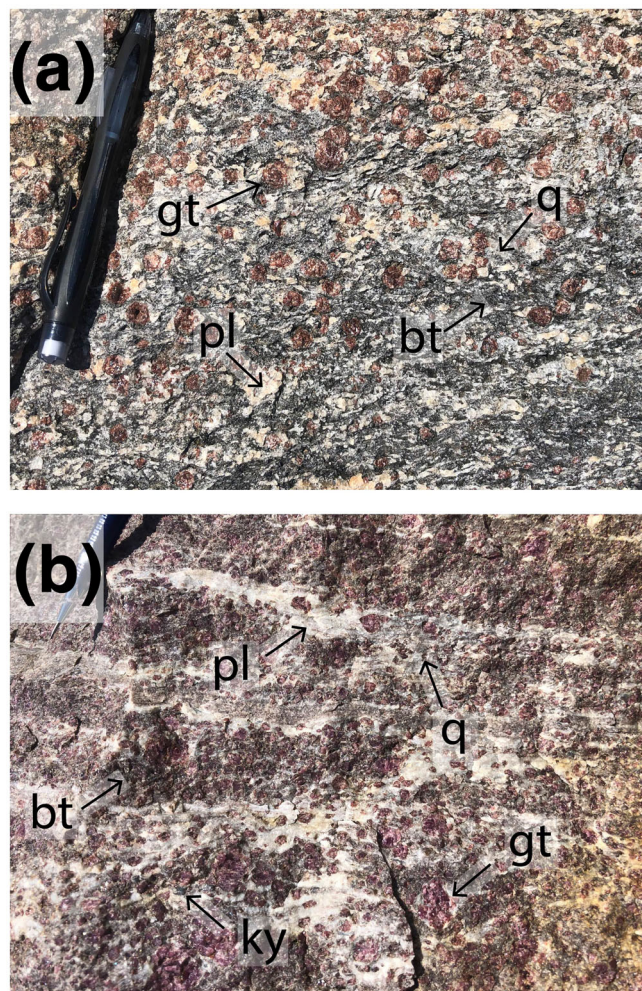

FIGURE 2 Field photos from sample locations. (a) Ulsteinvik WGC2019J-25B: garnet-kyanite-plagioclase-biotite-bearing gneiss. Annotations: gt = garnet, ky = kyanite, pl = plagioclase, bt = biotite, q = quartz. (b) Fjørtoft WGC2019J-31C garnet-kyanite-biotite metapelite with K-feldspar-plagioclase domains, suggestive of partial melting [Colour figure can be viewed at wileyonlinelibrary.com]

Veritas, Adelaide. Geochemical data are presented in Table S3.

3.2 | Electron Probe Micro Analyses (EPMA)

Mineral composition element analyses were acquired at Adelaide Microscopy, using a CAMECA SXFive Electron Probe Microanalyser. The instrument is equipped with five wavelength-dispersive spectrometers and runs PeakSite v6.4 software for microscope operation, and Probe for EPMA software. Alkali element migration and beam damage were mitigated through using a defocused electron beam and mean atomic

number (MAN) background correction (Donovan et al., 2016; Donovan & Tingle, 1996). Mobile elements (Na, F, and Cl) were analysed first on the detector, using the time-dependent intensity (TDI) correction feature of Probe (Donovan & Rowe, 2005). The decay of X-ray counts over time can then be measured and modelled to return a $t = 0$ intercept, allowing a concentration to be calculated.

Minerals were analysed using a 20 nA beam current, 15 kV accelerating voltage, and a 5 μm spot size. Oxygen was calculated by stoichiometry and assumed that all Fe was Fe^{2+}, following matrix corrections of Armstrong-Love/Scott φ (ρz) (Armstrong, 1988). Henke MACs were used for data reduction. Cl, Ca, K, and Ba were measured using the PET crystal; F on the PC0; Ti and P on the PET; Na, Si, Mg, and Al on the TAP; and Fe, Mn, Cr, and Ni on the LIF. The following standards were used: Cl – tugtupite, Ca – wollastonite, K – orthoclase, Ba – barite, F – MgF_2, P – apatite, Ti – rutile, Na, Si – albite, Mg – olivine, Al, Fe – almandine garnet, Mn – rhodonite, Cr – chromium oxide, Ni – nickel olivine.

Elemental X-ray maps for garnet and cordierite-spinel reaction textures were also acquired at Adelaide Microscopy, using the CAMECA SXFive Electron Microprobe. A beam current of 200 nA, an accelerating voltage of 20 kV, a dwell time of 30 μs, and a step size of 4–16 μm were used.

Mineral formula stoichiometric charge balanced mineral recalculations (Droop, 1987) were then used to calculate the amount of Fe^{3+} present in iron-bearing minerals within the samples as a general compositional range to locate mineral oxidation state modelling.

3.3 | Imaging

A FEI Quanta 450 scanning electron microscope (SEM) with an attached Oxford Ultim Max Large Area energy dispersive spectrometer (EDS) detector at Adelaide Microscopy, Australia, was used to image monazite from both samples and WGC2019J-25B zircon. Cathodoluminescence (CL) images for zircon were acquired using a spot size of 7.2 μm, an accelerating voltage of 15 kV, and a working distance of 17 mm. Backscattered electron (BSE) images for monazite used a spot size of 4 μm, an accelerating voltage of 20 kV, and a working distance of 10 mm.

Zircons from WGC2019J-31A were imaged using the Quanta600 SEM at Adelaide Microscopy. CL images were acquired using a spot size of 7 μm, an accelerating voltage of 15 kV, and a working distance of 15 mm.

Backscattered electron (BSE) imaging and compositional characterization of former melt inclusions in garnet was done using a Sigma Zeiss Field Emission Scanning Electron Microscope (FESEM) equipped with Oxford XMax EDS Silicon Drifted detector at the CNR-IENI, Padova. Analytical conditions used were a spot size of ∼1 μm, an accelerating voltage of 20 kV and a working distance varying from 7 to 12 mm.

TABLE 1 LA–ICP–MS operating conditions

Mineral	Sample/Analysis type	Spot size (μm)	Fluence (J/cm²)	Energy (mJ)	Frequency (Hz)	Scan speed (μm/s)
Zircon	WGC2019J-25B spot data	19	2	28	5	-
	WGC2019J-31A spot data	19	2	30	5	-
Monazite	WGC2019A-3 spot data	19	2	33	5	-
	WGC2019J-25B spot data	19	2	33	5	-
	WGC2019J-31A spot data	19	2	33	5	-
Rutile	WGC2019A-3 spot data	29	5	45	5	-
	WGC2019J-25B spot data	29	5	45	5	-
Apatite	WGC2019A-3 spot data	29	3.5	45	5	-
	WGC2019J-25B spot data	29	3.5	45	5	-
Garnet	WGC2019J-25B (1) spot data	51	3.5	45	5	-
	WGC2019J-25B (2) spot data	51	3.5	45	5	-
	WGC2019J-31A spot data	51	3.5	45	5	-
	WGC2019J-25B (1) map	61	3.5	45	10	90
	WGC2019J-25B (2) map	61	3.5	45	10	90
	WGC2019J-31A map	91	3.5	45	10	135

3.4 | LA–ICP–MS: Geochronology

Zircon, monazite, rutile, and apatite U–Pb isotopic data were acquired using a RESOlution LR 193 nm Excimer laser system and coupled Agilent 7700s ICP–MS at Adelaide Microscopy. Operating conditions are detailed in Table 1.

Zircon grains were separated using standard crushing, sieving, and panning procedures to be analysed in a grain mount. Additionally, sample WGC2019J-31A was processed with heavy liquid separation. Zircon Pb/U and Pb/Pb ratios were calibrated against primary standard GJ (608.5 ± 0.4 Ma; Jackson et al., 2004) and secondary standards Pleisovice (337.1 ± 0.4 Ma; Sláma et al., 2008) and 91500 (1065.4 ± 0.3 Ma; Wiedenbeck et al., 1995). In the WGC2019J-25B zircon run, Pleisovice and 91500 yield concordia ages of 339.2 ± 1.7 Ma ($n = 19$, MSWD = 1.3) and 1058.5 ± 10.8 Ma ($n = 10$, MSWD = 1.4), respectively. For WGC2019J-31A zircon, Pleisovice gives a concordia age of 338.2 ± 2.0 Ma ($n = 37$, MSWD = 2.1), and 91500 yields a concordia age of 1057.5 ± 5.2 Ma ($n = 38$, MSWD = 1.2).

Monazite for both samples were analysed in situ against primary standard, MAdel (518.4 ± 1 Ma; updated from Payne et al., 2008, with additional TIMS analysis), and secondary standards, Ambat (~525 Ma; in-house) and 222 (450.2 ± 3.4 Ma; in-house). Ambat calculates a concordia age of 518.1 ± 2.2 ($n = 13$, MSWD = 0.85), and 222 yields a concordia age of 450.6 ± 1.3 Ma ($n = 32$, MSWD = 0.86).

In situ analysis of apatite for WGC2019J-25B was calibrated against primary standard, MAD (486.6 ± 0.85 and 474.3 ± 0.4 Ma; Thomson et al., 2012), and secondary standards, McClure (523.5 ± 1.5 Ma; Schoene & Bowring, 2006) and 401 (530.3 ± 1.5 Ma; Thompson et al., 2016). During the analysis, McClure and 401 give concordia ages of 540.8 ± 21 Ma ($n = 22$, MSWD = 0.98) and of 541.3 ± 10.1 Ma ($n = 17$, MSWD = 2), respectively.

Rutile was analysed in situ across two separate runs. Samples were calibrated using the primary standard, R10 (1090 ± 5 Ma; Luvizotto & Zack, 2009), and secondary standard, R19 (489.5 ± 0.9 Ma; Zack et al., 2011). The first run incorporated analyses from both WGC2019J-25B and WGC2019J-31A, whilst the second included additional analyses from WGC2019J-25B. In the first run, R19 yields a concordia age of 496.2 ± 10.7 Ma ($n = 10$, MSWD = 1.9), and in the second run, R19 gives a concordia age of 485.5 ± 5.8 Ma ($n = 34$, MSWD = 1.4).

Data processing and reduction was completed using Iolite 3.6 software, where secondary standards were used to propagate the external precision of unknowns (Hellstrom et al., 2008; Paton et al., 2011).

3.5 | LA–ICP–MS: Trace elements

Trace element data for zircon, monazite, apatite, and rutile were acquired using a RESOlution LR 193 nm Excimer laser system and coupled Agilent 7700s ICP–MS at Adelaide Microscopy. Iolite 3.6 software (Hellstrom et al., 2008; Paton et al., 2011) was used for data processing and reduction. Synthetic glass NIST 610 was monitored to confirm the accuracy of trace element data reduction (Pearce et al., 2007).

For spot data, Zr^{91} was used as the internal standard for zircon (index content = 43.14%), Ce^{58} was used for monazite (index content = 20.00%), Ca^{20} for apatite (index content = 39.36%), and Ti^{22} for rutile (index content = 59.94%). Using the pressure dependent calibration defined by Kohn (2020), Zr concentrations (in ppm) were used to calculate temperature estimates for rutile. Similarly, Ti concentrations (in ppm) were used to constrain temperature estimates for zircon (Ferry & Watson, 2007).

3.6 | Mineral equilibria forward modelling

Mineral equilibria models were calculated using THERMOCALC v.3.40 software in the model system MnNCKFMASHTO (MnO-Na$_2$O-CaO-K$_2$O-FeO-MgO-Al$_2$O$_3$-SiO$_2$-H$_2$O-TiO$_2$-O) or in NCKFMASHTO (Na$_2$O-CaO-K$_2$O-FeO-MgO-Al$_2$O$_3$-SiO$_2$-H$_2$O-TiO$_2$-O), using the internally consistent thermodynamic dataset 'ds62' (Green et al., 2016; Holland & Powell, 2011). The most recent activity-composition (a–x) models (Diener & Powell, 2012; Green et al., 2016; Holland & Powell, 2003, 2011; Smye et al., 2010; White et al., 2000, 2014) were used to calculate P–T pseudosections for samples WGC2019J-25B and WGC2019J-31A. Activity-composition models are most applicable at pressures <15 kbar (White et al., 2014) and modelling exceeding these pressures is based on extrapolation. The details of phase-equilibria calculations at higher pressures on these diagrams should therefore be interpreted with caution.

Bulk compositions were calculated based on whole-rock geochemistry. P–Mo pseudosections were used to constrain the sensitivity of mineral assemblages to oxidation (Figures S1 and S2). The P–Mo models were constructed for a range of oxidation states (90% Fe$_2$O$_3$ to 10% Fe$_2$O$_3$) and were calculated at 790°C for a pressure range of 4 to 30 kbar. 790°C was chosen as the approximate temperature of peak metamorphism for the samples from Zr-in-rutile thermometry. Water content was determined by multiplying total wt% biotite in each sample by EPMA-calculated wt% H$_2$O in biotite. This was verified

via the calculation of PH$_2$O diagrams, which confirmed the position of prograde and peak assemblages at this calculated water content (Figures S3 and S4).

4 | RESULTS

4.1 | Petrography

4.1.1 | WGC2019J-25B

Garnet porphyroblasts of up to one centimetre in diameter sit within a weakly foliated matrix principally composed of kyanite, biotite, plagioclase and quartz. Similar to replacement textures recognized in past studies (e.g. Hacker et al., 2010; Holder et al., 2015; Peterman et al., 2009; Walsh & Hacker, 2004), plagioclase and a large proportion of biotite form coarse, elongate, symplectitic-style patches that are up to several centimetres long (Figure 3a). Biotite within these intergrowths is not consistently oriented. The textural association of the biotite-plagioclase intergrowths suggests they may have replaced one or more pre-existing minerals (e.g. Holder et al., 2015). Using 75 × 25 millimetre 600 dpi thin section scans, the region outlined by the boundaries of these domains comprises 26 volume % of the assemblage, with biotite accounting for 36 volume % of the total intergrowth (Appendix S1). Calculating the average of the biotite and plagioclase compositions and their proportions indicates that the present composition of the intergrowths contains ~50 wt% SiO$_2$ and 22 wt% Al$_2$O$_3$, along with significant amounts of Na$_2$O, K$_2$O, FeO, MgO, and TiO$_2$. In addition to occurring within these intergrowths, biotite also forms coarse-grained mono-mineralic domains within which crystals are roughly aligned and define a weak foliation (Figure 3a). Garnet comprises ~13.5 volume % of the assemblage. The cores of garnet porphyroblasts contain coarse-grained inclusions of quartz and plagioclase and smaller inclusions of kyanite, rutile, zircon, apatite, muscovite, and biotite (Figure 3f). Additionally, garnet contains small (<20 μm) polycrystalline inclusions consisting of quartz, plagioclase, biotite, and sometimes chlorite (Figure 4). These inclusions occur throughout garnet and likely represent crystallized melt inclusions, that is, nanogranitoids (Bartoli et al., 2016; Cesare et al., 2015). Assuming this interpretation is correct, these inclusions imply the presence of melt in the prograde history for WGC2019J-25B. Kyanite is irregularly shaped due to the formation of replacive retrograde minerals and contains inclusions of rutile, apatite, and quartz. Rutile is predominantly contained within garnet, but also occurs to a lesser extent in the matrix, with only two grains analysed

in this study. Apatite occurs as a coarse-grained (up to ~2000 μm) mineral within the matrix (Figure 3a) or as finer grained inclusions (~250 μm) inside garnet. Monazite is sparse, but may be up to 700 μm in size.

Based on existing minerals, the interpreted peak assemblage is garnet+kyanite+quartz+rutile +apatite±monazite. Additional to this, based on compositional criteria, biotite-plagioclase intergrowths (Figure 3a) could conceivably represent the replacement of phengite and omphacite. UHP minerals and quartz textures after coesite have been observed in rocks proximal to the metapelite sampled in this study (e.g. Carswell et al., 2003), suggesting the sample likely also experienced UHP conditions. Therefore, the full peak assemblage can be interpreted as garnet+kyanite+phengite +omphacite+rutile+apatite+coesite.

Garnet is commonly separated from biotite and kyanite by coronas of cordierite, and cordierite-spinel symplectites enclose kyanite and separate it from biotite (Figure 3b,c; Štípská et al., 2010; Baldwin et al., 2015). The cordierite-spinel symplectites occasionally contain ilmenite, but more commonly contain rutile. Kyanite is often enclosed by coronitic plagioclase (Figure 3e; Štípská et al., 2010). Despite textural evidence for biotite as a reactant in the formation of the cordierite-spinel symplectites, there is no K-bearing reaction product in the textures. In places, kyanite has inverted to sillimanite (Figure 3d; Carmichael, 1969; White et al., 2008), and in rare instances, sillimanite has acted as substrate for spinel nucleation. The inferred retrograde mineral assemblage is cordierite+spinel+sillimanite+plagioclase. However, volumetrically, the retrograde assemblage comprises less than 3% of the sample. Of the retrograde minerals, cordierite is the most diagnostic as it occurs throughout the rock, whereas spinel only occurs where there is an aluminosilicate substrate.

4.1.2 | WGC2019J-31A

Porphyroblastic garnet within WGC2019J-31A is up to 5 cm. Garnet contains inclusions of sillimanite, kyanite, biotite, pyrite, pyrrhotite, chalcopyrite, zircon, monazite, apatite, quartz, and graphite. With the exception of sillimanite, these inclusions are typically concentrated in a domain (~300 μm wide) that occurs at the rim in coarser-grained garnets (Figure 3g), and closer to the core in finer-grained garnets (Figure 3h). Sillimanite inclusions exclusively occur within the cores of coarse-grained garnets. Collectively, garnet comprises ~28 volume % of the sample.

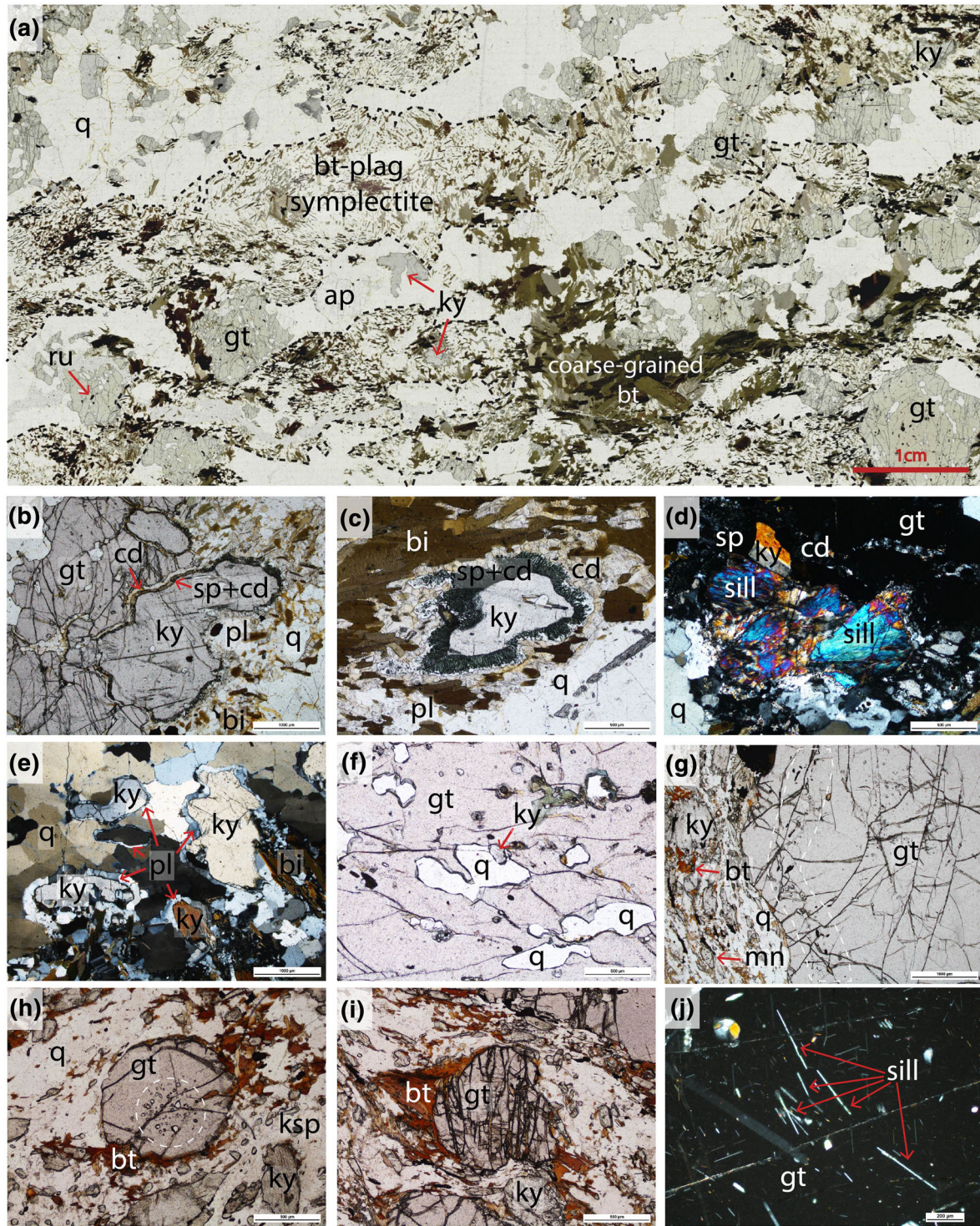Garnet grains are enclosed in a protomylonitic matrix consisting of plagioclase, K-feldspar, biotite, kyanite,

FIGURE 3 Photomicrographs from this study. (a) WGC2019J-25B: The textural setting of the rock. Fine-grained biotite-plagioclase-quartz domains that potentially formed after the breakdown of phengite and omphacite are outlined with a dashed line. (b) WGC2019J-25B: Porphyroblastic kyanite and garnet separated by symplectic cordierite and spinel, and a simple corona of cordierite. (c) WGC2019J-25B: Spinel-cordierite symplectite and cordierite corona isolating kyanite from biotite. (d) WGC2019J-25B. Sillimanite retrogression of kyanite. (e) WGC2019J-25B. Plagioclase coronas around kyanite. (f) WGC2019J-25B: Coarse-grained, gneissic inclusions inside garnet. (g) WGC2019J-31A. A trail of inclusions (dotted line) concentrated in the rim of a coarse-grained garnet porphyroblast. (h) WGC2019J-31A. Inclusions (dotted line) concentrated in the core of a fine-grained garnet porphyroblast. (i) WGC2019J-31A. A retrograde biotite strain shadow adjacent to porphyroblastic garnet. (j) WGC2019J-31A: Sillimanite inclusions inside garnet. Annotations: gt = garnet, ky = kyanite, pl = plagioclase, cd = cordierite, ksp = K-feldspar, bt = biotite, mn = monazite, q = quartz, ap = apatite, ru = rutile [Colour figure can be viewed at wileyonlinelibrary.com]
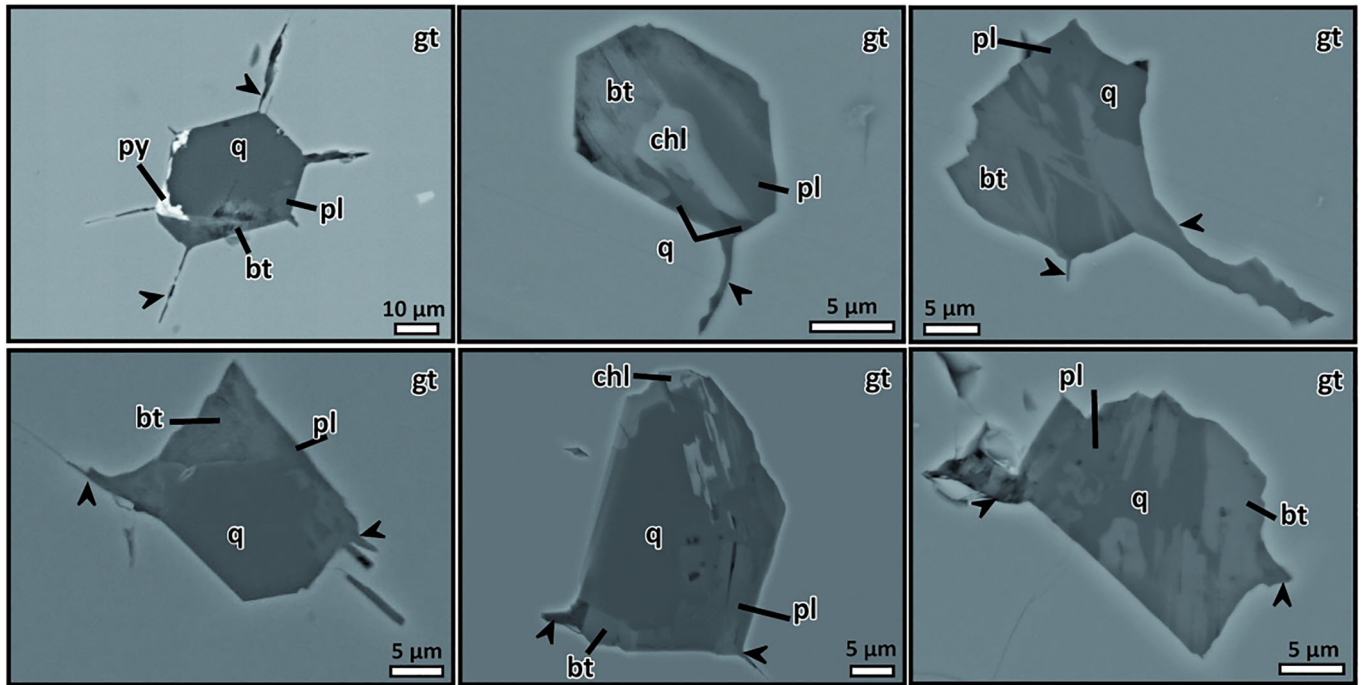
FIGURE 4 FESEM BSE images of nanogranitoids in garnet (gt) containing plagioclase (pl), quartz (q), biotite (bt), and less frequently, chlorite (chl) and pyrite (py) (sample WGC2019J-25B). Black arrows point to offshoots typical of decrepitated inclusions; note that some offshoots may show a radial arrangement around the inclusions (top left) [Colour figure can be viewed at wileyonlinelibrary.com]

quartz, rutile, pyrrhotite, chalcopyrite, muscovite, graphite, and monazite. Kyanite is deformed within this foliation and optically shows significant intragranular strain. Large grains of K-feldspar (<1000 μm) are enclosed by finer grained K-feldspar aggregates, suggesting they are relics that pre-date the development of the protomylonitic foliation. Late sillimanite is observed within the protomylonitic matrix, parallel to the pre-existing fabric. This defines an evolution from garnet+kyanite+muscovite+plagioclase+K-feldspar+rutile+quartz to garnet +sillimanite+muscovite+plagioclase+K-feldspar+rutile +quartz. The late-stage growth of biotite effectively makes the final assemblage sillimanite+muscovite+plagioclase+K-feldspar+rutile+quartz+biotite. Three textural types of biotite are present in the sample: (1) fine-grained inclusions within garnet and kyanite, (2) matrix, foliation defining biotite, and (3) retrograde biotite localized in strain shadows adjacent to garnet (Figure 3i). Possibly, the latter two are age equivalent. Monazite is typically <150 μm but can form grains up to ∼700 μm in size.

Due to the development of the late protomylonitic matrix foliation, determining the peak assemblage is difficult. However, it likely consisted of at least garnet +kyanite+muscovite+rutile+K-feldspar+quartz. The retrograde assemblage involved the formation of plagioclase and biotite in the presence of garnet and kyanite. If the prominent felsic domains in the outcrop (Figure 2b) represent melt, this may have also been a constituent of the retrograde assemblage.

4.2 | Mineral chemistry

Representative endmember compositions of garnet, plagioclase and K-feldspar are presented in Table 2. Table S4 contains representative electron microprobe analyses for each mineral, along with their respective cation calculations.

4.2.1 | Garnet

Garnet composition from WGC2019J-25B is dominantly almandine (Figure 5b; Table 2), with X_{alm} (Fe^{2+}/(Fe^{2+} + Ca + Mg + Mn)) values of 0.48–0.54 in garnet cores, 0.49–0.64 in garnet rims, and 0.64–0.71 in garnet partially consumed in retrograde reaction textures. Qualitative elemental maps (Figure 5a) and quantitative traverse data (Figure 5b) record prograde zoning. Almandine, grossular, and spessartine are enriched in WGC2019J-25B garnet cores and steadily decrease in concentration towards the rim. Pyrope is depleted within garnet cores and increases toward the rim.

TABLE 2 Summary of mineral chemistry for WGC2019J-25B and WGC2019J-31A

Mineral	End-member proportions	WGC2019J-25B Garnet rim	Garnet core	WGC2019J-25B reaction textures	WGC2019J-31A Garnet rim	Garnet core
Garnet	X_{gt}	0.59–0.73	0.60–0.70	0.65–0.73	0.65–0.74	0.67–0.72
	X_{alm}	0.49–0.64	0.48–0.54	0.64–0.71	0.59–0.67	0.63–0.68
	X_{py}	0.21–0.30	0.16–0.32	0.26–0.34	0.20–0.29	0.24–0.28
	X_{grs}	0.08–0.17	0.17–0.23	0	0.06–0.10	0.03–0.04
	X_{sps}	0.01–0.04	0.01–0.02	0.03–0.04	0.01	0.01–0.02
Plagioclase	X_{ab}	0.06–0.76		0.01–0.05	0.74–0.75	
	X_{an}	0.23–0.94		0.95–0.99	0.24–0.25	
K-Feldspar	X_{ab}	–		–	0.11–0.15	
	X_{or}	–		–	0.85–0.89	
Spinel	X_{sp}	0.61–0.65		0.72–0.78	–	
	ZnO (wt%)	1.43–2.36		–	–	
	Cr_2O_3 (wt%)	0.16–0.46		0.12–0.62	–	
	MnO (wt%)	0.08–0.21		0.13–0.22	–	
Biotite	X_{bi}	0.24–0.26		0.36–0.46	0.41–0.43	
	TiO_2 (wt%)	2.84–3.25		2.46–5.05	4.42–5.49	
	Al_2O_3 (wt%)	16.62–17.55		16.56–18.05	16.87–18.48	
	MnO (wt%)	−0.03–0.8		0	−0.02–0.08	
Cordierite	X_{crd}	–		0.22–0.25	–	
Ilmenite	MnO	–		0–0.42	–	
	TiO_2	–		44.01–47.98	–	

Note: Unless indicated otherwise by the units (wt%), proportions are atomic/molar. $X_{gt} = Fe^{2+}/(Fe^{2+} + Mg)$. $X_{alm} = Fe^{2+}/(Fe^{2+} + Mg + Ca + Mn)$. $X_{py} = Mg/(Fe^{2+} + Mg + Ca + Mn)$. $X_{gr} = Ca/(Fe^{2+} + Mg + Ca + Mn)$. $X_{sps} = Mn/(Fe^{2+} + Mg + Ca + Mn)$. $X_{ab} = Na/(Na + Ca)$. $X_{an} = Ca/(Ca + Na + K)$. $X_{or} = K/(Ca + Na + K)$. $X_{sp} = Mg/(Fe^{2+} + Mg)$. $X_{bi} = Fe^{2+}/(Fe^{2+} + Mg)$. $X_{crd} = Fe^{2+}/(Fe^{2+} + Mg)$.

Resorption in the outermost rim of garnet records a steep increase in almandine and spessartine concentrations and a decrease in pyrope and grossular (Figure 5a,c).

WGC2019J-31A garnet is principally almandine (X_{alm} = 0.59–0.68) and preserves a flat zoning profile (Figure 5d). Almandine and spessartine exhibit subtle rim-ward depletion. Pyrope records limited variation throughout the zoning profile. Grossular occurs in low concentrations and records a primarily flat profile that abruptly rises toward the rim (Figure 5c,g).

LA–ICP–MS trace element compositions for WGC2019J-25B and WGC2019J-31A garnet are presented in Table S5.

4.2.2 | Plagioclase

Plagioclase is present in both samples. WGC2019J-25B yields X_{an} (Ca/(Ca + Na + K)) values of 0.23–0.99 and X_{ab} (Na/Na + Ca) values of 0.01–0.076 (Table 2). Plagioclase that occurs in WGC2019J-25B reaction textures is more anorthitic (X_{an} = 0.95–0.99). WGC2019J-31A plagioclase calculates X_{an} values of 0.24–0.25 and X_{ab} values of 0.74–0.75.

4.2.3 | K-feldspar

K-feldspar occurs only in WGC2019J-31A. It records X_{ab} values of 0.11–0.15 and X_{or} (K/(Ca + Na + K)) values of 0.85–0.89 (Table 2).

4.2.4 | Spinel

Spinel is present in WGC2019J-25B. X_{sp} (Mg/(Fe^{2+} + Mg)) ranges from 0.61 to 0.78 and is higher in reaction texture spinel. It contains small amounts of ZnO, Cr_2O_3, and MnO.
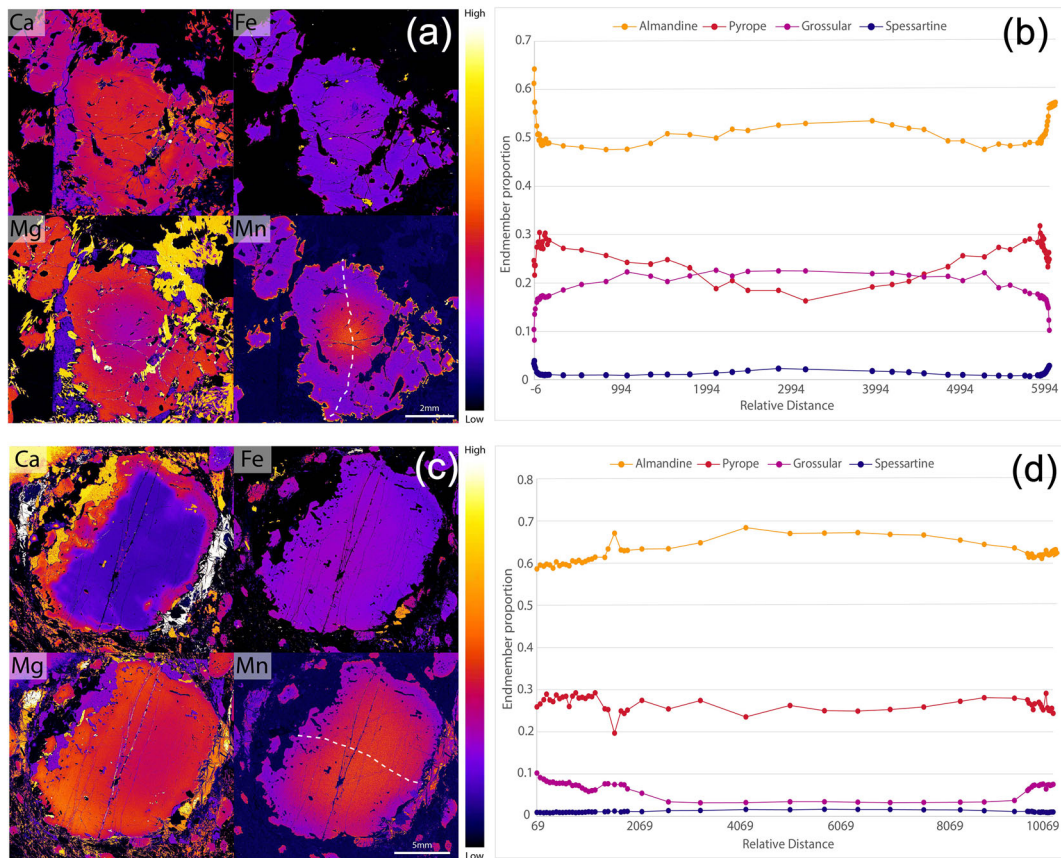
FIGURE 5 Garnet EPMA and LA–ICP–MS elemental maps and traverse data. *WGC2019J-25B:* (a) EPMA garnet major element maps for Ca, Fe, Mg and Mn. (b) EPMA garnet major element rim to rim traverse, showing end-member proportions. Traverse path is traced in Figure 4a with a dotted line. *WGC2019J-31A:* (c) EPMA garnet major element maps for Ca, Fe, Mg and Mn. (d) EPMA garnet major element rim to rim traverse, showing end-member proportions. Traverse path is traced in Figure 4d with a dotted line [Colour figure can be viewed at wileyonlinelibrary.com]
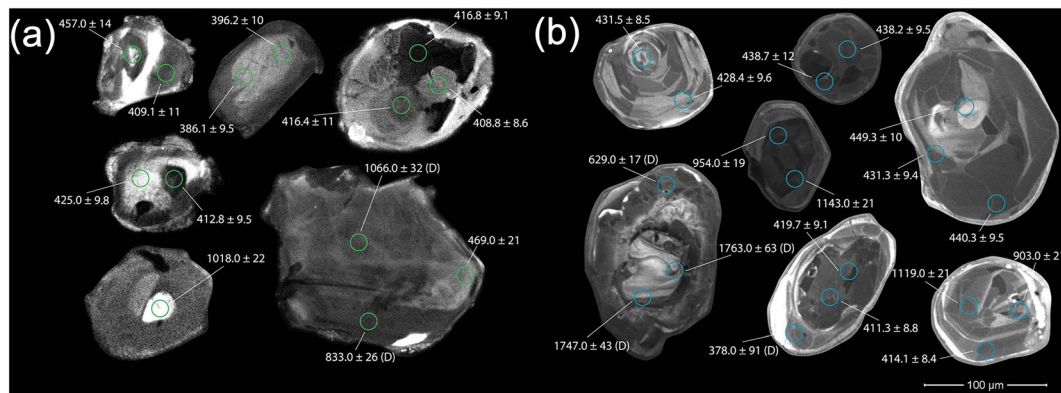
FIGURE 6 Representative examples of zircon SEM-CL metamorphic zoning in (a) Ulsteinvik (green), and (b) Fjørtoft (blue). Ages are in Ma. Discordant analyses are indicated by (D) [Colour figure can be viewed at wileyonlinelibrary.com]

4.2.5 | Biotite

X_{bi} ($Fe^{2+}/(Fe^{2+} + Mg)$) values in WGC2019J-25B range from 0.24 to 0.46, with reaction texture biotite recording the higher proportion of these values ($X_{bi} = 0.36$–

0.46). WGC2019J-31A records X_{bi} values between 0.41 and 0.43. TiO$_2$ in WGC2019J-25B biotite ranges from 2.46 to 5.05 wt%, while WGC2019J-31A is comparatively enriched, with values between 4.42 and 5.49 wt %.

4.2.6 | Cordierite

X_{crd} ($Fe^{2+}/(Fe^{2+} + Mg)$) in WGC2019J-25B reaction textures ranges between 0.22 and 0.25.

4.2.7 | Ilmenite

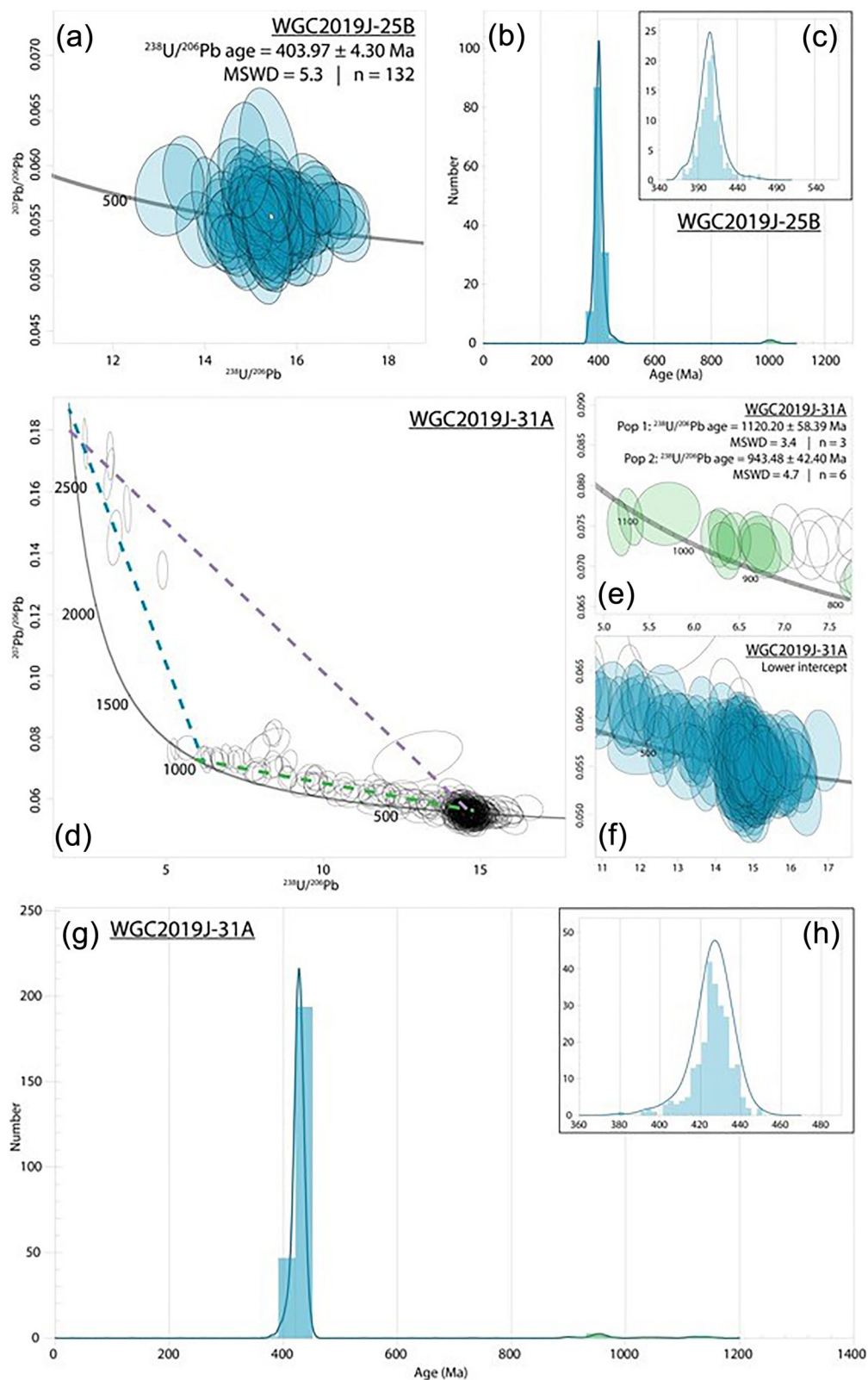Ilmenite in WGC2019J-25B has low MnO content, with values ranging between 0 and 0.42 wt%.

FIGURE 7 Zircon age data from Ulsteinvik and Fjørtoft. *WGC2019J-25B*: (a) U–Pb Tera Wasserburg concordia for concordant Palaeozoic-aged data, (b) Probability density plot for all concordant U–Pb ages, (c) Probability density plot for concordant Palaeozoic U–Pb ages. *WGC2019J-31A*: (d) U–Pb Tera Wasserburg concordia with potential discordia paths indicated by dashed lines, (e) U–Pb Tera Wasserburg concordia for Mesoproterozoic-aged data, where concordant data is coloured, (f) U–Pb Tera Wasserburg concordia for Caledonian-aged data, where concordant data is coloured, (g) Probability density plot for all concordant U–Pb ages, (h) Probability density plot for concordant Caledonian U–Pb ages [Colour figure can be viewed at wileyonlinelibrary.com]

4.3 | Zircon U–Pb geochronology and trace elements

U–Pb dating and trace element analysis was undertaken on mounted zircons from samples WGC2019J-25B and WGC2019J-31A. Calculated Tera-Wasserburg concordia plots and probability density plots are in Figure 7. Trace element REE spiderplots are shown in Figure 8. Extended morphological descriptions, U–Pb ratios, and trace element concentrations for zircon are in Tables S6 and S7.

4.3.1 | WGC2019J-25B

Zircons are ∼50–200 μm, sub-rounded to rounded and commonly display spectacular metamorphic patchy to polygonal sector zoning in CL (Figure 6). Analysis of 85 zircons reveal an almost continuous spread of dates from c. 470 to 370 Ma (Figure 7c), yielding a concordia date of 404.0 ± 4.3 Ma, with an MSWD indicating significant dispersion (MSWD = 5.3; Figure 7a). Two Proterozoic-aged analyses (c. 1009 Ma) were also recorded. Palaeozoic-aged zircons exhibit no significant Eu anomaly and (mean $Eu_N/\sqrt{(Sm_N*Gd_N)}$ = 1.1, n = 98) record a flat HREE slope (mean Lu_N/Gd_N = 2.6, n = 131), with the exception of the two oldest Palaeozoic-aged analyses (Lu_N/Gd_N = 25.5–86.8, n = 2). Late Mesoproterozoic-aged analyses have notably higher HREEs (Lu_N/Gd_N = 22.7–39.6, n = 2) and slightly negative Eu anomalies (Figure 8a).

4.3.2 | WGC2019J-31A

Zircons are ∼50–150 μm, are primarily equant and rounded, and display well-defined metamorphic internal morphology in CL similar to WGC2019J-25B, but with the occasional atypical dark core (Figure 6). One hundred seventy individual zircon grains generate a continuous range of dates spanning from the Proterozoic to the Palaeozoic. Differentiating precisely between concordant and discordant data is difficult due to the majority of discordia-defining analyses contacting the concordia (Figure 7d). As a result of this ambiguity, we do not attempt to assign a date to the lower intercept (Figure 7f). Three potential discordia lines are presented in Figure 7d based on the trend of data. Nine concordant analyses comprise two Proterozoic-aged populations, ranging from c. 1143 to 903 Ma (Figure 7e). Population 1 gives a date of 1120.2 ± 58.4 Ma (n = 3, MSWD = 3.4), and population 2 records a date of 943.5 ± 42.4 Ma (n = 6, MSWD = 4.7). Proterozoic-aged analyses occur exclusively within the dark cores of grains, but dark cores are not exclusively Proterozoic. REE patterns in Palaeozoic-aged grains are variably enriched in HREEs (Lu_N/Gd_N = 0.002–38.2, n = 242). Younger Palaeozoic-aged analyses record positive Eu anomalies and higher concentrations of Ce. Europium anomalies become increasingly negative and Ce concentrations progressively decrease with increasing age. Proterozoic-aged zircons have the most negative Eu anomalies and flat HREE slopes (Lu_N/Gd_N = 1.1–6.6, n = 9; Figure 8b).

4.4 | Monazite U–Pb geochronology and trace elements

In situ geochronology and trace element analysis were undertaken on monazite grains from various textural locations in samples WGC2019J-25B and WGC-2019J-31A. Table S8 contains morphological descriptions for monazite, and Table S9 presents LA–ICP–MS U–Pb ratios and trace element concentrations.
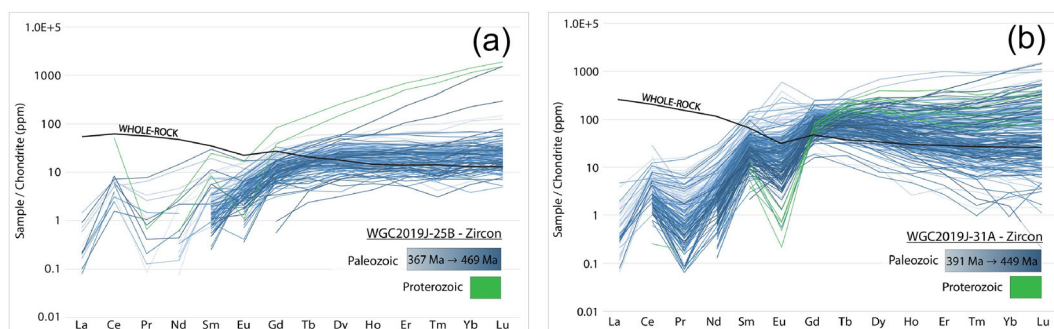

FIGURE 8 Chondrite-normalized zircon trace element data presented in REE spiderplots. Whole-rock compositions for each sample are represented by a black bold line. (a) WGC2019J-25B. (b) WGC2019J-31A. Spiderplots are coloured by age: Proterozoic = green, Palaeozoic = blue gradient, where pale blue lines represent younger zircon U–Pb ages [Colour figure can be viewed at wileyonlinelibrary.com]

4.4.1 | WGC2019J-25B

Monazite grains are not abundant and range in size from ~75 to 700 μm. Crystal habit is primarily anhedral, and BSE-defined zoning is either non-existent or weak. A total of eight monazite grains were analysed. Texturally, all grains are located within the matrix, with the exception of a single monazite inclusion within kyanite. LA–ICP–MS results from 164 analyses yield two discordant populations. These results are anchored to a common $^{207}Pb/^{206}Pb$ ratio of 0.8593 ± 0.00068 acquired from matrix biotite (Table S10) and yield well-defined dates of 401.9 ± 1.6 Ma and 376.7 ± 1.0 Ma ($n = 26$, MSWD = 0.5 and $n = 135$, MSWD = 1.7, respectively; Figure 9a). Population 1 (401.9 ± 1.6 Ma) consists of analyses from the monazite inclusion in kyanite. It is comparatively enriched in LREEs, less enriched in HREEs, and calculates a steep middle rare earth element (MREE) slope (average $Dy_N/Gd_N = 0.03$, $n = 26$) relative to population 2 (average $Dy_N/Gd_N = 0.09$, $n = 135$; Figure 11a). An Eu anomaly is absent in population 1. The majority of population 2 analyses record no Eu anomaly; however, four analyses have a negative Eu anomaly and are also enriched in HREEs relative to the remaining population.

4.4.2 | WGC2019J-31A

In situ WGC2019J-31A monazite grains range in size from ~75 to 700 μm, have variable crystal habit, and exhibit weak to no zoning in BSE. A total of 122 spots within 18 grains were analysed. Three populations are defined: 1053.2 ± 3.6 Ma ($n = 51$, MSWD = 4.9),

423.2 ± 2.0 Ma ($n = 49$, MSWD = 2.3), and 385.2 ± 6.7 Ma ($n = 2$, MSWD = 0.5; Figure 9b–d). The ages of populations 1 and 3 are given by concordia dates, and an age for population 2 is constrained by an anchoring $^{207}Pb/^{206}Pb$ value of 0.8437 ± 0.002 defined by biotite and K-feldspar $^{207}Pb–^{206}Pb$ composition (Figure 9d). Texturally, older dates tend to be associated with monazites that occur as inclusions within garnet on the inner side of the inclusion trail rims (Figure 3g). Figure 10a highlights the textural position of monazite dates, with the inset figure demonstrating the distribution and spatial organization of individual Palaeozoic and Mesoproterozoic dates from the matrix versus garnet side of a monazite grain partially included within garnet. There is a distinct relationship between dates and trace element concentration (Figure 11b). Population 2 is the most enriched in LREEs. All populations exhibit a negative Eu anomaly, with the Palaeozoic populations recording similar magnitudes (~0.2), and population 1 displays the most negative anomaly (~0.04). The HREEs are the most depleted in population 2 and the least depleted in population 3. All populations record a similar MREE slope.

4.5 | Apatite U–Pb geochronology and trace elements

4.5.1 | WGC2019J-25B

Geochronology and trace element analysis was undertaken in situ from WGC2019J-25B. Analysed grains range from ~250 to 2500 μm and occur in the matrix or within
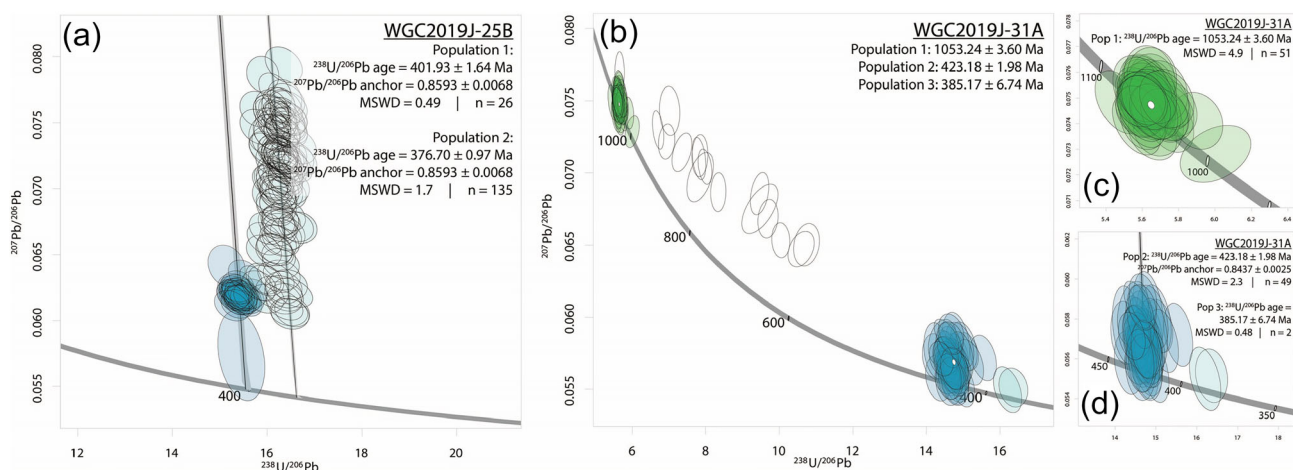

FIGURE 9 Tera Wasserburg concordia diagrams for monazite analyses from Ulsteinvik and Fjørtoft. Lower intercept ages for discordant or a combination of discordant and concordant data are anchored by a calculated $^{207}Pb/^{206}Pb$ ratio from biotite and K-feldspar (Table S10). (a) WGC2019J-25B. (b) WGC2019J-31A. (c) WGC2019J-31A upper intercept, showing Proterozoic analyses. (d) WGC2019J-31A lower intercept, showing Palaeozoic analyses. Ellipses are coloured based on population [Colour figure can be viewed at wileyonlinelibrary.com]
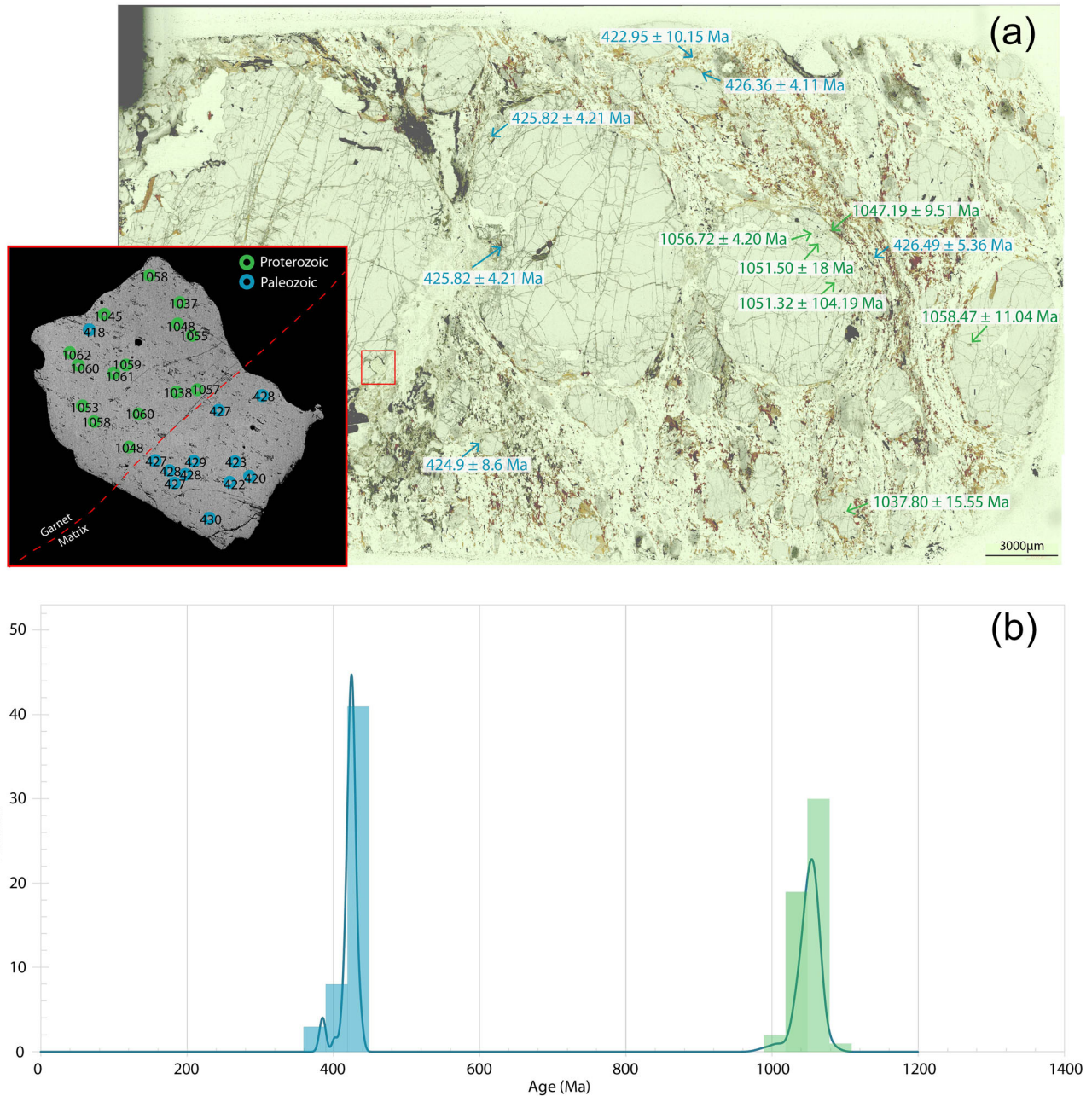
FIGURE 10 (a) WGC2019J-31A thin section scan annotated with monazite locations and weighted mean grain ages. Inset: monazite grain located at the edge of a garnet grain. A red dotted line marks the garnet grain boundary. (b) WGC2019J-31A cumulative probability distribution plot showing the spread of monazite data. In both plots: blue = Palaeozoic, green = Proterozoic [Colour figure can be viewed at wileyonlinelibrary.com]

garnet. An extended summary of morphology, LA–ICP–MS geochronology, and trace element data is presented in Tables S11 and S12. Nine apatite grains were analysed, totalling 183 analyses which plot discordantly on a Tera-Wasserburg concordia. Anchoring of these analyses using the biotite $^{207}Pb/^{206}Pb$ ratio (0.86 ± 0.01, $n = 16$, MSWD = 0.45) yields a date of 399.9 ± 1.9 Ma ($n = 183$,

MSWD = 1.5, Figure 12a). The HREE concentrations and Eu anomaly magnitude are directly related to textural location (Figure 12b); apatite analyses texturally included within garnet lack significant Eu anomalies and exhibit depletion in HREEs ($Lu_N/Gd_N = 0.0055$, $n = 33$), while matrix apatite has a negative Eu anomaly and is comparatively enriched in HREEs ($Lu_N/Gd_N = 0.087$, $n = 111$).
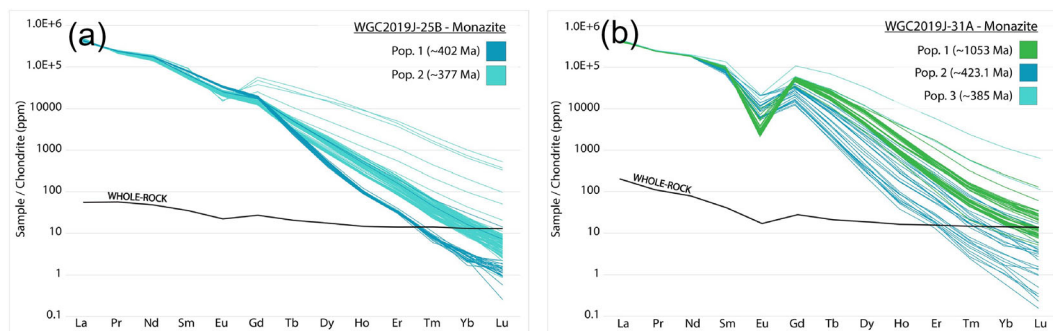
FIGURE 11 Chondrite-normalized monazite trace element data presented in REE spiderplots. Whole-rock compositions for each sample are represented by a black bold line. (a) WGC2019J-25B. (b) WGC2019J-31A. Plots are coloured by population. Green = Proterozoic, dark blue = old Palaeozoic, light blue = young Palaeozoic [Colour figure can be viewed at wileyonlinelibrary.com]
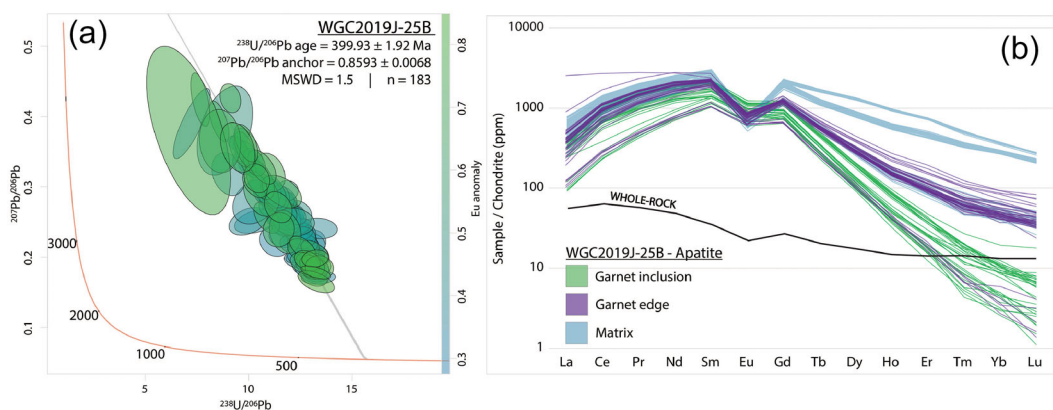

FIGURE 12 Ulsteinvik apatite geochronology and trace element data. (a) Tera Wasserburg concordia anchored by $^{207}Pb/^{206}Pb$ from biotite and coloured by the magnitude of Eu anomaly. (b) REE spiderplot for chondrite-normalized apatite trace element data coloured by textural location. Whole-rock compositions for each sample are represented by a black bold line [Colour figure can be viewed at wileyonlinelibrary.com]

4.6 | Rutile U–Pb geochronology

Geochronology and trace element analysis of in situ rutile was undertaken for WGC2019J-25B and WGC2019J-31A. Extended morphology descriptions and results are presented in Tables S13 and S14.

4.6.1 | WGC2019J-25B

Rutile grains vary in size between 50 and 400 μm and, with the exception of two matrix grains, occur as inclusions in garnet. Out of 249 total analyses, 86 are concordant. These analyses define a spread from *c.* 453 to 358 Ma (Figure 13b), giving a concordia date of 403.8 ± 8.7 Ma (*n* = 86, MSWD = 0.3) with significant dispersion, suggesting the data do not represent a single age population (Figure 13a).

4.6.2 | WGC2019J-31A

Seventeen rutile grains ranging in size between 50 and 650 μm and from both matrix and inclusions in garnet were analysed, totalling 31 analyses. Twenty-one of these analyses plot concordantly, defining an almost continuous spread from *c.* 449 to 379 Ma (Figure 13d) and giving a concordia date of 400.0 ± 12.5 Ma (MSWD = 1.4; Figure 13c).

4.7 | Zr-in-rutile thermometry

Trace element compositions of rutile were used for Zr-in-rutile thermometry in samples WGC2019J-25B and WGC2019J-31A (Kohn, 2020). Analyses exceeding 10,000 ppm Zr likely represent zircon inclusions within rutile and are excluded.
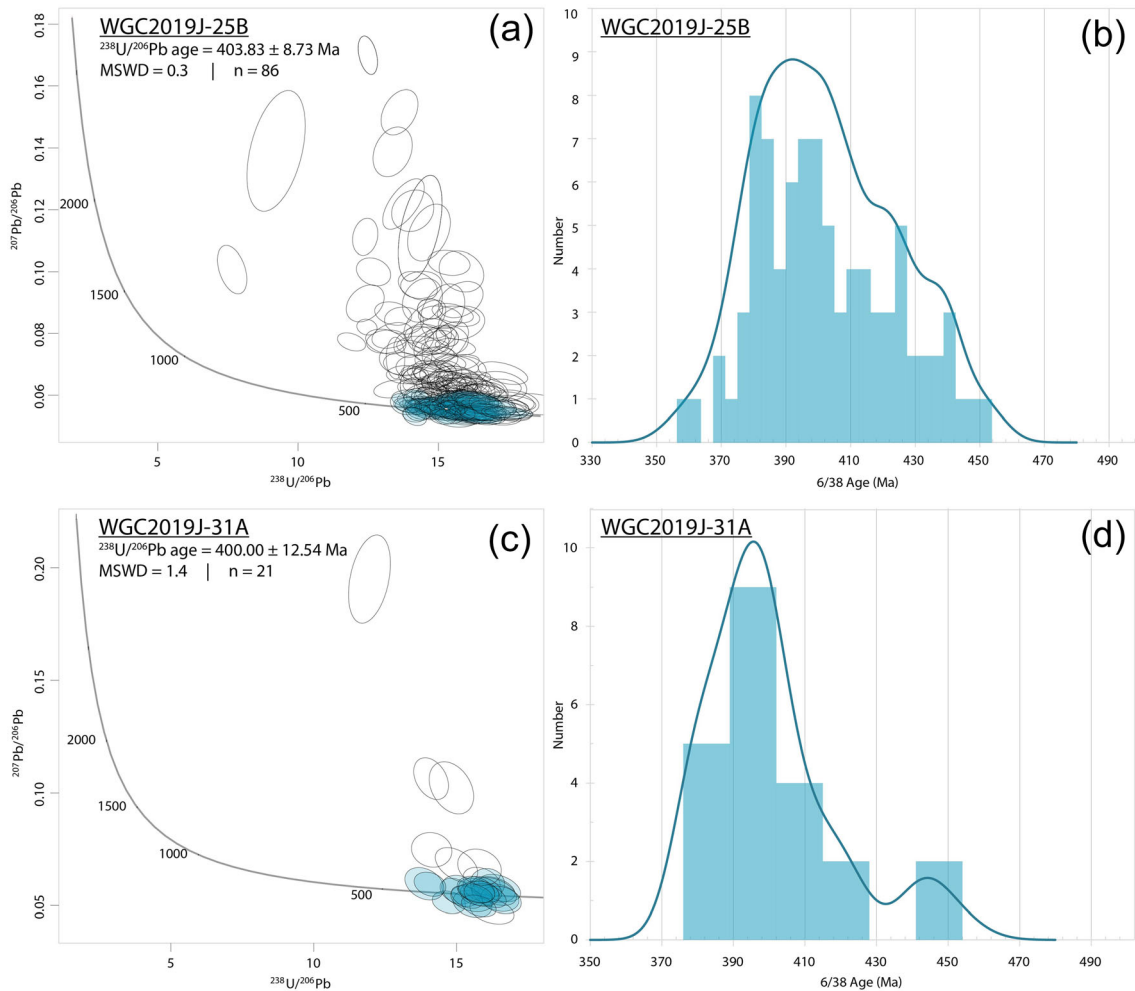
FIGURE 13 Rutile age data. (a) WGC2019J-25B Tera Wasserburg concordia, (b) WGC2019J-25B cumulative probability distribution plot, (c) WGC2019J-31A Tera Wasserburg concordia, (d) WGC2019J-31A cumulative probability distribution plot [Colour figure can be viewed at wileyonlinelibrary.com]

Zr-in-rutile temperatures for WGC2019J-25B were separated by textural setting and calculated at 10 kbar (Figure 16), using the calculation assigned by Kohn (2020). Rutile inclusions in garnet cores define three populations: $695 \pm 3°C$, $655 \pm 4.8°C$, and $391 \pm 36°C$; rutile in garnet rims defines four populations: $698 \pm 4.1°C$, $649 \pm 5.4°C$, $526 \pm 23°C$, and $385 \pm 19°C$; and matrix rutile defines one population: $653 \pm 8°C$. The combination of all data defined four populations: $698 \pm 2°C$, $652 \pm 3°C$, $559 \pm 16°C$, and $387 \pm 19°C$. The majority of analyses (94%) fit into populations 1 ($698 \pm 2°C$) and 2 ($652 \pm 3°C$). Population 2 is recorded by rutile contained within the matrix, garnet cores, and garnet rims, whilst population 1 is only recorded in rutile inclusions inside garnet.

At 18 kbar, WGC2019J-31A Zr-in-rutile temperatures from matrix grains define one population at $756 \pm 5.4°C$.

There is little to no correlation between calculated temperature and age in either WGC2019J-25B or WGC2019J-31A. Extended thermometry data are in Table S14.

4.8 | Ti-in-zircon thermometry

Trace element compositions of zircon were used for Ti-in-zircon thermometry in samples WGC2019J-25B and WGC2019J-31A (Ferry & Watson, 2007). WGC2019-25B calculates temperatures ranging from 574 to 828°C. The unmix algorithm in Isoplot v. 4 defines two populations: $705 \pm 12°C$ (34%) and $659 \pm 10°C$ (66%) with a combined misfit of 0.990 (Table 3). WGC2019J-31A records temperatures spanning between 573 and 898°C and calculates three populations: $853 \pm 27°C$ (4%), $758 \pm 8°C$ (44%), and $662 \pm 9°C$ (52%) with a combined misfit of 0.859.

T A B L E 3 Average Zr-in-rutile temperatures for WGC2019J-25B and WGC2019J-31A data

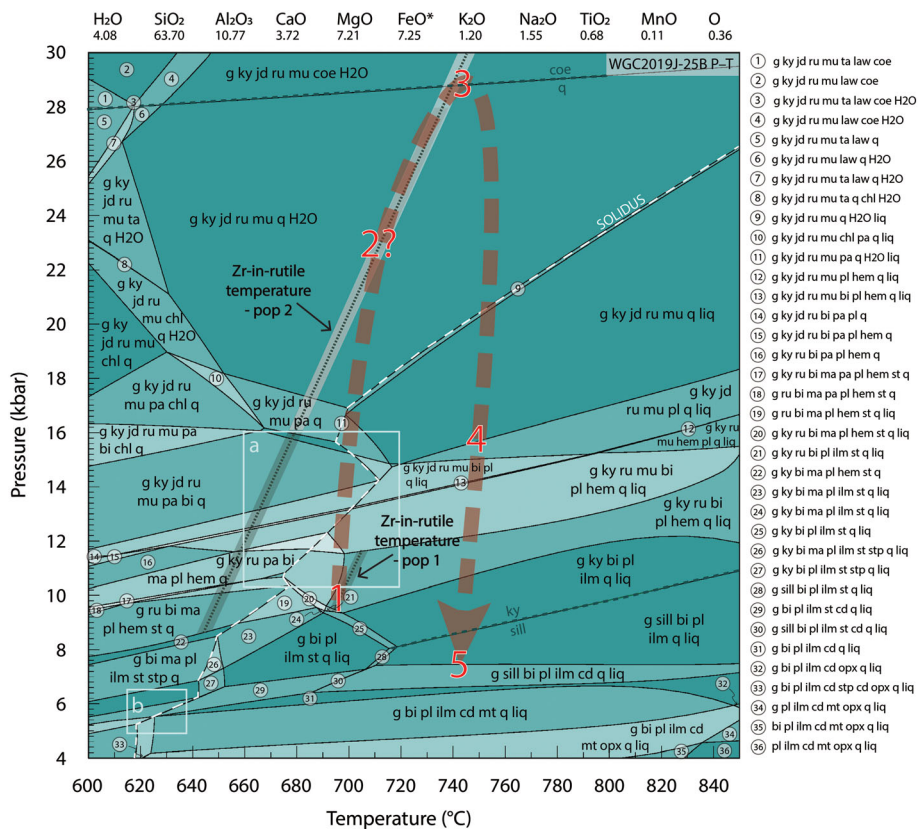| Sample		Ti-in-zircon temperature (°C) (Ferry & Watson, 2007)	Zr-in-rutile temperature (°C) (Kohn, 2020)	
WGC2019J-25B	Population 1	705 ± 12°C (34%)	At 10 kbar	698 ± 2°C (57%)
	Population 2	659 ± 10°C (66%)		652 ± 3°C (37%)
	Population 3	-		559 ± 16°C (3%)
	Population 4	-		387 ± 19°C (3%)
WGC2019J-31A	Population 1	853 ± 27°C (4%)	At 18 kbar	
	Population 2	758 ± 8°C (44%)		756 ± 5.4°C (100%)
	Population 3	662 ± 9°C (52%)		

F I G U R E 1 4 *P–T* pseudosection for metapelite WGC2019J-25B. The red arrow represents the inferred *P–T* path, defined by points 1–5. Point 1 identifies the prograde field. Point 2 is imprecisely determined by population 2 Zr-in-rutile temperatures and may exist anywhere along this contour. The minimum peak pressure constraint is defined by Point 3. Point 4 represents the c. 400 Ma arrival of plagioclase, as indicated by apatite. Point 5 defines a *P–T* point calculated from a retrograde bulk composition. Variance increases with shading in the diagram. Magnified insets of complex regions (a) and (b) are contained in Figure S5. Bulk composition used for the calculation of the phase diagram is listed in mol.% at the top of the diagram. Oxidation (M_O) was constrained at 0.15 (see additional PM_O pseudosection in Figure S1). Zr-in-rutile temperature populations are contoured with a dashed line with the surrounding shaded area representing associated errors. Black shading indicates potential biotite breakdown or rutile recrystallization, and white can only result from rutile recrystallization. Inset fields are provided in Figure S5. Abbreviations: g = garnet, ky = kyanite, sill = sillimanite, jd = jadeite, ru = rutile, mu = muscovite, ta = talc, law = lawsonite, pa = paragonite, ma = margarite, bi = biotite, chl = chlorite, pl = plagioclase, hem = hematite, ilm = ilmenite, st = staurolite, stp = stipnomelane, q = quartz, mt = magnetite, opx = orthopyroxene, cd = cordierite, liq = liquid, H_2O = water [Colour figure can be viewed at wileyonlinelibrary.com]

There is no relationship between calculated temperature and age in either sample.

4.9 | Mineral equilibria forward modelling

4.9.1 | WGC2019J-25B

Figure 14 represents the mineral equilibria forward model for sample WGC2019J-25B. The early prograde path for WGC2019J-25B is a conservative estimate based on Zr-in-rutile temperatures and the inferred presence of melt in the rock (Figure 14; Point 1), where crystallized melt was interpreted based on <20 μm polycrystalline inclusions inside garnet. Population 1 Zr-in-rutile temperatures occur exclusively as inclusions inside garnet, making the current garnet mode in the rock (∼13.5%) a reasonable constraint on this thermometry line. Even if garnet had experienced retrograde replacement and once existed as larger porphyroblasts, at least the current mode of garnet would have had to have existed during rutile growth in order for rutile to be captured as inclusions. Garnet mode can therefore provide a minimum constraint on population 1 Zr-in-rutile thermometry (Figure S7). Based on these constraints, WGC2019J-25B is interpreted to have traversed through the garnet+kyanite+rutile+biotite+plagioclase+hematite+quartz+melt field at between 9.5 and 11.5 kbar and ∼700°C. It should be noted that modelled hematite mode within this field is <0.01%, so would not contribute heavily to the oxidation state of the rock. Constraints for the later prograde history are poor, but the rock is assumed to have intersected population 2 Zr-in-rutile somewhere along its ∼8.5–28 kbar and 640–730°C contour (Figure 14; Point 2). The exact location along this thermometry line cannot be precisely determined, though it likely occurs at >20 kbar to avoid cooling in the prograde P–T path.

Based on existing minerals, the interpreted peak assemblage is garnet+kyanite+quartz+rutile+apatite. Additional to this, based on compositional criteria biotite-plagioclase intergrowths (Figure 3a) comprising ∼26% of the sample could conceivably represent the replacement of phengite and omphacite. UHP minerals and quartz textures after coesite have been observed in rocks proximal to the metapelite sampled in this study (e.g. Carswell et al., 2003), suggesting that the sample likely also experienced UHP conditions. Additionally, while it cannot be directly observed, we suggest the peak assemblage contained water, rather than melt. For the peak assemblage to have contained melt and coesite, temperatures > 850°C would be required, for which there is no evidence from rutile or zircon trace element thermometry. Therefore, the full peak assemblage can be interpreted as garnet+kyanite+phengite+omphacite+rutile+apatite+coesite+water (Figure 14; Point 3).

Reaction textures in WGC2019J-25B first involve the development of rock-scale plagioclase-biotite symplectites interpreted to have replaced omphacite-phengite-rutile followed by the formation of cordierite, plagioclase, and spinel after kyanite and garnet. Volumetrically, this second-stage retrograde assemblage comprises <3% of the sample, suggesting these localized Al-rich reaction domains may not have a bulk composition equivalent to the larger-scale rock composition. Therefore, retrograde conditions have been inferred by computing independent thermobarometric reactions for the cordierite+spinel+plagioclase-bearing symplectites and coronas (Appendix S2). The intersection of these equilibria lines gives a P–T point at ∼7 kbar and ∼740°C (Figure 14; Point 5). Calculations between 700 and 800°C give pressures between 6.94 and 7.4 kbar and uncertainties between 0.60 and 0.64 kbar (Appendix S2). The position of this P–T point correlates well with the modelled stability of cordierite-bearing assemblages, which plot below the kyanite-sillimanite transformation (Figure 14). The absence of spinel in the WGC2019J-25B P–T diagram reflects that it only forms in highly localized Al-rich areas of the rock, whereas the calculated pseudosection is computed for the overall rock composition (Figure 14). Additionally, spinel contains up to 2.5 wt% ZnO that may have enhanced its stability relative to the overall modelled composition (Nichols et al., 1992). Despite evidence for biotite as a reactant in the formation of the cordierite-spinel-plagioclase-bearing assemblage, there is no K-bearing product within the reaction textures, indicating potential loss of K_2O either within a fluid or the melt. Of these possibilities, melt is tentatively suggested based on the sparsely migmatitic character of the rock. The small volume of reaction texture domains suggests that any melt loss would have had negligible effect on the overall rock composition. Therefore, it is suggested the modelled solidus is a reasonable estimate for the minimum temperature at which the retrograde cordierite-bearing assemblage may have formed.

4.9.2 | WGC2019J-31A

Recently obtained Lu–Hf age data from the sample used in this study indicates the garnets in the Fjørtoft sample, WGC2019J-31A, formed during the Mesoproterozoic (Simpson et al., 2021; Tamblyn et al., 2021). This is consistent with the presence of Late Mesoproterozoic-aged monazite inclusions inside garnet (Figure 8a; Terry et al., 2000b; Holder

et al., 2015). To account for the presence of Mesoproterozoic-aged garnet in the likely Caledonian-aged matrix, garnet was subtracted from the bulk composition used in *P–T* modelling (Figure 15). A model accounting for the opposite scenario, in which garnet is solely Caledonian-aged is provided in Appendix S3 as a counterpoint reference. A Zr-in-rutile thermometry contour is plotted on the *P–T* diagram. The upper *P–T* validity of this contour is constrained by the availability of a Ti reservoir, either through biotite breakdown or the recrystallization of pre-existing rutile.

The mineral assemblage in WGC2019J-31A consists of garnet porphyroblasts enclosed in a matrix of kyanite+biotite+muscovite+plagioclase+K-feldspar+rutile +quartz+graphite+Fe-Cu sulphides. Aside from garnet and its inclusions, there are no obvious relics of minerals that pre-dated the current matrix assemblage and therefore no evidence for diagnostic minerals such as coesite or diamond, although the sample does contain graphite which conceivably postdates diamond. However, past studies from the Fjørtoft metapelite have identified UHP minerals (e.g. Dobrzhinetskaya et al., 1995; van Roermund et al., 2002), providing evidence this sample likely also experienced UHP conditions. A minimum constraint for peak conditions is therefore suggested as ~28 kbar in a field of coesite stability. If reported diamond is part of the mineral assemblage, as opposed to a sample preparation contaminant, then pressures were in excess of 38 kbar. Within the matrix, biotite and muscovite define the foliation. Biotite post-dates muscovite, suggesting the rock may have cooled through a *P–T* field defined by
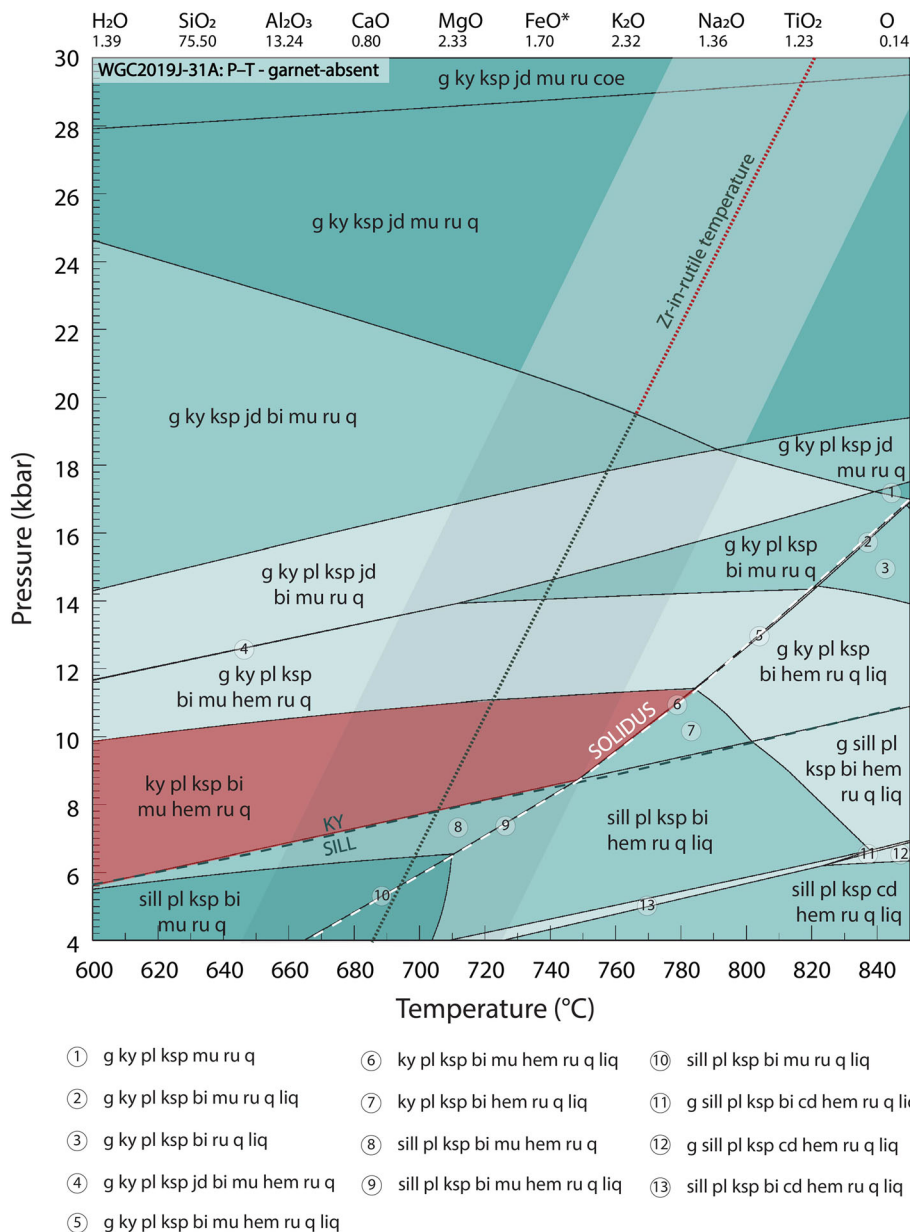

FIGURE 15 WGC2019J-31A garnet-absent *P–T* diagram. The highlighted field indicates the current mineral assemblage in the rock. Zr-in-rutile temperatures are indicated by a dotted line, with the surrounding shaded area representing associated errors. Bulk composition is listed in mol. % at the top of the diagram. Variance increases with shading. A garnet-present *P–T* diagram is given in Figure S6. Abbreviations as in Figure 14 [Colour figure can be viewed at wileyonlinelibrary.com]

kyanite+biotite+muscovite+plagioclase+K-feldspar+rutile+quartz. This assemblage is also stable across a wide range of temperatures between ∼6 and 11 kbar (Figure 15). The modelled assemblage also contains hematite, of which the modal proportion is less than 1%. Therefore, its presence in the model is interpreted as insignificant. The formation of biotite after muscovite suggests the rock cooled to form the matrix assemblage.

5 | DISCUSSION

In this study, multi-mineral U–Pb geochronology, petrochronology, thermometry, and mineral equilibria forward modelling were undertaken on (U)HP metapelitic rocks from Ulsteinvik and Fjørtoft in order to provide further insight into the conditions and dynamics of continental subduction within the WGR.

5.1 | Interpretation of U–Pb geochronology and trace elements

U–Pb geochronology of zircon, monazite, apatite, and rutile from the Ulsteinvik metapelite documents a predominantly Caledonian-aged history, with the exception of two Mesoproterozoic-aged zircon analyses (Figure 7b). This poor preservation of Mesoproterozoic dates relative to the Fjørtoft metapelite may be attributed to differing origins within or outside of the Seve-Blåhø nappe, or a number of other causes including (1) Pb-loss in metamict zircon (Halpin et al., 2012; Mezger & Krogstad, 1997), (2) Mesoproterozoic-aged zircon not being extracted during mineral separation, or (3) variable overprinting across the WGR that in places, completely obliterated Mesoproterozoic mineral assemblages. Further interpretation is limited by the sparsity of this data.

Concordant Caledonian zircon dates span from c. 469 to 367 Ma (Figure 7a,c), suggesting either a protracted period of (re)crystallization, Pb loss, or multiple discrete events, all of which may contribute to the 'smeared' appearance of data along the concordia (e.g. Halpin et al., 2012; Mezger & Krogstad, 1997). REE concentrations in zircon do not vary systematically with age, and the majority of grains exhibit relatively flat HREE profiles without Eu anomalies (Figure 8a). Rutile grains record a similarly prolonged history, with dates ranging between c. 453 and 358 Ma (Figure 13a,b). The Ordovician to Early Silurian dates recorded in zircon and rutile from this study are similar in age to the metamorphic assemblages in the Seve-Blåhø nappe in Sweden (e.g. Brueckner et al., 2004; Majka et al., 2012). This supports the hypothesis made by Root et al. (2005) regarding a potentially allochthonous history for rocks in the Ulsteinvik region. Ulsteinvik and surrounds were first correlated with the Blåhø Nappe based on lithological similarities (Root et al., 2005), and have been further linked by zircon data from a mafic eclogite in Ulsteinvik, which shows a near continuous spread of concordant zircon ages ranging from c. 475 to 430 Ma (DesOrmeau et al., 2015). The record of pre-Scandian U–Pb zircon and rutile dates from the Ulsteinvik metapelite (Figures 7a,c and 13a,b), corroborates the zircon data from DesOrmeau et al. (2015), and further validates the hypothesis made by Root et al. (2005) regarding an allochthonous origin for the rocks in the Ulsteinvik region. It also closely resembles geochronology from Gossa, which is part of the Seve-Blåhø nappe north of the Nordøyane UHP domain (Jeanneret et al., 2021). The apparent ability of rutile in sample WGC2019J-25B to record dates as old as c. 450–440 Ma without resetting is attributed to its textural location as an inclusion within garnet, where it appears to have been effectively 'armoured' to retain Pb above its nominal closure temperature (∼640°C; Kooijman et al., 2010). Old rutile ages (up to c. 450 Ma)
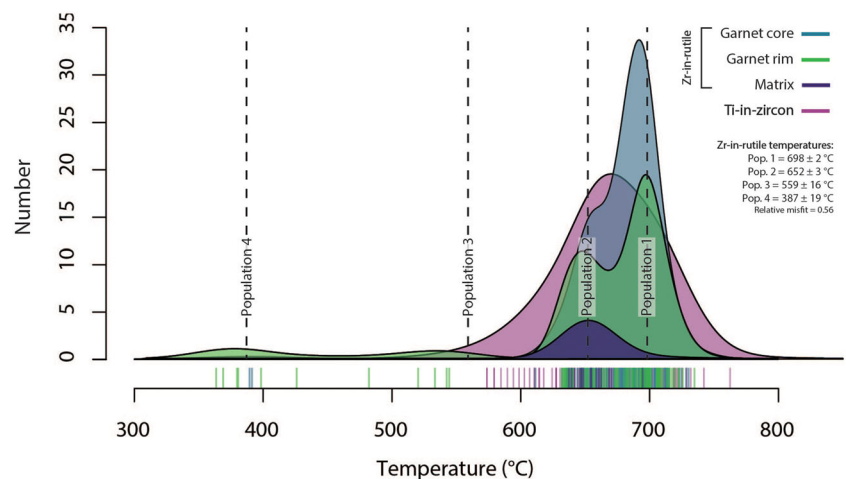

FIGURE 16 Zr-in-rutile (Kohn, 2020) and Ti-in-zircon (Ferry & Watson, 2007) temperature distributions calculated at 10 kbar. Zr-in-rutile thermometry profiles are separated by textural location. Blue = rutile in garnet core, green = rutile in garnet rim, deep purple = rutile in matrix, lilac = zircon [Colour figure can be viewed at wileyonlinelibrary.com]

can therefore be used to provide an approximate constraint for the minimum age of garnet nucleation in the Ulsteinvik metapelite, whilst younger ages record variable diffusional resetting or recrystallization. Zr-in-rutile temperatures (Figure 16), from inclusions in garnet cores range between 400 and 730°C, with nearly 90% (110/126) of those temperatures falling between 650 and 730°C using the Kohn (2020) calibration. Temperatures were calculated at 10 kbar, as this is the approximate pressure that aligns with the current modal proportion of garnet in the rock in the mineral equilibria *P–T* model. Conservatively, it therefore represents the maximum pressure at which rutile grains would have become trapped within garnet cores. At 10 kbar, rutile grains that occur in the rims of the garnet give Zr-in-rutile temperature estimates between 360 and 735°C, with ∼90% of estimates between 630 and 735°C (82/95). With the exception of a minor number of low-Zr analyses, the overall distribution of Zr-in-rutile temperatures has a bimodal character. This bimodality defines two temperature peaks: ∼695°C (population 1) and ∼650°C (population 2). Gaussian unmixing identified the bimodal thermal character in both garnet core and rim rutile temperatures, but only the lower temperature population for matrix-hosted grains (Figure 16). This overall apparent bimodality could reflect either different prograde populations captured by garnet, partial retrograde Zr loss, or recrystallization of rutile during the peak to retrograde evolution of the rock.

Zircon was analysed in a grain mount, and grains therefore lack textural context. Similarities in age range suggests rutile and zircon existed in the same mineral assemblage for an extended period of time (Figures 7a,b and 13a,b). Assuming Ti contents in Caledonian-aged zircon were buffered by rutile, as appears likely, Ti-in-zircon temperatures give an overall mean value of 742 ± 7°C for the Ferry and Watson (2007) calibration (Figure 16) and 738 ± 7°C for Watson et al. (2006), spanning an equivalent temperature range to the Zr-in-rutile thermometry.

Irrespective of age, zircon in WGC2019J-25B is characterized by flat HREE signatures, suggesting the concurrent growth of another HREE-reservoir (e.g. Rubatto, 2002). Rare earth element partitioning trends between zircon and garnet (D_{REE} = garnet/zircon) suggest garnet underwent earlier or coexisting growth relative to Caledonian zircon (Figure 17a). Garnet cores record D_{REE} values for Pr–Lu approaching 10, while garnet rims have slightly lower D_{REE} values but still exceeding 1. Based on pre-Scandian zircon dates, this suggests that garnet from WGC2019J-25B began growing prior to zircon.

In addition to early Caledonian dates, zircon and rutile from sample WGC2019J-25B preserve a pervasive record of concordant dates from *c.* 430 to 370 Ma. This range coincides with the general consensus of when subduction and subsequent exhumation of the WGR occurred. Monazite occurs in two discordant Scandian-aged populations (*c.* 402 Ma and 377 Ma; Figure 9a) and occurs either within the matrix or within kyanite and generally does not contain an Eu anomaly (Figure 11a). Apatite U–Pb discordia gives a lower intercept date of 399.9 ± 1.9 Ma (Figure 12a). Apatite within garnet lacks a distinct Eu anomaly and is characterized by flat HREE signatures, whilst matrix apatite exhibits a strongly negative Eu anomaly and comparative enrichment in HREEs (Figure 12b). Negative Eu anomalies are commonly assumed to be the product of co-crystallization with feldspar; however, they may also occur due to the sensitivity of Eu^{2+}/Eu^{3+} to low f_{O2} (Holder et al., 2020). Apatite inclusions within garnet are connected to the matrix via fractures, preventing them from being armoured in a scenario similar to that described for rutile. The geochemical differences in apatite grains of the same age can be explained by relative differences in diffusion, where REEs such as Eu are less mobile than Pb (e.g. Bau, 1991; Cherniak, 2000). We therefore suggest apatite preserved as inclusions within garnet retains a prograde REE
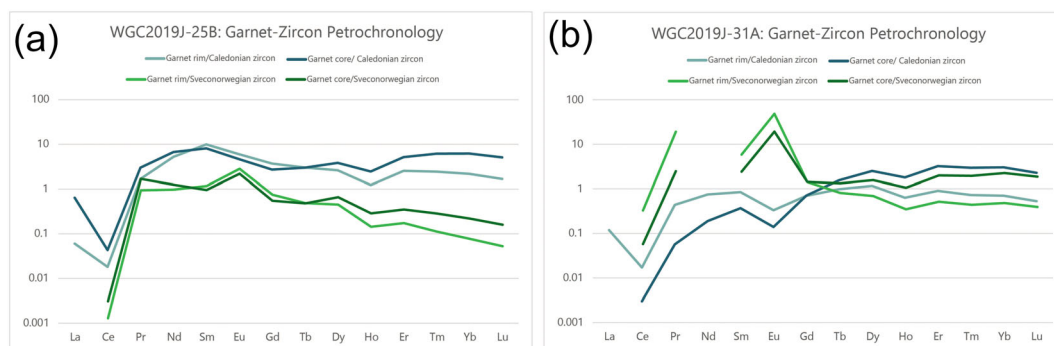

FIGURE 17 Rare earth element partitioning trends between zircon and garnet (D_{REE} = garnet/zircon) using representative rare earth element averages for Caledonian versus Mesoproterozoic zircon populations and garnet core versus garnet rim populations. (a) WGC2019J-25B. (b) WGC2019J-31A [Colour figure can be viewed at wileyonlinelibrary.com]

signature, but only records ages representative of cooling through the nominal Pb closure temperature for large 500–1000 μm grains (∼600°C; Krogstad & Walker, 1994; Cochrane et al., 2014). Apatite inclusions in garnet appear to lack an Eu anomaly, but upon closer inspection, apatite from all textural locations record Eu concentrations of approximately the same magnitude. Instead, Sm and Gd vary, with texturally younger apatite being more enriched in MREEs and depleted in HREEs relative to apatite inclusions in garnet cores. The HREE signatures in apatite within garnet cores can be attributed to the uptake of HREEs by the host garnet, while apatite in the matrix conceivably recrystallized during the breakdown of allanite, growth of monazite and potentially the breakdown of garnet. This gives the impression of a pronounced Eu anomaly in matrix apatite.

The absence of an Eu anomaly in effectively age-equivalent monazite (c. 402 Ma; Figure 9b) suggests the rock traversed from plagioclase-absent to plagioclase-bearing parts of P–T space at c. 400 Ma (Figure 14, Point 3; Nagy et al., 2002; Rubatto et al., 2013). This potentially provides a well-defined constraint for the end of UHP metamorphism and is consistent with previous studies constraining the beginning of exhumation and retrograde plagioclase crystallization at Ulsteinvik (Butler et al., 2018; Carswell et al., 2003; T.E. Krogh et al., 2011; Kylander-Clark et al., 2008; Kylander-Clark & Hacker, 2014; Root et al., 2004, 2005; Schärer & Labrousse, 2003; Spencer et al., 2013; Tucker et al., 2004; Young et al., 2007). As discussed by Holder et al. (2015, 2020), it should be noted the absence or presence of an Eu anomaly in monazite may also be tied to oxygen fugacity and its impact on the compatibility of Sr and Eu in monazite at high temperatures (Aigner-Torres et al., 2007; Wilke & Behrens, 1999). Therefore, it is plausible the absence of a negative Eu anomaly in monazite may reflect more oxidized conditions. However, a c. 400 Ma monazite age is consistent with past interpretations for the onset of exhumation (Butler et al., 2018; Carswell et al., 2003; T.E. Krogh et al., 2011; Kylander-Clark et al., 2008; Kylander-Clark & Hacker, 2014; Root et al., 2004, 2005; Schärer & Labrousse, 2003; Spencer et al., 2013; Tucker et al., 2004; Vrijmoed et al., 2013; Walsh et al., 2013; Young et al., 2007). A second population of c. 377 Ma monazite is assumed to have formed as a result of recrystallization of c. 402 Ma monazite.

Recent advances in Lu–Hf dating allowed for garnets from the same sample as the Fjørtoft metapelite used in this study (WGC2019J-31A) to be dated in situ. Mesoproterozoic garnet ages (Simpson et al., 2021; Tamblyn et al., 2021) indicate the Fjørtoft metapelite sample used in this study had a Mesoproterozoic-aged metamorphic protolith. These findings are corroborated by U–Pb results from monazite and zircon, which record unambiguous evidence of a Mesoproterozoic event (e.g. Bingen et al., 2008). Zircon gives a small number of concordant upper intercept dates (3.6% of total concordant analyses), ranging from 1143 to 903 Ma (Figure 7g), while monazite retains a more extensive record with 51 concordant analyses (64% of total concordant), giving an age of 1053.2 ± 3.6 Ma (Figures 9c and 10b). Mesoproterozoic-aged monazite occurs predominantly in the interior of garnet (Figure 10a), inside the internal boundary defined by fine-grained inclusion trails (Figure 3g,h). Monazite grains in garnet rims and in the matrix define a bimodal distribution, comprising the c. 1053 Ma population and a second 423.2 ± 2.0 Ma population. The monazite age bimodality and its textural relationship to garnet is epitomized in a ∼700 μm monazite grain, where one side is exposed to the matrix and the other included inside garnet (Figure 10a, inset). Spot dates on the garnet side are Mesoproterozoic-aged, while analysis spots on the matrix-side record Caledonian dates. Past records of Mesoproterozoic-aged monazite from the Fjørtoft metapelite have been broadly interpreted as detrital, despite their ubiquity and/or regular textural association within garnet (Cuthbert & van Roermund, 2011; Holder et al., 2015; Liu & Massone, 2019; Terry et al., 2000b; Walczak et al., 2019). Instead, we suggest the consistent occurrence of c. 1050 Ma monazite in garnet (Figure 10a), and similar-aged Lu–Hf garnet dates provide strong evidence the Fjørtoft metapelite experienced high-grade, late Mesoproterozic-aged metamorphism. Reinforcing this, garnet-zircon petrochronology in this study shows garnet core growth pre-dated the (re)crystallization of both Mesoproterozoic and Caledonian-aged zircon (Figure 17b). A similar record of Mesoproterozoic-aged growth has been found elsewhere in the WGR using various minerals and methods (e.g. Butler et al., 2018; DesOrmeau et al., 2015; Hacker et al., 2015; Holder et al., 2015; Root et al., 2005; Tamblyn et al., 2021; Walsh et al., 2007). However, this record of late Mesoproterozoic metamorphism is generally regionally absent (Butler, 2013; Carswell et al., 2003, 2006; Cuthbert et al., 2000; Hacker et al., 2010; Holder et al., 2015; Kylander-Clark et al., 2009; Root et al., 2004; Wain, 1997; Young et al., 2007). Even at the sampled Fjortoft metapelite location and its nearby continuity, garnet Lu–Hf ages record different metamorphic histories. Tamblyn et al. (2021) analysed four different Fjørtoft samples using garnet Lu–Hf, three of which gave late Mesoproterozoic ages, with no Caledonian record. The fourth sample, however, gave a poorly resolved Caledonian age of 496 ± 73 Ma and preserved no Mesoproterozoic record, despite being collected only metres away from sample

WGC2019J-31A and lacking any obvious lithological or textural differences. Similarly, Tual et al. (2020) obtained a Lu–Hf garnet age of 422 ± 2 Ma from the Fjørtoft metapelite. In contrast, the Ulsteinvik metapelite from this study only records two Mesoproterozoic-aged zircons and garnet Lu–Hf dating gives Caledonian ages (Tamblyn et al., 2021). This regional and local heterogeneity in the recorded timing of garnet formation highlights complexity in the metamorphic record, possibly arising as the result of either high-grade Caledonian-aged overprinting of local previously retrogressed Mesoproterozoic-aged assemblages, the resistance of low aH2O assemblages to Caledonian metamorphic change, or the incorporation of previously unmetamorphosed rocks into the Caledonian tectonic system.

Three potential discordia paths are proposed for Fjørtoft metapelitic zircon (Figure 7d), two of which track from discordant Mesoproterozoic-aged grains to either concordant Mesoproterozoic-aged or Caledonian-aged grains, and the third of which spans from the Mesoproterozoic to the Caledonian. The latter discordia comprises the most analyses but contributes ambiguity in defining the age range of Caledonian zircon grains. Due to its proximity to the concordia, a large majority of ellipses defining the discordia are also in contact with the concordia. In order to identify genuine Caledonian-aged zircons, an obvious geochemical difference would have to be identified between analyses. Older zircon analyses typically exhibit overall lower REE concentrations and stronger negative Eu anomalies relative to the younger dates (Figure 8b); however, this transition is broadly gradational and is not consistent enough to act as an accurate method of differentiation. Additionally, Caledonian-aged zircon may have formed as the result of the recrystallization of Mesoproterozoic-aged zircon, which likely grew in the presence of garnet (Figure 17). Caledonian-aged zircon may therefore have inherited REE signatures from a Mesoproterozoic-aged assemblage. The inferred microdiamond-bearing garnet-kyanite metapelites from Fjørtoft have been suggested to represent part of the Seve-Blåhø nappe (Terry & Robinson, 2004; Terry et al., 2000b), though it is worth noting the metapelite also bears geochronological similarity to the Tännäs Augen Gneiss Nappe in the Middle Allochthon in the Swedish Caledonides (Claesson, 1980; Dallmeyer et al., 1985; Dallmeyer & Gee, 1986; Gromet et al., 1993; Mørk et al., 1988; Romer, 1994; Sjöström & Bergman, 1994). To summarize, peak metamorphism in the nappe likely occurred at c. 440–435 Ma, prior to thrusting of the Upper Allochthon over the Middle Allochthon (Gromet et al., 1993; Romer, 1994; Sjöström & Bergman, 1994). The SNC outcrops both in Sweden and in the Indre Troms region and WGR in Norway. In northern parts of the SNC, dating indicates two generations of pre-Scandian metamorphism at c. 500–475 Ma and c. 460–440 Ma (e.g. Brueckner & van Roermund, 2007; Dallmeyer & Gee, 1986; Root & Corfu, 2009, 2012). Ages become progressively younger further south in the Seve Nappe. In the WGR, monazite dates span c. 500–385 Ma, supported by zircon geochronology (Walsh et al., 2007), and dates as old as c. 450 Ma occur at Fjortoft (Walczak et al., 2019). Differentiating between an origin in the Tännäs Augen Gneiss Nappe as opposed to the basement of the Seve-Blåhø nappe is difficult. Based on previous work, we assign c. 505 Ma to be the oldest, feasible age that could be recorded by Fjørtoft metamorphic zircon, but acknowledge this upper constraint is uncertain. Determining whether the Fjørtoft metapelite originated in the basement of the Seve-Blåhø Nappe or within the Tännäs Augen Gneiss Nappe is outside of the scope of this study, as a result we conservatively present data under the current assumption that it was subducted with the Seve-Blåhø Nappe.

Concordant rutile dates range from c. 449 to 378 Ma (Figure 13c,d), while Caledonian-aged monazite records dates between c. 438 and 382 Ma (89% > 415 Ma; Figure 9b,d). The Late Ordovician–Early Silurian components of this history are attributed to the imbrication and emplacement of the Seve-Blåhø Nappe, a sliver of which likely exists on Fjørtoft (e.g. Terry et al., 2000a). Caledonian-aged monazite U–Pb results are split into two populations: 423.2 ± 2.0 Ma and 385.2 ± 6.7 Ma (Figure 9b,d). The older and more abundant population occurs as inclusions within garnet rims and in the matrix, while the younger population occurs solely within matrix. Despite c. 423 Ma monazites occurring within the Mesoproterozoic-aged garnet (Simpson et al., 2021; Tamblyn et al., 2021), these grains are connected to the matrix via fractures. This connection with the matrix may have facilitated monazite recrystallization in response to fracture-hosted fluid migration (e.g. Tartakovsky et al., 2007; Figure 10a). Both monazite populations exhibit negative Eu anomalies, which could be interpreted as the product of coeval growth with plagioclase and therefore early exhumation of Fjørtoft. However, variables such as f_{O2} (Holder et al., 2020) and monazite composition also may impact Eu anomaly magnitude. Ca-bearing monazite is able to accommodate Eu^{2+} in addition to Eu^{3+}, effectively suppressing the magnitude of the Eu anomaly. Monazite in the Fjørtoft metapelite (WGC2019J-31A) is Ca-poor (<∼5000 ppm) and therefore has limited ability to uptake Eu^{2+}. In the reduced, graphite-bearing assemblage of the Fjørtoft metapelite, the Eu^{3+}/Eu^{2+} ratio would be low and Ca-poor monazite could therefore develop a negative anomaly without cogenetic plagioclase. Negative Eu anomalies

in Fjørtoft monazite are therefore an unreliable indicator for stable plagioclase. Instead, population 2 monazite (*c.* 423 Ma) is interpreted as recording the early stages of (U) HP metamorphism (Holder et al., 2015), while population 3 monazite (*c.* 385 Ma) is consistent with past constraints for cooling in the region (e.g. T.E. Krogh et al., 2011; Kylander-Clark & Hacker, 2014; Vrijmoed et al., 2013; Walsh et al., 2013).

5.2 | Pressure–temperature conditions during metamorphism

P–T conditions were calculated from mineral equilibria forward modelling and Zr-in-rutile thermometry in the Ulsteinvik metapelite (Figure 14). Two populations of Zr-in-rutile temperatures are plotted on the WGC2019J-25B *P–T* diagram (Figure 14). Population 1 (698 ± 2°C) occurs almost exclusively as inclusions within garnet and is interpreted to preserve a high temperature record, possibly associated with the arc–continent collision that pre-dates the main phase of subduction. Due to its textural association with garnet, the upper pressure constraint for population 1 Zr-in-rutile is determined by the current garnet mode in the rock (~13.5%), as this amount of garnet would have needed to exist in the assemblage in order for rutile to be captured. This defines an ~9–11.5 kbar pressure range for population 1 Zr-in-rutile, intersecting with the garnet+kyanite+rutile+biotite +plagioclase+hematite+quartz+melt field (Figure 14; Point 1), which is supported by the interpreted presence of crystallized melt inclusions inside garnet (Figure 4). *P–T* modelling shows garnet growth pre-dates rutile growth in the rock (Figure S7), and garnet-zircon petro-chronology demonstrates garnet growth either pre-dates or coincides with the crystallization of Caledonian zircon (Figure 17a). To explain how garnet initiation can pre-date the growth of its inclusion minerals, we suggest early garnet grew as a fine-grained mineral, and garnet nuclei then coalesced to entrap rutile that formed slightly later at the edges of the proto-garnets (e.g. Daniel & Spear, 1999; Majka et al., 2018; Spiess et al., 2008; Whitney & Seaton, 2010). This also explains why garnet, which is modelled to grow throughout the *P–T* history (Figure S7), is capable of entrapping high-temperature inclusions even in cores. Population 2 Zr-in-rutile temperatures (~640–745°C) are either the result of subsequent rutile growth on the prograde path, recrystallization of rutile or diffusive loss of Zr. Regardless, the Ulsteinvik metapelite would have intersected this thermometry contour at some point in its *P–T* history (Figure 14; Point 2), although the corresponding pressure cannot be precisely determined.

The inferred peak assemblage for the Ulsteinvik metapelite is garnet+kyanite+coesite+rutile+phengite +omphacite+water. Water is suggested rather than melt, due to coesite and melt only coexisting at temperatures exceeding *c.* 850°C. Zircon and rutile thermometry preclude ultrahigh-temperature conditions. Neither omphacite nor coesite occur in the rock, but are inferred based on relict symplectites (Appendix S1) and the presence of coesite in the neighbouring Hareidland eclogite (Carswell et al., 2003), respectively. This provides a minimum peak pressure constraint of ~28 kbar (Figure 14; Point 3).

Assuming no dramatic change in oxidation fugacity, the absence of a Eu anomaly in *c.* 402 Ma Ulsteinvik monazite (Figure 9b,d; Figure 11a) and its presence in age-equivalent *c.* 400 Ma apatite (Figure 12a,b; McLennan, 1989) adds a time constraint to the Ulsteinvik *P–T* path, suggesting the rock did not traverse through retrograde plagioclase-stable fields until after *c.* 400 Ma. Based upon this hypothesis, Ulsteinvik must have experienced either a long-lived prograde path and/or stalled in the mantle before its retrograde evolution, remaining at *P–T* conditions above 15 kbar (Figure 14; Point 4) until at least *c.* 400 Ma. Temperature constraints cannot be determined for this phase of the metapelite's history. Three distinct retrograde mineral reaction textures occur: (1) fine-grained intergrown biotite+plagioclase+quartz domains (Figure 3a); (2) fine-grained cordierite+plagioclase+spinel symplectitic coronas and coronitic plagioclase (Figure 3b,c,e); and (3) partial replacement of kyanite by sillimanite (Figure 3d). As discussed above, biotite-plagioclase-quartz intergrowths are interpreted as the retrograde product of peak omphacite+phengite +rutile breakdown. Cordierite+plagioclase+spinel coronas are interpreted to form at the expense of garnet +kyanite+biotite, which still exist in the rock. Symplectites around kyanite reflect the instability of kyanite with the matrix and have been suggested to form as a result of near-isothermal decompression to <10 kbar (Baldwin et al., 2015; Štípská et al., 2010). Allied to these retrograde textures, calculation of a single *P–T* point (Appendix S2) was used to constrain retrograde conditions within the Ulsteinvik metapelite at ~7 kbar and ~740°C (Figure 14, Point 5; Appendix S2), at which point the rock contains both cordierite and sillimanite. This supports the petrographic observation of cordierite+spinel+plagioclase coronas occasionally consuming retrograde sillimanite (Figure 3d). Decompression during exhumation may have caused minor melting within the rock (Figure 2c). The lack of K-feldspar within cordierite-spinel reaction textures suggests some melt loss, however this is likely to be volumetrically minor due to the preservation of abundant biotite, the small volume (<3%) of

cordierite and spinel in the rock, and the lack of a pervasive migmatitic character in the outcrop.

Based on the frequent observation of Mesoproterozoic-aged monazite and zircon inclusions inside garnet from Fjørtoft both in our study (Figure 10a) and in others (e.g. Cuthbert & van Roermund, 2011; Liu & Massone, 2019; Terry et al., 2000a; Walczak et al., 2019), and Mesoproterozoic Lu–Hf dates from garnet (Simpson et al., 2021; Tamblyn et al., 2021), we confidently state that garnet growth in our sample from Fjørtoft pre-dates the Caledonian Orogeny. To account for this, garnet was excluded from the Fjørtoft bulk composition used in P–T modelling. Limited P–T constraints exist in the Fjørtoft mineral equilibria forward model (Figure 15), preventing extensive interpretation. The current Fjørtoft assemblage is composed of Mesoproterozoic-aged garnet porphyroblasts in a matrix of kyanite+biotite+muscovite+plagioclase+K-feldspar +rutile+quartz+graphite+Fe-Cu sulphides. Aside from garnet, no relics of an earlier mineral assemblage are preserved, and the rock does not contain diagnostic UHP microdiamond or coesite relics. However, past studies have stated the presence of microdiamond at this locality and nearby (Dobrzhinetskaya et al., 1995; van Roermund et al., 2002). The inferred peak assemblage is therefore assumed to have contained coesite, providing a minimum peak constraint at ∼28 kbar, with diamond indicating pressures >38 kbar. The matrix assemblage occurs in a large field, spanning from 600 to 780°C and 6–11 kbar, potentially limited by Zr-in-rutile thermometry to 660–760°C. The observation of biotite post-dating muscovite suggests this assemblage forming via cooling.

Liu and Massone (2019) followed a similar approach to one adopted in this study in their P–T modelling of the Fjørtoft metapelite, calculating one model for the entire bulk rock composition, and a second model in which garnet cores were subtracted. However, they interpreted that garnet cores formed during the pre-Scandian stage of the Caledonian, and that the rims and finer-grained garnets recorded Scandian subduction. Their P–T results were significantly lower than past UHP estimates (core = 1.2– 1.3 GPa, 875–880°C; rim 1 = 1.35–1.45 GPa, 770–820°C; rim 2 = 0.74–0.90 GPa, 610–685°C; Liu & Massone, 2019). Similar results for the Fjørtoft metapelite were obtained using elastic geobarometry applied to garnet inclusions (Gilio et al., 2021). We suggest the garnets in both studies may have been at least partial relics of a Mesoproterozoic metamorphism, rather than purely recording Caledonian metamorphism. Given the potential for texturally non-obvious polymetamorphism, future thermobarometry analysis within the WGR should employ reconnaissance dating of garnet—or potentially fully armoured monazite, if present—prior to constraining P–T conditions.

5.3 | Tectonic implications for the Caledonian evolution of the Western Gneiss Region

Ulsteinvik and Fjørtoft metapelite record protracted histories. Both samples contain Mesoproterozoic U–Pb zircon and monazite ages, although Fjørtoft preserves a more extensive record. The abundance of Mesoproterozoic ages in Fjørtoft records the growth of monazite and garnet during a late Mesoproterozoic metamorphic event, at c. 1100–900 Ma.

Fjørtoft and Ulsteinvik both record a Late Ordovician-Early Silurian peak in zircon and rutile dates (Figure 18), that pre-dates the onset of the main Scandian phase of subduction in the WGR (c. 430 Ma; e.g. Griffin & Brueckner, 1980; Tucker et al., 2004; T.E. Krogh et al., 2011). In Fjørtoft, the record of these ages is widely acknowledged and attributed to its likely history as a constituent of the Seve-Blåhø nappe, which is an orogen-scale allochthonous unit that was imbricated onto the Baltican margin prior to Scandian subduction (e.g. Carswell et al., 2006; Robinson, 1995; Terry et al., 2000a). U–Pb zircon results record a long-lived pre-Scandian history, potentially spanning from c. 504 to 430 Ma. The covariance of pre-Scandian Ulsteinvik and Fjørtoft age data (Figure 18) suggests the Ulsteinvik metapelite may have also been a constituent of the Seve-Blåhø Nappe, and therefore shared its pre-Scandian history with the Fjørtoft metapelite. This hypothesis is supported by observations made by Root et al. (2005), regarding similarities in host-rock lithologies between the Ulsteinvik area and the Blåhø Nappe, as well as by near identical zircon age data presented by DesOrmeau et al. (2015) in neighbouring eclogitic rocks to the Ulsteinvik metapelite. Ulsteinvik and Fjørtoft are therefore hypothesized to have shared an early history within the Seve-Blåhø nappe, where their initial formation and imbrication was associated with arc–continent collision and subduction to mantle depths at c. 455 Ma (Majka et al., 2012). High temperatures recorded by Zr-in-rutile thermometry (698 ± 2°C; Table 3) and melt inclusions inside garnet (Figure 4) from Ulsteinvik are thought to be linked to this arc–continent collision in the WGR.

Based on geochronology, along with geochemistry and P–T modelling, the Ulsteinvik metapelite appears to have experienced a long-lived prograde Caledonian history. The preservation of prograde garnet zoning profiles (Figure 5b) indicates the Ulsteinvik metapelite could not
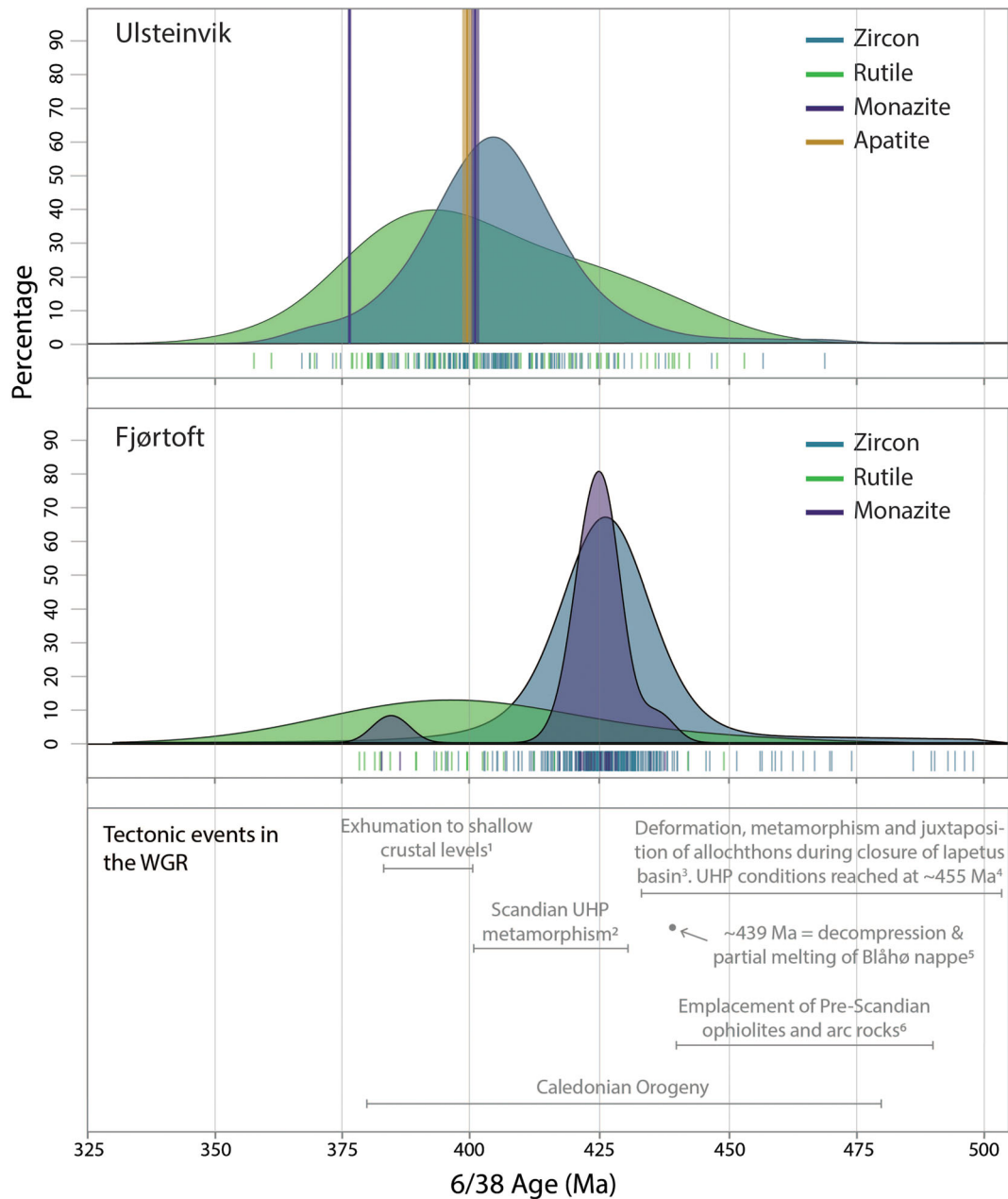
FIGURE 18 Age distribution for Ulsteinvik (green) and Fjørtoft (blue). Rutile and zircon age data are combined in cumulative age distribution curves, monazite and apatite are indicated by dotted lines and associated error bars. Note that distribution curve heights have been normalized for visual comparison. The plot is annotated based on observations and interpretations made within this study. The bottom panel presents inferred tectonic events that occur within the WGR based on past studies [Colour figure can be viewed at wileyonlinelibrary. com]

have remained in the mantle for longer than ∼10 Myr (Caddick et al., 2010). The absence of an Eu anomaly in c. 402 Ma monazite (Figure 9a) and its pronounced presence in c. 400 Ma apatite is interpreted as a rapid transition from plagioclase-absent to plagioclase-bearing P–T

space. This suggests the Ulsteinvik metapelite remained above ∼15 kbar until c. 400 Ma (Figure 14; Point 3) and is supported by various past works (e.g. Butler et al., 2018; Carswell et al., 2003; T.E. Krogh et al., 2011; Kylander-Clark et al., 2008; Kylander-Clark &

Hacker, 2014; Root et al., 2004, 2005; Schärer & Labrousse, 2003; Spencer et al., 2013; Tucker et al., 2004; Vrijmoed et al., 2013; Walsh et al., 2013; Young et al., 2007).

The relative offset in zircon, rutile, and monazite ages between the Ulsteinvik and Fjørtoft metapelites (Figure 18) may suggest a diachronous Caledonian history for the allochthons. This is potentially supported by the preservation of garnet zoning in Ulsteinvik and comparative thermal relaxation of Fjørtoft garnet profiles (Figure 5), provided this diffusion occurred during the Caledonian. The diachronicity of these histories could be interpreted as either, (1) the Blåho Nappe was disassembled at some stage during pre-Scandian subduction and exhumation, effectively disrupting an obvious connection between the Ulsteinvik and Fjørtoft metapelites, or (2) the Ulsteinvik and Fjørtoft metapelites comprised two distinct nappe complexes, with Ulsteinvik being a constituent of the Seve-Blåho Nappe alongside the geochronologically similar Gossa region (Jeanneret et al., 2021), and Fjørtoft belonging to a separate nappe complex—of which the Tännäs Augen Gneiss Nappe is tentatively suggested. In the first scenario, the Seve-Blåhø Nappe experienced slab tear and partial underplating during pre-Scandian continental underthrusting (e.g. Platt, 1993; Rosenbaum et al., 2008; van Hunen & Allen, 2011). Discrete pieces of the nappe could then reattach to the lower plate and undergo partial exhumation at different times (e.g. Berger et al., 2012).

6 | CONCLUSION

The Western Gneiss Region, Norway offers fascinating insight into the dynamics of continental subduction and emphasises that it is not always a smooth, 'conveyor belt' process. Geochronology, geochemistry, and thermometry, along with P–T forward modelling from the Ulsteinvik and Fjørtoft metapelites supports the following conclusions:

1. Pervasive Mesoproterozoic-ages of 1064–903 Ma were recorded in Fjørtoft, and a comparatively scarce record of 1018–998 Ma in Ulsteinvik. The prevalence of this record across the WGR, along with the frequent occurrence of Mesoproterozoic-aged monazite entrapped within garnet supports the conclusion that at least one generation of garnet nucleated and grew during the Mesoproterozoic. This refutes past claims of a detrital origin for Mesoproterozoic-aged monazite data. The relative preservation of these Mesoproterozoic dates across the WGR is attributed to variable degrees of deformation, retrogression and fluid access, resulting in different locations being more or less predisposed to age resetting.

2. The Ulsteinvik metapelite records a Late Ordovician-Early Silurian age peak that pre-dates the onset of Scandian UHP subduction. The similarity of this pre-Scandian age peak to ages recorded within the Seve-Blåhø nappe supports the conclusion made by Root et al. (2005) regarding Ulsteinvik's affinity for the allochthon. Fjørtoft is suggested to have either shared this Ordovician-Early Silurian history alongside Ulsteinvik in the Seve-Blåhø nappe, or to have once existed within a separate nappe complex. The Tännäs Augen Gneiss Nappe is tentatively suggested. The Ulsteinvik metapelite was exhumed prior to the Fjørtoft metapelite either through slab tear or within a separate allochthonous nappe, resulting in a diachronous history for the metapelites.

3. Ulsteinvik experienced a long-lived prograde history and potentially rapid growth of retrograde plagioclase based on the lack of negative Eu anomaly in c. 402 Ma monazite, and its presence in c. 400 Ma apatite. This suggests that Ulsteinvik was at pressures (∼16 kbar) that inhibited plagioclase growth until as late as c. 402 Ma before rapid exhumation.

ORCID

Samantha March https://orcid.org/0000-0002-5909-1280

Martin Hand https://orcid.org/0000-0003-3743-9706

Renée Tamblyn https://orcid.org/0000-0003-1679-1954
Bruna B. Carvalho https://orcid.org/0000-0003-2976-3194
Chris Clark https://orcid.org/0000-0001-9982-7849

REFERENCES

Åhäll, K., & Connelly, J. N. (2008). Long-term convergence along SW Fennoscandia: 330 m.y. of Proterozoic crustal growth. *Precambrian Research*, *161*(3–4), 452–474. https://doi.org/10.1016/j.precamres.2007.09.007

Aigner-Torres, M., Blundy, J., Ulmer, P., & Pettke, T. (2007). Laser Ablation ICPMS study of trace element partitioning between plagioclase and basaltic melts: an experimental approach. *Contributions to Mineralogy and Petrology*, *153*, 647–667.

Andersen, T. B., Berry, H. N., Lux, D. R., & Andresen, A. (1998). The tectonic significance of pre-Scandian 40Ar/39Ar phengite cooling ages in the Caledonides of western Norway. *Journal of the Geological Society, London*, *155*, 297–309. https://doi.org/10.1144/gsjgs.155.2.0297

Andersen, T. B., Jamtveit, B., Dewey, J. F., & Swensson, E. (1991). Subduction and eduction of continental crust: major mechanisms during continent–continent collision and orogenic extensional collapse, a model based on the south Norwegian Caledonides. *Terra Nova*, *3*, 303–310.

Armstrong, J. T. (1988). *Quantitative analysis of silicate and oxide minerals: Comparison of Monte Carlo, ZAF, and φ (ρz) procedures*. San Francisco Press.

Austrheim, H. (1987). Eclogitization of lower crustal granulites by fluid migration through shear zones. *Earth and Planetary Science Letters*, *81*, 221–232.

Baldwin, J. A., Powell, R., White, R. W., & Štípská, P. (2015). Using calculated chemical potential relationships to account for-replacement of kyanite by symplectite in high pressure granulites. *Journal of Metamorphic Geology*, *33*, 311–330. https://doi.org/10.1111/jmg.12122

Barnes, C. J., Majka, J., Jeanneret, P., Ziemniak, G., Kooijman, E., Kośmińska, K., Kielman-Schmitt, M., & Schneider, D. A. (2021). Using Th-U-Pb geochronology to extract crystallization ages of Paleozoic metamorphic monazite contaminated by initial Pb. *Chemical Geology*, *582*, 120450. https://doi.org/10.1016/j.chemgeo.2021.120450

Barnes, C. J., Majka, J., Schneider, D., Walczak, K., Bukała, M., Kośmińska, K., Tokarski, T., & Karlsson, A. (2019). High-spatial resolution dating of monazite and zircon reveals the timing of subduction–exhumation of the Vaimok Lens in the Seve Nappe Complex (Scandinavian Caledonides). *Contributions to Mineralogy and Petrology*, *174*(5). https://doi.org/10.1007/s00410-018-1539-1

Bartoli, O., Acosta-Vigil, A., Ferrero, S., & Cesare, B. (2016). Granitoid magmas preserved as melt inclusions in high-grade metamorphic rock. *American Mineralogist*, *101*(7), 1543–1559.

Batt, G. E., & Braun, J. (1999). The tectonic evolution of the Southern Alps, New Zealand: Insights from fully thermally coupled dynamical modelling. *Geophysical Journal International*, *136*(2), 403–420. https://doi.org/10.1046/j.1365-246X.1999.00730.x

Bau, M. (1991). Rare-earth mobility during hydrothermal and metamorphic fluid-rock interaction and the significance of the oxidation state of europium. *Chemical Geology*, *93*, 219–230. https://doi.org/10.1016/0009-2541(91)90115-8

Beckman, V., Möller, C., Söderlund, U., Corfu, F., Pallon, J., & Chamberlain, K. R. (2014). Metamorphic zircon formation at the transition from gabbro to eclogite in Trollheimen–Surnadalen, Norwegian Caledonides. In F. Corfu, D. Gasser, & D. M. Chew (Eds.), *New perspecties on the Caledonides of Scandinavia and related areas* (Vol. 390, pp. 403–424). Geological Society of London Special Publications.

Berger, A., Mercolli, I., Kapferer, N., & Fügenschuh, B. (2012). Single and double exhumation of fault blocks in the internal Sesia-Lanzo Zone and the Ivrea-Verbano Zone (Biella, Italy). *International Journal of Earth Sciences*, *101*, 1877–1894. https://doi.org/10.1007/s00531-012-0755-6

Bingen, B., Nordgulen, Ø., & Viola, G. (2008). A four-phase model for the Sveconorwegian orogeny, SW Scandinavia. *Norwegian Journal of Geology*, *88*, 43–72.

Bottrill, A. D., van Hunen, J., Cuthbert, S. J., Brueckner, H. K., & Allen, M. B. (2014). Plate rotation during continental collision and its relationship with the exhumation of UHP metamorphic terranes: Application to the Norwegian Caledonides. *Geochemistry, Geophysics, Geosystems*, *15*(5), 1766–1782. https://doi.org/10.1002/2014GC005253

Brown, M., & Johnson, T. (2018). Secular change in metamorphism and the onset of global plate tectonics. *American Mineralogist*, *103*(2), 181–196. https://doi.org/10.2138/am-2018-6166

Brueckner, H. K. (1972). Interpretation of Rb-Sr Ages from the Precambrian and Paleozoic rocks of Southern Norway. *American Journal of Science*, *272*, 334–358.

Brueckner, H. K. (2006). Dunk, dunkless and re-dunk tectonics: a model for metamorphism, lack of metamorphism, and repeated metamorphism of HP/UHP terranes. *International Geology Review*, *48*, 978–995.

Brueckner, H. K., & van Roermund, H. L. M. (2004). Dunk tectonics: A multiple subduction/eduction model for the evolution of the Scandinavian Caledonides. *Tectonics*, *23*(2). https://doi.org/10.1029/2003TC001502

Brueckner, H. K., & van Roermund, H. L. M. (2007). Concurrent HP metamorphism on both margins of Iapetus: Ordovician ages for eclogites and garnet pyroxenites from the Seve Nappe Complex, Swedish Caledonides. *Journal of the Geological Society, London*, *164*, 117–128. https://doi.org/10.1144/0016-76492005-139

Brueckner, H. K., van Roermund, H. L. M., & Pearson, N. J. (2004). An Archean(?) to Paleozoic evolution for a garnet peridotite lens with sub-Baltic Shield affinity within the Seve Nappe Complex of Jämtland, Sweden, Central Scandinavian Caledonides. *Journal of Petrology*, *45*, 415–437. https://doi.org/10.1093/petrology/egg088

Bryhni, I. (1966). Reconnaissance studies of gneisses, ultrabasites, eclogites and anorthosites in outer Nordfjord, western Norway. *Norges Geologiske Undersøkelse Bulletin*, NGU (Vol. 241).

Bryhni, I., & Andréasson, P. G. (1985). Metamorphism in the Scandinavian Caledonides. In D. G. Gee & B. A. Sturt (Eds.), *The Caledonide Orogen - Scandinavia and Related Areas* (pp. 763–781). John Wiley and Sons.

Butler, J. P. (2013). *Crustal subduction and the exhumation of (ultra) high-pressure terranes: Constrasting modes with examples from*

the Alps ad Caledonides [Unpublished PhD thesis. Dalhousie University. 291 pp

Butler, J. P., Jamieson, R. A., Dunning, G. R., Pecha, M. E., Robinson, P., & Steenkamp, H. M. (2018). Timing of metamorphism and exhumation in the Nordøyane ultra-high-pressure domain, Western Gneiss Region, Norway: New constraints from complementary CA-ID-TIMS and LA-ICP-MS geochronology. *Lithos*, *310-311*, 153–170. https://doi.org/10.1016/j.lithos.2018.04.006

Butler, J. P., Jamieson, R. A., Steenkamp, H. M., & Robinson, P. (2012). Discovery of coesite–eclogite from the Nordøyane UHP domain, Western Gneiss Region, Norway: field relations, metamorphic history, and tectonic significance. *Journal of Metamorphic Geology*, *31*, 147–163. https://doi.org/10.1111/jmg.12004

Caddick, M. J., Konopásek, J., & Thompson, J. (2010). Preservation of garnet growth zoning and the duration of prograde metamorphism. *Journal of Petrology*, *51*(11), 2327–2347. https://doi.org/10.1093/petrology/egq059

Carmichael, D. M. (1969). On the mechanism of prograde metamorphic reactions in quartz-bearing pelitic rocks. *Contributions to Mineralogy and Petrology*, *20*, 244–267.

Carswell, D. A., & Cuthbert, S. J. (2003). Ultrahigh pressure metamorphism in the Western Gneiss Region of Norway. *International Geology Review*, *11*, 955–966.

Carswell, D. A., Tucker, R. D., O'Brien, P. J., & Krogh, T. E. (2003). Coesite micro-inclusions and the U/Pb age of zircons from the Hareidland Eclogite in the Western Region of Norway. *Lithos*, *67*(3–4), 181–190. https://doi.org/10.1016/S0024-4937(03)00014-8

Carswell, D. A., van Roermund, H. L. M., & Wiggers De Vries, D. F. (2006). Scandian ultrahigh-pressure metamorphism of Proterozoic basement rocks on Fjørtoft and Otrøy, Western Gneiss Region, Norway. *International Geology Review*, *48*(11), 957–977. https://doi.org/10.2747/0020-6814.48.11.957

Cesare, B., Acosta-Vigil, A., Bartoli, O., & Ferrero, S. (2015). What can we learn from melt inclusions in migmatites and granulites? *Lithos*, *239*, 186–216. https://doi.org/10.1016/j.lithos.2015.09.028

Cherniak, D. J. (2000). Rare earth element diffusion in apatite. *Geochimica et Cosmochimica Acta*, *64*, 3871–3885. https://doi.org/10.1016/S0016-7037(00)00467-1

Chopin, C. (1984). Coesite and pure pyrope in high-grade blueschists of the Western Alps: A first record and some consequences. *Contributions to Mineralogy and Petrology*, *86*(2), 107–118. https://doi.org/10.1007/BF00381838

Claesson, S. (1980). A Rb-Sr isotope study of granitoids and related mylonites in the Tännäs Augen Gneiss Nappe, southern Swedish Caledonides. *Geologiska Föreningens i Stockholm Förhandlingar*, *102*, 403–420. https://doi.org/10.1080/11035898009454497

Claesson, S., Klingspor, I., & Stephens, M. B. (1983). U-Pb and Rb-Sr isotopic data on an Ordovician volcanic-subvolcanic complex from the Tjopasi Group, Koli Nappes, Swedish Caledonides. *Geologiska Föreningen i Stockholm Förhandlingar*, *105*(1), 9–15. https://doi.org/10.1080/11035898309455285

Cochrane, R., Spikings, R. A., Chew, D., Wotzlaw, J. F., Chiaradia, M., Tyrrel, S., Schaltegger, U., & van der Lelij, R.

(2014). High temperature (>350°C) thermochronology and mechanisms of Pb loss in apatite. *Geochimica et Cosmochimica Acta*, *127*, 39–56. https://doi.org/10.1016/j.gca.2013.11.028

Corfu, F., & Andersen, T. B. (2002). U-Pb ages of the Dalsfjord Complex, SW Norway, and their bearing on the correlation of allochthonous crystalline segments of the Scandinavian Caledonides. *International Journal of Earth Science*, *91*, 955–963. https://doi.org/10.1007/s00531-002-0298-3

Corfu, F., Austrheim, H., & Ganzhorn, A. C. (2013). Localized granulite and eclogite facies metamorphism at Flatraket and Kråkeneset, Western Gneiss Region: U–Pb data and tectonic implications. *Geological Society of London, Special Publication*, *390*, 425–442.

Cuthbert, S. J., Carswell, D. A., Krogh-Ravna, E. J., & Wain, A. (2000). Eclogites and eclogites in the Western Gneiss Region, Norwegian Caledonides. *Lithos*, *52*(1–4), 165–195. https://doi.org/10.1016/S0024-4937(99)00090-0

Cuthbert, S. J., & van Roermund, H. L. M. (2011). In-situ monazite dating of a microdiamond-bearing gneiss, Fjortoft, Norway: Age pattern in relation to garnet zoning and growth history. 9th Internation Eclogite Conference 2011.

Cutts, J. A., & Smit, M. A. (2018). Rates of deep continental burial from Lu-Hf garnet chronology and Zr-in-rutile thermometry on (ultra)high-pressure rocks. *Tectonics*, *37*, 71–88. https://doi.org/10.1002/2017TC004723

Cutts, J. A., Smit, M. A., Kooijman, E., & Schmitt, M. (2019). Two stage cooling and exhumation of deeply subducted continents. *Tectonics*, *38*, 863–877. https://doi.org/10.1029/2018TC005292

Dallmeyer, R. D., & Gee, D. G. (1986). 40Ar/39Ar mineral dates from retrogressed eclogites within the Baltoscandian miogeocline: Implications for a polyphase Caledonian orogenic evolution. *Geological Society of America Bulletin*, *97*(1), 26–34. https://doi.org/10.1130/0016-7606(1986)97%3C26:AMDFRE%3E2.0.CO;2

Dallmeyer, R. D., Gee, D. G., & Beckholmen, M. (1985). 40Ar/39Ar mineral age record of early Caledonian tectonothermal activity in the Baltoscandian miogeocline, Central Scandinavia. *American Journal of Science*, *285*, 532–568.

Daniel, C. G., & Spear, F. (1999). The clustered nucleation and growth processes of garnet in regional metamorphic rocks from north-west Connecticut, USA. *Journal of Metamorphic Geology*, *17*(5), 503–520. https://doi.org/10.1046/j.1525-1314.1999.00200.x

DesOrmeau, J. W., Gordon, S. M., Kylander-Clark, A. R. C., Hacker, B. R., Bowring, S. A., Schoene, B., & Samperton, K. M. (2015). Insights into (U)HP metamorphism of the Western Gneiss Region, Norway: A high-spatial resoltuion and high-precision zircon study. *Chemical Geology*, *414*, 138–155.

Diener, J. F. A., & Powell, R. (2012). Revised activity-composition models for clinopyroxene and amphibole. *Journal of Metamorphic Geology*, *30*(2), 131–142. https://doi.org/10.1111/j.1525-1314.2011.00959.x

Dobrzhinetskaya, L. F., Eide, E. A., Larsen, R. B., Sturt, B. A., Trønnes, R. G., Smith, D. C., Taylor, W. R., & Posukhova, T. V. (1995). Microdiamond in high-grade metamorphic rocks of the Western Gneiss region, Norway. *Geology*, *23*(7), 597–600.

Donovan, J. J., & Rowe, M. (2005). Techniques for improving quantitative analysis of mineral glasses. Geochimica et Cosmochimica Acta, Goldschmidt abstracts.

Donovan, J. J., Singer, J. W., & Armstrong, J. T. (2016). A new EPMA method for fast trace element analysis in simple matrices. *American Mineralogist*, *101*(8), 1839–1853.

Donovan, J. J., & Tingle, T. N. (1996). An improved mean atomic number background correction for quantitative microanalysis. *Microscopy and Microanalysis*, *1*, 1–7.

Dransfield, M. (1994). *Extensional Exhumation of High-Grade Rocks in Western Norway and the Zanskar Himalaya*. University of Oxford.

Droop G. T. R. (1987). A general equation for estimating Fe3+ concentrations in ferromagnesian silicates and oxides from microprobe analyses, using stoichiometric criteria. *Mineralogical Magazine*, *51*(361), 431–435. https://doi.org/10.1180/minmag.1987.051.361.10

Dunning, G. R., & Pedersen, R. B. (1988). U/Pb ages of ophiolites and arc-related plutons of the Norwegian Caledonides: Implications for the development of Iapetus. *Contributions to Mineralogy and Petrology*, *98*(1), 13–23. https://doi.org/10.1007/BF00371904

Engvik, A. K., Andersen, T. B., & Wachmann, M. (2007). Inhomogeneous deformation in deeply buried continental crust, an example from the eclogite-facies province of the Western Gneiss Region, Norway. *Norwegian Journal of Geology*, *87*, 373–389.

Engvik, A. K., Willemoes-Wissing, B., & Lutro, O. (2018). High-temperature, decompressional equilibration of the eclogite facies orogenic root (Western Gneiss Region, Norway). *Journal of Metamorphic Geology*, *36*(5), 529–545. https://doi.org/10.1111/jmg.12418

Ernst, W. G., Maruyama, S., & Wallis, S. (1997). Buoyancy-driven, rapid exhumation of ultrahigh-pressure metamorphosed continental crust. *The National Academy of Sciences*, *94*(18), 9532–9537. https://doi.org/10.1073/pnas.94.18.9532

Fassmer, K., Froitzheim, N., Janák, M., Strohmeyer, M., Bukała, M., Lagos, M., & Münker, C. (2021). Diachronous collision in the Seve Nappe Complex: Evidence from Lu–Hf geochronology of eclogites (Norrbotten, North Sweden). *Journal of Metamorphic Geology*, *39*(7), 819–842. https://doi.org/10.1111/jmg.12591

Fassmer, K., Klonowska, I., Walczak, K., Andersson, B., Froitzheim, N., Majka, J., Fonseca, R. O., Münker, C., Janák, M., & Whitehouse, M. (2017). Middle Ordovician subduction of continental crust in the Scandinavian Caledonides: An example from Tjeliken, Seve Nappe Complex, Sweden. *Contributions to Mineralogy and Petrology*, *172*(103). https://doi.org/10.1007/s00410-017-1420-7

Ferry, J. M., & Watson, E. B. (2007). New thermodynamic models and revised calibrations for the Ti-in-zircon and Zr-in-rutile thermometers. *Contributions to Mineralogy and Petrology*, *154*, 429–437. https://doi.org/10.1007/s00410-007-0201-0

Furnes, H., Dilek, Y., & Pedersen, R. B. (2012). Structure, geochemistry, and tectonic evolution of trench-distal backarc oceanic crust in the western Norwegian Caledonides, Solund-Stavfjord ophiolite (Norway). *GSA Bulletin*, *124*(7/8), 1027–1047. https://doi.org/10.1130/B30561.1

Furnes, H., Ryan, P. D., Grenne, T., Roberts, D., Sturt, B. A., & Prestvik, T. (1985). Geological and geochemical classification of the ophiolite fragments in the Scandinavian Caledonides. In D. G. Gee & B. A. Sturt (Eds.), *The Caledonide Orogen -*

Scandinavia and Related Areas (pp. 657–669). John Wiley & Sons Ltd.

Garber, J. M., Hacker, B. R., Kylander-Clark, A. R. C., Stearns, M., & Seward, G. (2017). Controls on trace element uptake in metamorphic titanite: implications for petrochronology. *Journal of Petrology*, *58*, 1031–1058.

Gee, D. G. (1975). A tectonic model for the central part of the Scandinavian Caledonides. *American Journal of Science*, *275-A*, 468–515.

Gee, D. G., Janák, M., Majka, J., Robinson, P., & van Roermund, H. L. M. (2013). Subduction along and within the Baltoscandian margin during closing of the Iapetus Ocean and Baltica-Laurentia collision. *Lithosphere*, *5*(2), 169–178. https://doi.org/10.1130/L220.1

Gee, D. G., Klonowska, I., Andréasson, P. G., & Stephens, M. B. (2020). Middle thrust sheets in the Caledonide orogen, Sweden: the outer margin of Baltica, the continent–ocean transition zone and late Cambrian–Ordovician subduction–accretion. *Geological Society, London, Memoirs*, *50*, 517–548. https://doi.org/10.1144/M50-2018-73

Gilio, M., Scambelluri, M., Angel, R. J., & Alvaro, M. (2021). The contribution of elastic geothermobarometry to the debate on HP versus UHP metamorphism. *Journal of Metamorphic Geology*, *40*(2), 229–242. https://doi.org/10.1111/jmg.12625

Gilotti, J. A., Nutman, A. P., & Brueckner, H. K. (2004). Devonian to Carboniferous collision in the Greenland Caledonides: U-Pb zircon and Sm-Nd ages of high-pressure and ultrahigh-pressure metamorphism. *Contributions to Mineralogy and Petrology*, *148*, 216–235.

Gjelsvik, T. (1951). Oversikt over bergartene på Sunnmøre og tilgrensende deler av Nordfjord. *Med geologisk oversiktskart av T. Gjelsvik & Chr. C. Gleditsch. Norges Geologiske Undersøkelse*, *179*, 1–45.

Glodny, J., Kühn, A., & Austrheim, H. (2008). Diffusion versus recrystallization processes in Rb–Sr geochronology: Isotopic relics in eclogite facies rocks, Western Gneiss Region, Norway. *Geochimica et Cosmochimica Acta*, *72*(2), 506–525. https://doi.org/10.1016/j.gca.2007.10.021

Green, E. C. R., White, R. W., Diener, J. F. A., Powell, R., Holland, T. J. B., & Palin, R. M. (2016). Activity-composition relations for the calculation of partial melting equilibria in metabasic rocks. *Journal of Metamorphic Geology*, *34*(9), 845–869. https://doi.org/10.1111/jmg.12211

Griffin, W. L., & Brueckner, H. K. (1980). Caledonian Sm-Nd ages and crustal origin for Norwegian eclogites. *Nature*, *285*, 319–321. https://doi.org/10.1038/285319a0

Griffin, W. L., & Brueckner, H. K. (1985). REE, Rb-Sr and Sm-Nd studies of Norwegian eclogites. *Chemical Geology*, *52*, 249–271.

Gromet, L. P., Bergman, S., Sjöström, H., & Claesson, S. (1993). High-precision metamorphic U-Pb ages in the Seve Nappes, Scandinavian Caledonides of central Sweden. Geological Society of America, Annual Meeting, Abstract Volume 25, 340.

Hacker, B. R. (2007). Ascent of the ultrahigh-pressure Western Gneiss Region, Norway. Convergent Margin Terranes and Associated Regions: A Tribute to W.G. Ernst, M. Cloos, W.D. Carlson, M.C. Gilbert, J.G. Liou, S.S. Soreson, 171–184.

Hacker, B. R., Andersen, T. B., Johnston, S., Kylander-Clark, A. R. C., Peterman, E. M., Walsh, E. O., & Young, D. J. (2010). High-temperature deformation during continental-

margin subduction and exhumation: The ultrahigh-pressure Western Gneiss Region of Norway. *Tectonophysics*, *480*, 149–171. https://doi.org/10.1016/j.tecto.2009.08.012

Hacker, B. R., & Gans, P. B. (2005). Continental collisions and the creation of ultrahigh-pressure terranes: Petrology and thermochronology of nappes in the central Scandinavian Caledonides. *GSA Bulletin*, *117*(1/2), 117–134. https://doi.org/10.1130/B25549.1

Hacker, B. R., Keleman, P. B., & Behn, M. D. (2011). Differentiation of the continental crust by relamination. *Earth and Planetary Science Letters*, *307*(3–4), 501–516. https://doi.org/10.1016/j.epsl.2011.05.024

Hacker, B. R., Kylander-Clark, A. R. C., Holder, R., Andersen, T. B., Peterman, E. M., Walsh, E. O., & Munnikhuis, J. K. (2015). Monazite response to ultrahigh-pressure subduction from U-Pb dating by laser ablation split stream. *Chemical Geology*, *409*, 28–41. https://doi.org/10.1016/j.chemgeo.2015.05.008

Halpin, J. A., Daczko, N. R., Milan, L. A., & Clarke, G. L. (2012). Decoding near-concordant U–Pb zircon ages spanning several hundred million years: recrystallisation, metamictisation or diffusion? *Contributions to Mineralogy and Petrology*, *163*, 67–85. https://doi.org/10.1007/s00410-011-0659-7

Harrison, T. M., Célérier, J., Aikman, A. B., Hermann, J., & Heizler, M. T. (2009). Diffusion of 40Ar in muscovite. *Geochimica et Cosmochimica Acta*, *73*(4), 1039–1051. https://doi.org/10.1016/j.gca.2008.09.038

Hellstrom, J., Paton, C., Woodhead, J., & Hergt, J. (2008). Iolite: Software for spatially resolved LA-(quad and MC) ICPMS analysis. *Mineralogical Association of Canada short course series*, 343–348.

Holder, R., Hacker, B. R., Kylander-Clark, A. R. C., & Cottle, J. M. (2015). Monazite trace-element and isotopic signatures of (ultra)high-pressure metamorphism: Examples from the Western Gneiss Region, Norway. *Chemical Geology*, *409*, 99–111. https://doi.org/10.1016/j.chemgeo.2015.04.021

Holder, R., Yakymchuk, C., & Viete, D. R. (2020). Accessory mineral Eu anomalies in suprasolidus rocks: Beyond feldspar. *Geochemistry, Geophysics, Geosystems*, *21*(8). https://doi.org/10.1029/2020GC009052

Holland, T., & Powell, R. (2003). Activity-composition relations for phases in petrological calculations: an asymmetric multicomponent formulation. *Contributions to Mineralogy and Petrology*, *145*(4), 492–501. https://doi.org/10.1007/s00410-003-0464-z

Holland, T. J. B., & Powell, R. (2011). An improved and extended internally consistent thermodynamic dataset for phases of petrological interest, involving a new equation of state for solids. *Journal of Metamorphic Geology*, *29*(3), 333–383. https://doi.org/10.1111/j.1525-1314.2010.00923.x

Holmberg, J., Bukała, M., Jeanneret, P., Klonowska, I., & Majka, J. (2019). Decompressional equilibration of the Midsund Granulite from Otrøy, Western Gneiss Region, Norway. *Geologica Carpathica*, *70*(6), 471–482. https://doi.org/10.2478/geoca-2019-0027

Jackson, S. E., Pearson, N. J., Griffin, W. L., & Belousova, E. A. (2004). The application of laser ablation-inductively coupled plasma-mass spectrometry to in situ U–Pb zircon geochronology. *Chemical Geology*, *211*(1), 47–69.

Jeanneret, P., Walczak, K., Majka, J., Bukała, M., Cuthbert, S. J., & Kooijman, E. (2021). In-situ U-(Th-)Pb dating and REE analysis of zircon and monazite in the Grt-bearing gneisses from Gossa: Tracing early subduction into the highest-grade domains of the Western Gneiss Region, Norway. vEGU21, the 23rd EGU General Assembly, Abstract. https://doi.org/10.5194/egusphere-egu21-7275

Jolivet, L., Raimbourg, H., Labrousse, L., Avigad, D., Leroy, Y., Austrheim, H., & Andersen, T. B. (2005). Softening trigerred by eclogitisation, the first step toward exhumation during continental subduction. *Earth and Planetary Science Letters*, *237*(3–4), 532–547.

Kohn, M. J. (2020). A refined zirconium-in-rutile thermometer. *American Mineralogist*, *105*(6), 963–971. https://doi.org/10.2138/am-2020-7091

Kooijman, E., Mezger, K., & Berndt, J. (2010). Constraints on the U-Pb systematics of metamorphic rutile from in situ LA-ICP-MS analysis. *Earth and Planetary Science Letters*, *293*, 321–330. https://doi.org/10.1016/j.epsl.2010.02.047

Krabbendam, M., Wain, A., & Andersen, T. B. (2000). Pre-Caledonian granulite and gabbro enclaves in the Western Gneiss Region, Norway: Indications of incomplete transition at high pressure. *Geological Magazine*, *137*, 235–255.

Krogh, E. J. (1977). Evidence for Precambrian continent-continent collision in western Norway. *Nature*, *267*, 17–19. https://doi.org/10.1038/267017a0

Krogh, T. E., Kamo, S. L., Robinson, P., Terry, M. P., & Kwok, K. (2011). U–Pb zircon geochronology of eclogites from the Scandian Orogen, northern Western Gneiss Region, Norway: 14–20 million years between eclogite crystallization and return to amphibolite facies conditions. *Canadian Journal of Earth Sciences*, *48*(2), 441–472.

Krogstad, E., & Walker, R. J. (1994). High closure temperatures of the U-Pb system in large apatites from the Tin Mountain pegmatite, Black Hills, South Dakota, USA. *Geochimica et Cosmochimica Acta*, *58*(18), 3845–3853. https://doi.org/10.1016/0016-7037(94)90367-0

Kylander-Clark, A. R. C., & Hacker, B. R. (2014). Age and significance of felsic dikes from the UHP western gneiss region. *Tectonics*, *33*, 2342–2360.

Kylander-Clark, A. R. C., Hacker, B. R., & Cottle, J. M. (2013). Laser-ablation split-stream ICP petrochronology. *Chemical Geology*, *345*, 99–112. https://doi.org/10.1016/j.chemgeo.2013.02.019

Kylander-Clark, A. R. C., Hacker, B. R., & Johnson, C. M. (2009). Slow subduction of a thick ultrahigh-pressure terrane. *Tectonics*, *28*(2), TC2003. https://doi.org/10.1029/2007TC002251

Kylander-Clark, A. R. C., Hacker, B. R., Johnson, C. M., Beard, B. L., Mahlen, N. J., & Lapen, T. J. (2007). Coupled Lu-Hf and Sm-Nd geochronology constrains prograde and exhumation histories of high- and ultrahigh-pressure eclogites from western Norway. *Chemical Geology*, *242*, 137–154. https://doi.org/10.1016/j.chemgeo.2007.03.006

Kylander-Clark, A. R. C., Hacker, B. R., & Mattinson, J. M. (2008). Slow exhumation of UHP terranes: Titanite and rutile ages of the Western Gneiss Region, Norway. *Earth and Planetary Science Letters*, *272*, 531–540. https://doi.org/10.1016/j.epsl.2008.05.019

Labrousse, L., Jolivet, L., Andersen, T. B., Agard, P., Hébert, R., Maluski, H., & Schärer, U. (2004). Pressure-temperature-time deformation history of the exhumation of ultra-high

pressure rocks in the Western Gneiss Region, Norway. *Gneiss domes in orogeny*, Special Paper of the Geological Society of America (Vol. 380). https://doi.org/10.1130/0-8137-2380-9.155

Liu, P., & Massone, H.-J. (2019). An anticlockwise P-T-t path at high-pressure, high-temperature conditions for a migmatitic gneiss from the Island of Fjørtoft, Western Gneiss Region, Norway, indicates two burial events during the Caledonian Orogeny. *Journal of Metamorphic Geology*, *37*, 567–588. https://doi.org/10.1111/jmg.12476

Luvizotto, G. L., & Zack, T. (2009). Nb and Zr behavior in rutile during high-grade metamorphism and retrogression: An example from the Ivrea–Verbano Zone. *Chemical Geology*, *261*(3–4), 303–317. https://doi.org/10.1016/j.chemgeo.2008.07.023

Majka, J., Be'eri-Shlevin, Y., Gee, D. G., Ladenberger, A., Claesson, S., Konečný, P., & Klonowska, I. (2012). Multiple monazite growth in the Åreskutan migmatite: Evidence for a polymetamorphic Late Ordovician to Late Silurian evolution in the Seve Nappe Complex of west-central Jämtland, Sweden. *Journal of Geosciences (Prague)*, *57*, 3–23. https://doi.org/10.3190/jgeosci.112

Majka, J., Mazur, S., Młynarska, M., Klonowska, I., Tual, L., Kośmińska, K., Tarasiuk, J., & Wroński, S. (2018). Integrating X-ray mapping and microtomography of garnet with thermobarometry to define the P–T evolution of the (near) UHP Międzygórze eclogite, Sudetes, SW Poland. *Journal of Metamorphic Geology*, *37*(1), 97–112. https://doi.org/10.1111/jmg.12450

Majka, J., Rosén, Å., Janák, M., Froitzheim, N., Klonowska, I., Manecki, M., Sasinková, V., & Yoshida, K. (2014). Microdiamond discovered in the Seve Nappe (Scandinavian Caledonides) and its exhumation by the "vacuum-cleaner" mechanism. *Geology*, *42*(12), 1107–1110. https://doi.org/10.1130/G36108.1

Mcclelland, W. C., Power, S. E., Gilotti, J. A., Mazdab, F. K., & Wopenka, B. (2006). U-Pb SHRIMP geochronology and trace element geochemistry of coesitebearing zircons, North-East Greenland Caledonides. In B. Hacker, W. C. McClelland, & J. G. Liou (Eds.), *Ultrahigh-pressure metamorphism: Deep continental subduction* (Vol. 403) (pp. 23–43). Geological Society of America, Special Paper.

McLennan, S. M. (1989). Rare earth elements in sedimentary rocks: Influence of provenance and sedimentary processes. *Reviews in Mineralogy*, *21*, 169–200. https://doi.org/10.1515/9781501509032-010

Mearns, E. W. (1986). Sm-Nd ages for Norwegian garnet peridotite. *Lithos*, *19*, 269–278. https://doi.org/10.1016/0024-4937(86)90027-7

Mezger, K., & Krogstad, E. (1997). Interpretation of discordant U-Pb zircon ages: An evaluation. *Journal of Metamorphic Geology*, *15*(1), 127–140. https://doi.org/10.1111/j.1525-1314.1997.00008.x

Mørk, M. B. E., Kullerud, K. V., & Stabel, A. (1988). Sm–Nd dating of Seve eclogites, Norrbotten, Sweden: evidence for early Caledonian (505 Ma) subduction. *Contributions to Mineralogy and Petrology*, *99*, 344–351. https://doi.org/10.1007/BF00375366

Mørk, M. B. E., & Mearns, E. W. (1986). Sm–Nd isotopic systematics of a gabbro–eclogite transition. *Lithos*, *19*, 255–267.

Mysen, B. O., & Heier, K. S. (1972). Petrogenesis of eclogites in high-grade metamorphic gneisses exemplified by the Hareidland eclogite, west Norway. *Contributions to Mineralogy and Petrology*, *36*, 73–94.

Nagy, G., Draganits, E., Demeny, A., Panto, G., & Arkai, P. (2002). Genesis and transformations of monazite, florencite, and rhabdophane during medium grade metamorphism: Examples from the Sopron Hills, Eastern Alps. *Chemical Geology*, *191*(1–3), 25–46. https://doi.org/10.1016/S0009-2541(02)00147-X

Nance, D. R., & Murphy, B. J. (2013). Origins of the supercontinent cycle. *Geoscience Frontiers*, *4*(4), 439–448. https://doi.org/10.1016/j.gsf.2012.12.007

Nichols, G. T., Berry, R. F., & Green, D. H. (1992). Internally consistent gahnitic spinel-cordierite-garnet equilibria in the FMASHZn system: Geothermobarometry and applications. *Contributions to Mineralogy and Petrology*, *111*, 362–377. https://doi.org/10.1007/BF00311197

Paton, C., Hellstrom, J., Paul, B., Woodhead, J., & Hergt, J. (2011). Iolite: Freeware for the visualisation and processing of mass spectrometric data. *Journal of Analytical Atomic Spectrometry*, *26*(12), 2508. https://doi.org/10.1039/c1ja10172b

Payne, J. L., Hand, M., Barovich, K., & Wade, B. (2008). Temporal constraints on the timing of high-grade metamorphism in the northern Gawler Craton: Implications for assembly of the Australian Proterozoic. *Australian Journal of Earth Sciences*, *55*(5), 623–640. https://doi.org/10.1080/08120090801982595

Pearce, N. J. G., Perkins, W. T., Westgate, J. A., Gorton, M. P., Jackson, S. E., Neal, C. R., & Chenery, S. P. (2007). A compilation of new and published major and trace element data for NIST SRM 610 and NIST SRM 612 glass reference material. *Geostandards Newsletter*, *21*(1), 115–144. https://doi.org/10.1111/j.1751-908X.1997.tb00538.x

Pedersen, R. B., & Dunning, G. R. (1997). Evolution of arc crust and relations between contrasting sources: U-Pb (age), Nd and Sr isotope systematics of the ophiolite terrain of SW Norway. *Contributions to Mineralogy and Petrology*, *128*(1), 1–15. https://doi.org/10.1007/s004100050289

Pedersen, R. B., & Furnes, H. (1991). Geology, magmatic affinity and geotectonic environment of some Caledonian ophiolites in Norway. *Journal of Geodynamics*, *13*(2–4), 183–203. https://doi.org/10.1016/0264-3707(91)90038-G

Peterman, E. M., Hacker, B. R., & Baxter, E. F. (2009). Phase transformations of continental crust during subduction and exhumation: Western Gneiss Region, Norway. *European Journal of Mineralogy*, *21*(6), 1097–1118. https://doi.org/10.1127/0935-1221/2009/0021-1988

Platt, J. P. (1993). Exhumation of high-pressure rocks: A review of concepts and processes. *Terra Nova*, *5*(2), 119–133. https://doi.org/10.1111/j.1365-3121.1993.tb00237.x

Renedo, R. N., Nachlas, W. O., Whitney, D. L., Teyssier, C., Piazolo, S., Gordon, S. M., & Fosson, H. (2015). Fabric development during exhumation from ultrahigh-pressure in an eclogite-bearing shear zone, Western Gneiss Region, Norway. *Journal of Structural Geology*, *71*, 58–70. https://doi.org/10.1016/j.jsg.2014.09.012

Roberts, D. (2002). The Scandinavian Caledonides: Event chronology, palaeogeographic settings and likely modern analogues.

Tectonophysics, *365*, 283–299. https://doi.org/10.1016/S0040-1951(03)00026-X

Roberts, D. (2003). The Scandinavian Caledonides: Event chronology, palaeogeographic settings and likely modern analogues. *Tectonophysics*, *365*, 283–299. https://doi.org/10.1016/S0040-1951(03)00026-X

Roberts, D., & Gee, D. G. (1985). An introduction to the structure of the Scandinavian Caledonides. In D. G. Gee & B. A. Sturt (Eds.), *The Caledonide Orogen—Scandinavia and Related Areas* (pp. 55–68). Wiley.

Robinson, P. (1995). Extension of Trollheimen tectono-stratigraphic sequence in deep synclines near Molde and Brattvåg, Western Gneiss Region, southern Norway. *Norsk Geologisk Tidsskrift*, *75*, 181–198.

Romer, R. L. (1994). Rb-Sr data structure—A possible cause for differences in Rb-Sr whole-rock and U-Pb zircon ages. *GFF*, *116*(2), 93–103. https://doi.org/10.1080/11035899409546165

Root, D. B., & Corfu, F. (2009). Zircon U–Pb dating reveals two discrete episodes of Ordovician high-pressure metamorphism within the Seve Nappe Complex, Scandinavian Caledonides. American Geophysical Union, Fall Meeting 2009, abstract #V43D-2298.

Root, D. B., & Corfu, F. (2012). U–Pb geochronology of two discrete Ordovician high-pressure metamorphic events in the Seve Nappe Complex, Scandinavian Caledonides. *Contributions to Mineralogy and Petrology*, *163*, 769–788. https://doi.org/10.1007/s00410-011-0698-0

Root, D. B., Hacker, B. R., Gans, P. B., Ducea, M. N., Eide, E. A., & Mosenfelder, J. L. (2005). Discrete ultrahigh-pressure domains in the Western Gneiss Region, Norway: Implications for formation and exhumation. *Journal of Metamorphic Geology*, *23*, 45–61. https://doi.org/10.1111/j.1525-1314.2005.00561.x

Root, D. B., Hacker, B. R., Mattinson, J. M., & Wooden, J. L. (2004). Zircon geochronology and ca. 400 Ma exhumation of Norwegian ultrahigh-pressure rocks: An ion microprobe and chemical abrasion study. *Earth and Planetary Science Letters*, *228*, 325–341.

Rosenbaum, G., Gasparon, M., Lucente, F. P., Peccerillo, A., & Miller, M. S. (2008). Kinematics of slab tear faults during subduction segmentation and implications for Italian magmatism. *Tectonics*, *27*(2). https://doi.org/10.1029/2007TC002143

Rubatto, D. (2002). Zircon trace element geochemistry: partitioning with garnet and the link between U–Pb ages and metamorphism. *Chemical Geology*, *184*(1–2), 123–138. https://doi.org/10.1016/S0009-2541(01)00355-2

Rubatto, D., Chakraborty, S., & Dasgupta, S. (2013). Timescales of crustalmelting in the Higher Himalayan Crystallines (Sikkim, Eastern Himalaya) inferred from trace element constrained monazite and zircon chronology. *Contributions to Mineralogy and Petrology*, *165*, 349–372.

Schärer, U., & Labrousse, L. (2003). Dating the exhumation of UHP rocks and associated crustal melting in the Norwegian Caledonides. *Contributions to Mineralogy and Petrology*, *144*, 758–770. https://doi.org/10.1007/s00410-002-0428-8

Schoene, B., & Bowring, S. A. (2006). U–Pb systematics of the McClure Mountain syenite: Thermochronological constraints on the age of the 40Ar/39Ar standard MMhb. *Contributions to Mineralogy and Petrology*, *151*, 615–630. https://doi.org/10.1007/s00410-006-0077-4

Simpson, A., Gilbert, S. E., Tamblyn, R., Hand, M., Spandler, C., Gillespie, J., Nixon, A., & Glorie, S. (2021). In-situ Lu–Hf geochronology of garnet, apatite and xenotime by LA ICP MS/MS. *Chemical Geology*, *577*(1–2), 120299. https://doi.org/10.1016/j.chemgeo.2021.120299

Sizova, E., Hauzenberger, C., Fritz, H., Faryad, S. W., & Gerya, T. (2019). Late orogenic heating of (ultra)high pressure rocks: Slab rollback vs. slab breakoff. *Geosciences*, *9*(12), 499. https://doi.org/10.3390/geosciences9120499

Sjöström, H., & Bergman, S. (1994). Contraction and lateral extension in the Caledonian orogenic wedge of Central Scandinavia: evidence from a segment of the Seve-Köli terrane boundary. 21:a Nordiska Geologiska Vintermötet, Luleå 1994, Abstracts, 186.

Sláma, J., Košler, J., Condon, D. J., Crowley, J. L., Gerdes, A., Hanchar, J. M., Horstwood, M. S., Morris, G. A., Nasdala, L., Norberg, N., Schaltegger, U., Schoene, B., Tubrett, M. N., & Whitehouse, M. J. (2008). Plešovice zircon—A new natural reference material for U–Pb and Hf isotopic microanalysis. *Chemical Geology*, *249*(1–2), 1–35. https://doi.org/10.1016/j.chemgeo.2007.11.005

Smith, D. C. (1984). Coesite in clinopyroxene in the Caledonides and its implications for geodynamics. *Nature*, *310*, 641–644.

Smith, D. C., & Godard, G. (2013). A Raman spectroscopic study of diamond and disordered sp3-carbon in the coesite-bearing Straumen Eclogite Pod, Norway. *Journal of Metamorphic Geology*, *31*(1), 19–33.

Smye, A. J., Greenwood, L. V., & Holland, T. J. B. (2010). Garnet-chloritoid-kyanite assemblages: Eclogite facies indicators of subduction constraints in orogenic belts. *Journal of Metamorphic Geology*, *28*(7), 753–768. https://doi.org/10.1111/j.1525-1314.2010.00889.x

Sobolev, N. V., & Shatsky, V. S. (1990). Diamond inclusions in garnets from metamorphic rocks: A new environment of diamond formation. *Nature*, *343*, 742–746.

Spencer, K. J., Hacker, B. R., Kylander-Clark, A. R. C., Andersen, T. B., Cottle, J. M., Stearns, M. A., Poletti, J. E., & Seward, G. G. E. (2013). Campaign-style titanite U–Pb dating by laser-ablation ICP: Implications for crustal flow, phase transformations and titanite closure. *Chemical Geology*, *341*, 84–101. https://doi.org/10.1016/j.chemgeo.2012.11.012

Spengler, D., van Roermund, H. L. M., Drury, M. R., Ottolini, L., Mason, R. D., & Davies, G. R. (2006). Deep origin and hot melting of an Archaean orogenic peridotite massif in Norway. *Nature*, *440*(13), 913–917.

Spiess, R., Peruzzo, L., Prior, D. J., & Wheeler, J. (2008). Development of garnet porphyroblasts by multiple nucleation, coalescence and boundary misorientation-driven rotations. *Journal of Metamorphic Geology*, *19*(3), 269–290. https://doi.org/10.1046/j.1525-1314.2001.00311.x

Štípská, P., Powell, R., White, R. W., & Baldwin, J. A. (2010). Using calculated chemical potential relationships to account for-coronas around kyanite: an example from the Bohemian Massif. *Journal of Metamorphic Geology*, *28*, 97–116. https://doi.org/10.1111/j.1525-1314.2009.00857.x

Stølen, L. (1994). The rift-related mafic dyke complex of the Rohkunborri Nappe, Indre Troms, northern Norwegian Caledonides. *Norsk Geologisk Tidsskrift*, *74*, 35–47.

Tamblyn, R., Hand, M., Simpson, A., Gilbert, S. E., Wade, B., & Glorie, S. (2021). In-situ laser ablation Lu–Hf geochronology

of garnet across the Western Gneiss Region: Campaign-style dating of metamorphism. *Journal of the Geological Society.*, jgs2021–jgs2094. https://doi.org/10.1144/jgs2021-094

Tartakovsky, A. M., Meakin, P., Scheibe, T. D., & Wood, B. D. (2007). A smoothed particle hydrodynamics model for reactive transport and mineral precipitation in porous and fractured porous media. *Water Resources Research*, *43*(5). https://doi.org/10.1029/2005WR004770

Terry, M. P., & Robinson, P. (2004). Geometry of eclogite facies structural features: Implications for production and exhumation of ultrahigh-pressure and high-pressure rocks, Western Gneiss Region, Norway. *Tectonics*, *23*(2) TC2001 2001-2023. https://doi.org/10.1029/2002TC001401

Terry, M. P., Robinson, P., & Krogh Ravna, E. J. (2000a). Kyanite eclogite thermobarometry and evidence for thrusting of UHP over HP metamorphic rocks, Nordøyane, Western Gneiss Region, Norway. *American Mineralogist*, *85*, 1637–1650.

Terry, M. P., Robinson, P., Hamilton, M. A., & Jercinovic, M. J. (2000b). Monazite geochronology of UHP and HP metamorphism, deformation, and exhumation, Nordøyane, Western Gneiss Region, Norway. *American Mineralogist*, *85*, 1651–1664. https://doi.org/10.2138/am-2000-11-1208

Thompson, J., Meffre, S., Maas, R., Kamenetsky, V., Kamenetsky, M., Goemann, K., Ehrig, K., & Danyushevsky, L. (2016). Matrix effects in Pb/U measurements during LA-ICP-MS analysis of the mineral apatite. *Journal of Analytical Atomic Spectrometry*, *31*(6), 1206–1215.

Thomson, S. N., Gehrels, G. E., Ruiz, J., & Buchwaldt, R. (2012). Routine low-damage apatite U-Pb dating using laser ablation–multicollector–ICPMS. *Geochemistry, Geophysics, Geosystems*, *13*(2). https://doi.org/10.1029/2011GC003928

Tual, L., Smit, M. A., Kooijman, E., & Schmitt, M. (2020). Comparative chronology of garnet, zircon and monazite in (ultra)high-temperature and -pressure rocks. *Goldschmidt Conference, Abstract*, https://doi.org/10.46427/gold2020.2630

Tucker, R. D., Krogh, T. E., & Råheim, A. (1990). Proterozoic evolution and age-province boundaries in the central part of the Western Gneiss Region, Norway. Results of U-Pb dating of accessory minerals from Trondheimsfjord to Geiranger. In C. F. Gower, A. B. Ryan, & T. Rivers (Eds.), *Mid-Proterozoic Laurentia–Baltica* (Vol. 38). Geological Association of Canada, Special Paper. (pp. 149–173).

Tucker, R. D., Råheim, A., Krogh, T. E., & Corfu, F. (1987). Uranium-lead zircon and titanite ages from the northern portion of the Western Gneiss Region, south-central Norway. *Earth and Planetary Science Letters*, *81*(2–3), 203–211. https://doi.org/10.1016/0012-821X(87)90156-7

Tucker, R. D., Robinson, P., Solli, A., Gee, D. G., Thorsnes, T., Krogh, T. E., Nordgulen, Ø., & Bickford, M. E. (2004). Thrusting and extension in the Scandian hinterland, Norway: New U–Pb ages and tectonostratigraphic evidence. *American Journal of Science*, *304*(6), 477–532. https://doi.org/10.2475/ajs.304.6.477

van Hunen, J., & Allen, M. B. (2011). Continental collision and slab break-off: A comparison of 3-D numerical models with observations. *Earth and Planetary Science Letters*, *302*(1–2), 27–37. https://doi.org/10.1016/j.epsl.2010.11.035

van Roermund, H. L. M., Carswell, D. A., Drury, M. R., & Heijboer, T. C. (2002). Microdiamonds in a megacrystic garnet websterite pod from Bardane on the island of Fjørtoft, western Norway: Evidence for diamond formation in mantle rocks during deep continental subduction. *Geology*, *30*(11), 959–962. https://doi.org/10.1130/0091-7613(2002)030%3C0959:MIAMGW%3E2.0.CO;2

van Roermund, H. L. M., & Drury, M. R. (1998). Ultra-high pressure (P>6 GPa) garnet peridotits in Western Norway: Exhumation of mantle rocks from >185km depth. *Terra Nova*, *10*, 295–301. https://doi.org/10.1046/j.1365-3121.1998.00213.x

Vrijmoed, J. C., Austrheim, H., John, T., Hin, R. C., Corfu, F., & Davies, G. R. (2013). Metasomatism in the ultrahigh-pressure Svartberget garnet-peridotite (Western Gneiss Region, Norway): Implications for the transport of crust-derived fluids within the mantle. *Journal of Petrology*, *54*(9), 1815–1848. https://doi.org/10.1093/petrology/egt032

Vrijmoed, J. C., Smith, D. C., & van Roermund, H. L. M. (2008). Raman confirmation of microdiamond in the Svartberget Fe-Ti type garnet peridotite, Western Gneiss Region, Western Norway. *Terra Nova*, *20*(4), 295–301.

Vrijmoed, J. C., van Roermund, H. L. M., & Davis, G. R. (2006). Evidence for diamond-grade ultrahigh-pressure metamorphism and fluid interaction in the Svartberget Fe–Ti garnet peridotite–websterite body, Western Gneiss Region, Norway. *Mineralogy and Petrology*, *88*, 381–405.

Wain, A. (1997). New evidence for coesite in eclogite and gneisses: Defining an ultrahigh-pressure province in the Western Gneiss Region of Norway. *Geology*, *25*, 927–930. https://doi.org/10.1130/0091-7613(1997)025%3C0927:NEFCIE%3E2.3.CO;2

Wain, A., Waters, D. J., & Austrheim, H. (2001). Metastability of granulites and processes of eclogitization in the UHP region of western Norway. *Journal of Metamorphic Geology*, *19*(5), 609–625. https://doi.org/10.1046/j.0263-4929.2001.00333.x

Walczak, K., Barnes, C., Majka, J., Gee, D. G., & Klonowska, I. (2020). Zircon age depth-profiling sheds light on the early Caledonian evolution of the Seve Nappe Complex in west-central Jämtland. *Geoscience Frontiers*, 101112. in press. https://doi.org/10.1016/j.gsf.2020.11.009

Walczak, K., Cuthbert, S., Kooijman, E., Majka, J., & Smit, M. A. (2019). U-Pb zircon age dating of diamond-bearing gneiss from Fjørtoft reveals repeated burial of the Baltoscandian margin during the Caledonian Orogeny. *Geological Magazine*, *156*, 1949–1964. https://doi.org/10.1017/S0016756819000268

Walsh, E. O., & Hacker, B. R. (2004). The fate of subducted continental margins: Two-stage exhumation of the high-pressure to ultrahigh-pressure Western Gneiss complex, Norway. *Journal of Metamorphic Geology*, *22*, 671–689.

Walsh, E. O., Hacker, B. R., Gans, P. B., Grove, M., & Gehrels, G. (2007). Protolith ages and exhumation histories of (ultra)high-pressure rocks across the Western Gneiss Region, Norway. *GSA Bulletin*, *119*(3/4), 289–301. https://doi.org/10.1130/B25817.1

Walsh, E. O., Hacker, B. R., Gans, P. B., Wong, M. S., & Andersen, T. B. (2013). Crustal exhumation of the Western Gneiss region UHP terrane, Norway: $^{40}Ar/^{39}Ar$ thermochronology and fault-slip analysis. *Tectonophysics*, *608*, 1159–1179. https://doi.org/10.1016/j.tecto.2013.06.030

Warren, C. J., Kelley, S. P., Sherlock, S. C., & Mcdonald, C. S. (2012). Metamorphic rocks seek meaningful cooling rate: Interpreting 40Ar/39Ar ages in an exhumed ultra-high pressure terrane. *Lithos*, *155*, 30–48. https://doi.org/10.1016/j.lithos.2012.08.011

Watson, E. B., Wark, D. A., & Thomas, J. B. (2006). Crystallization thermometers for zircon and rutile. *Contributions to Mineralogy and Petrology*, *151*(4), 413–433. https://doi.org/10.1007/s00410-006-0068-5

White, R. W., Powell, R., & Baldwin, J. A. (2008). Calculated phase equilibria involving chemical potentials to investigate the textural evolution of metamorphic rocks. *Journal of Metamorphic Geology*, *26*, 181–198. https://doi.org/10.1111/j.1525-1314.2008.00764.x

White, R. W., Powell, R., Holland, T. J., & Worley, B. A. (2000). The effect of TiO2 and Fe2O3 on metapelitic assemblages at greenschist and amphibolite facies conditions: mineral equilibria calculations in the system K2O-FeO-MgO-Al2O3-SiO2-H2O-TiO2-Fe2O3. *Journal of Metamorphic Geology*, *18*(5), 497–511. https://doi.org/10.1046/j.1525-1314.2000.00269.x

White, R. W., Powell, R., Holland, T. J., Johnson, T. E., & Green, E. C. R. (2014). New mineral activity-composition relations for thermodynamic calculations in metapelitic systems. *Journal of Metamorphic Geology*, *32*(3), 261–286. https://doi.org/10.1111/jmg.12071

Whitney, D. L., & Seaton, N. S. (2010). Garnet polycrystals and the significance of clustered crystallization. *Contributions to Mineralogy and Petrology*, *160*(4), 591–607. https://doi.org/10.1007/s00410-010-0495-1

Wiedenbeck, M., Alle, P., Corfu, F., Griffin, W. L., Meier, M., Oberli, F., Quadt, A. V., Roddick, J. C., & Spiegel, W. (1995). Three natural zircon standards for U–Th–Pb, Lu–Hf, trace element and REE analyses. *Geostandards Newsletter*, *19*(1), 1–23. https://doi.org/10.1111/j.1751-908X.1995.tb00147.x

Wilke, M., & Behrens, H. (1999). The dependence of the partitioning of iron and europium between plagioclase and hydrous tonalitic melt on oxygen fugacity. *Contributions to Mineralogy and Petrology*, *137*, 102–114.

Young, D. J., Hacker, B. R., Andersen, T. B., & Corfu, F. (2007). Prograde amphibolite facies to ultrahigh-pressure transition along Nordfjord, western Norway: implications for exhumation tectonics. *Tectonics*, *26*(1). https://doi.org/10.1029/2004TC001781

Young, D. J., & Kylander-Clark, A. R. C. (2015). Does continental crust transform during eclogite-facies metamorphism? *Journal of Metamorphic Geology*, *33*(4), 331–357. https://doi.org/10.1111/jmg.12123

Zack, T., Stockli, D. F., Luvizotto, G. L., Barth, M. G., Belousova, E. A., Wolfe, M. R., & Hinton, R. W. (2011). In situ U–Pb rutile dating by LA-ICP-MS: 208Pb correction and prospects for geological applications. *Contributions to Mineralogy and Petrology*, *162*(3), 515–530. https://doi.org/10.1007/s00410-011-0609-4

SUPPORTING INFORMATION

Additional supporting information may be found in the online version of the article at the publisher's website.

Figure S1. WGC2019J-25B *PM$_o$* pseudosection. Oxidation was constrained at 0.15.

Figure S2. WGC2019J-31A *PMo* pseudosection. Oxidation was constrained at 0.075.

Figure S3. WGC2019J-25B PH$_2$O pseudosection. The inferred peak field is indicated by the bold outline, and the calculated water content based on biotite and used in *P–T* modelling is given by the dashed lined.

Figure S4. WGC2019J-25B PH$_2$O pseudosection. The inferred peak field is indicated by the bold outline, and the calculated water content based on biotite and used in *P–T* modelling is given by the dashed lined.

Figure S5. Inset fields for WGC2019J-25B *P–T*.

Figure S6. WGC2019J-31A *P–T* pseudosection for a bulk composition including garnet.

Figure S7. WGC2019J-25B phase diagram coloured by computed garnet mode and annotated with the inferred P–T path.

Data S1. Appendix S1: Biotite-plagioclase intergrowth calculation.

Appendix S2. Calculating a *P–T* point.

Table S1. Geochronological summary of Caledonian ages from Nordoyane.

Table S2. Geochronological summary of Caledonian ages from Sørøyane.

Table S3. Whole-rock geochemistry for samples WGC2019J-25B and WGC2019J-31A.

Table S4. Representative electron microprobe analyses for minerals from samples WGC2019J-25B and WGC2019J-31A.

Table S5. LA–ICP–MS compositional data for garnet

Table S6. Zircon morphology

Table S7. LA–ICP–MS zircon results

Table S8. Monazite morphology

Table S9. LA–ICP–MS monazite results

Table S10. Biotite and K-feldspar Pb

Table S11. Apatite morphology

Table S12. LA–ICP–MS apatite results

Table S13. Rutile morphology

Table S14. LA–ICP–MS rutile results